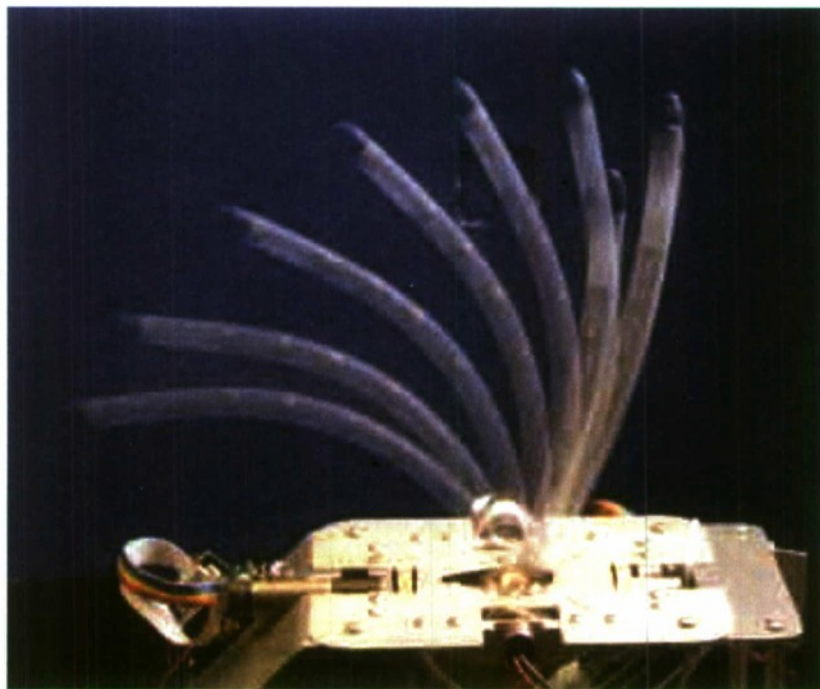


Exploration of Self-Regulation in the Natural Swimming of the Paramecium's Cilium

Promode R. Bandyopadhyay
Joshua C. Hansen
Autonomous and Defensive Systems Department



**Naval Undersea Warfare Center Division
Newport, Rhode Island**

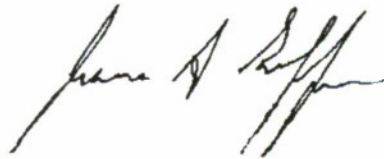
PREFACE

This report was prepared under Project No. N0001410-WX20352, "Co-Directivity," principal investigator Promode R. Bandyopadhyay (Code 823). The sponsoring activity is the Office of Naval Research (ONR-341, T. McKenna).

The technical reviewer for this report was J. Dana Hrubes (Code 8233).

The authors thank Messrs. Daniel Thivierge (NUWC Code 8231), Albert Fredette (NUWC Code 8231), and William Nedderman (McLaughlin Research Corporation) for their assistance with this work. The authors also gratefully acknowledge the numerous fruitful discussions with Norman Toplosky (NUWC Code 1532) and Kim Benjamin (NUWC Code 1512), which helped clarify many of the key issues.

Reviewed and Approved: 1 February 2012



James S. Griffin
Head, Autonomous and Defensive Systems Department



REPORT DOCUMENTATION PAGE				Form Approved OMB No. 0704-0188	
The public reporting burden for this collection of information is estimated to average 1 hour per response, including the time for reviewing instructions, searching existing data sources, gathering and maintaining the data needed, and completing and reviewing the collection of information. Send comments regarding this burden estimate or any other aspect of this collection of information, including suggestions for reducing this burden, to Department of Defense, Washington Headquarters Services, Directorate for Information Operations and Reports (0704-0188), 1215 Jefferson Davis Highway, Suite 1204, Arlington, VA 22202-4302. Respondents should be aware that notwithstanding any other provision of law, no person shall be subject to any penalty for failing to comply with a collection of information if it does not display a currently valid OPM control number. PLEASE DO NOT RETURN YOUR FORM TO THE ABOVE ADDRESS.					
1. REPORT DATE (DD-MM-YYYY) 01-02-2012		2. REPORT TYPE		3. DATES COVERED (From - To)	
4. TITLE AND SUBTITLE Exploration of Self-Regulation in the Natural Swimming of the Paramecium's Cilium				5a. CONTRACT NUMBER	
				5b. GRANT NUMBER	
				5c. PROGRAM ELEMENT NUMBER	
				5d. PROJECT NUMBER	
6. AUTHOR(S) Promode R. Bandyopadhyay Joshua C. Hansen				5e. TASK NUMBER	
				5f. WORK UNIT NUMBER	
7. PERFORMING ORGANIZATION NAME(S) AND ADDRESS(ES) Naval Undersea Warfare Center Division 1176 Howell Street Newport, RI 02841-1708				8. PERFORMING ORGANIZATION REPORT NUMBER TR 12,075	
9. SPONSORING/MONITORING AGENCY NAME(S) AND ADDRESS(ES) Office of Naval Research 875 North Randolph Street, Suite 1425 Arlington, VA 22203-1995				10. SPONSORING/MONITOR'S ACRONYM ONR	
				11. SPONSORING/MONITORING REPORT NUMBER	
12. DISTRIBUTION/AVAILABILITY STATEMENT Approved for public release; distribution is unlimited.					
13. SUPPLEMENTARY NOTES <div style="text-align: center; font-size: 1.5em; margin-top: 20px;">20/20307045</div>					
14. ABSTRACT This report explores the mechanics of the motion (and the aspects of bio-physical self-regulation of this motion) in the paramecium's cilium. The paramecium is a single-cell animal widely found in oxygenated aquatic environments. These animals propel themselves, albeit with limited maneuverability, by the synchronous motion of numerous tiny cilia populated around their flexible bodies. Three theoretical models are given: (1) a torsional pendulum model of beat frequency, (2) a nonlinear self-regulation model of cilium motion, and (3) a bio-physical mechanism of hardness control of the cilium. The first two models reproduce the experimental data quite accurately; a full modeling of the hydrolysis of adenosine-tri-phosphate (ATP), the "currency" of chemical energy (which is beyond the scope of this report), is awaited to quantitatively evaluate the third mechanism fully. Essentially, these theoretical results, together with an analysis of the motion of the biological cilium and a comparison of the results with various scaled biorobotic hardware models, are used to construct a bio-physical description of a self-regulating mechanism of natural swimming in the paramecium's cilium. It is theorized that cross-bridge links between the microtubule pairs are the source of cilium hardness during the power stroke; there is a critical phase near the end of the power stroke where one cross-bridge detaches at the point of inflection due to the arrival of ATP, causing a precipitous reduction in hardness that signals the start of the return stroke; therefore, in each beat cycle, there must be a reattachment process of the cross-bridge links and re-hardening of the cilium during the early phase of the return stroke. Also discussed is the invariance of the elementary oscillatory architecture of integrating sensors, actuators, and controllers from low to high Reynolds numbers (paramecia to fish). The present work helps lay the foundation of nonlinear underwater acoustic transduction, whose scope appears to be uncharted.					
15. SUBJECT TERMS Autonomy Biorobotics Biological Cilium Ciliary Propulsion Dynamic Systems Modeling of Ciliary Motion Hardness Control Natural Swimming Paramecium Robotic Cilium Underwater Acoustic Transduction					
16. SECURITY CLASSIFICATION OF:			17. LIMITATION OF ABSTRACT SAR	18. NUMBER OF PAGES 81	19a. NAME OF RESPONSIBLE PERSON Promode R. Bandyopadhyay
a. REPORT (U)	b. ABSTRACT (U)	c. THIS PAGE (U)			19b. TELEPHONE NUMBER (Include area code) 401-832-2712

TABLE OF CONTENTS

Section	Page
LIST OF ILLUSTRATIONS.....	ii
LIST OF TABLES.....	iv
1 INTRODUCTION	1
1.1 Literature Review.....	1
1.2 Purpose of This Work	3
2 MODELING	5
2.1 Modeling of the Natural Frequency of Oscillation of the Biological Cilium.....	5
2.2 Dynamic Systems Modeling of Cilium Motion.....	6
3 BIOLOGICAL AND ROBOTIC CILIUM DATA.....	9
3.1 Revisiting Biological Cilium Data.....	9
3.1.1 Collection and Processing of the Teunis and Machemer (1994) Data.....	9
3.1.2 Analysis of the Teunis and Machemer (1994) Data	13
3.2 Robotic Cilium.....	19
3.3 Comparison of Robotic Cilium and Biological Cilium	21
3.3.1 Comparison of Position.....	21
3.3.2 Comparison of Curvature and Torsion	23
4 SYNTHESIS OF RESULTS.....	27
4.1 Modeling the Increase and Decrease of the Biological Cilium's Hardness.....	27
4.2 Modeling of the Cross-Bridge Detachment/Softening	29
5 DISCUSSION	31
5.1 Development of Three-Dimensional Deformation in Cilium and the Role of Critical Hardness.....	31
5.2 Bio-Physical Self-Regulation of Cilium Hardness	31
5.3 Relationship with Larger Scale Natural Swimming: A Synthetic View.....	33
6 CONCLUSIONS.....	35
7 FUTURE WORK.....	37
8 BIBLIOGRAPHY	39
APPENDIX—SUPPLEMENTARY INFORMATION	A-1
A.1 Two-Dimensional Hydrodynamic Modeling.....	A-1
A.2 Validation of Digitization of Published Biological Cilium Data.....	A-5
A.3 Robotic Cilium.....	A-13
A.4 "Frictionless" Cilium Actuation Using a Hemispherical Motor Drive.....	A-18

TABLE OF CONTENTS (Cont'd)

Section	Page
A.5 Role of Torsional Rigidity in the Manifestation of Torsion	A-20
A.6 Progress Toward Robotic Emulation of Natural Swimming	A-25
A.7 Synthetic Modeling of the Transformation from Small to Large Via Optimization Mechanisms of Metachronism and Self-Regulation	A-28

LIST OF ILLUSTRATIONS

Figure	Page
1 (a) Schematic of the Torsional Pendulum Model of the Cilium; (b) Comparison of the Model with Measurements Due to Machemer (1972).....	6
2 Comparison of the Tracks of the Cilium of a Paramecium as Measured by Machemer (1972) and Per the Present Authors' Computation of LCO (Limit Cycle Oscillation) Using the Lienard Oscillator (Equation (2)).....	8
3 Variation of the Cilium Axial Distance from the Base with Beat Phase (= Time Step Number) in the Digitized Biological Cilium in the Revisited TM Data.....	11
4a Top View of the Cilium Beat Cycle in the Revisited TM Data.....	12
4b Side View of the Cilium in the Plane of the Power Stroke During the Beat Cycle in the Revisited TM Data.....	12
5 Variation of the Local Axial Angle of the Orbital Velocity and Position of the Biological Cilium Length Segments with Respect to the x -Axis (Power Stroke Axis) During the Beat Cycle in the Revisited TM Data	14
6 Variation of $\dot{X}(t)$ ($= \dot{x}(t)$) vs $\dot{y}(t)$ ($= \dot{y}(t)$) vs $\dot{z}(t)$ ($= \dot{z}(t)$) Using the Revisited TM Data.....	15
7 Inward Acceleration for the Revisited TM Data.....	15
8 Calculated Acceleration Components in the Biological Cilium Using the Revisited TM Data	16
9 Variation of Calculated Average Radius (R_{avg} in μm) of the Biological Cilium During the Beat Cycle in the Revisited TM Data	17
10 Calculated Variation of the Variable (Velocity x R_{avg} in $\mu\text{m}^2/\text{s}$) of the Biological Cilium in the Revisited TM Data.....	18
11 Photograph of the Scaled-Up Model of a Single Robotic Cilium	20
12 Strobe Picture of the Cilium in the Apparatus Shown in Figure 11	20
13a Comparison of the Biological Cilium and Robotic Cilium Positions—Side View: ($x(t)$, $y(t)$), and Top View: ($x(t)$, $z(t)$)	21
13b Comparison of Tracks in the Biological Cilium and Robotic Cilium	22
13c Comparison at Cilia Axial Distances of $S/L = 0.33$, 0.66 , and 1.0	22

LIST OF ILLUSTRATIONS (Cont'd)

Figure	Page
14 Comparison of the Robotic and Biological Cilium Positions at Each Time Step on the Longitudinal Plane	23
15 Comparison of the Curvature of the Robotic Cilium and the Biological Cilium Using the Revisited TM Data	25
16 Comparison of Torsion in the Robotic Cilium and the Biological Cilium.	26
17a Schematic of Compression-Tension Neutral-Plane Flipping at Point P on the Cilium at the Beat Phase of Neutral Equilibrium	28
17b Modeling of Cross-Bridge Link Between the Pair of Central Microtubules	28
A-1 Rigid Link Model of Cilium	A-2
A-2 Two-Dimensional Cilium Profiles.....	A-3
A-3 Two-Dimensional Base Thrust	A-3
A-4 Graph of Digitized Cilium Prior to Parametric Processing and Smoothing	A-6
A-5 Biological Cilium Waveform from the Revisited TM Data at the Distal Point Compared with Sine Waveforms in Cartesian and Polar Coordinates	A-12
A-6 Successive Frames from CAD Simulation of D-Cam-Guided Three-Link Robotic Cilium.....	A-14
A-7 Pendulum Apparatus for Understanding Cilium Motion.....	A-15
A-8 Schematic and Photograph of Early Version of the Biorobotic Cilium Apparatus	A-16
A-9 Schematic of Mechanism Showing How Planar Bending Is Produced in the Robotic Cilium by Sliding the Top Strip Relative to the Bottom Strip.....	A-17
A-10 Photographs of the Rotor and Stator of a Hemispherical Motor Assembly	A-18
A-11 Schematic of Electromagnets and Gaps in the Hemispherical Motor	A-19
A-12 Schematic of Mechanism for Actuating a Long Robotic Cilium	A-21
A-13 Development of Torsion in a Low-Hardness “Rod”	A-21
A-14 Effects of Clockwise and Anti-Clockwise Turning of a Doublet of a Two-Doublet, Sheathed Cilium Oriented Orthogonally	A-22
A-15 Cilia Constructed of Continuous Rubber.....	A-24
A-16 Effects of the Parameter a on Olivo-Cerebellar Modeling of Cilium Motion.....	A-26
A-17 Apparatus for Driving the Robotic Cilium Using the Electronic Rendition of Dynamic Systems Equation (1)	A-27
A-18 Thrust Actuators from S to M to L Considered in Bandyopadhyay (2009)	A-29
A-19 Schematic of How a Metachronic Wave Produced with a Densely Packed and Membrane-Wrapped Two-Dimensional Array of Cilia Can Emulate an Eel.....	A-29
A-20 Schematic of Progressive Unwrapping of the Cilium to Produce a Fish’s Pectoral Fin..	A-30
A-21 Sequence Rationalizing the S to L Progression	A-31

LIST OF TABLES

Table	Page
A-1 Hydrodynamic Modeling Background Information	A-4
A-2 Variation of RMS in Length Estimation in the Revisited TM Data (Entire Beat Cycle)...	A-8
A-3 Variation of RMS in Length Estimation in the Revisited TM Data (Power Stroke).....	A-9
A-4 Variation of RMS in Length Estimation in the Revisited TM Data (Return Stroke) ...	A-10
A-5 Physical Properties of Two Low-Viscosity Two-Component Urethane Casting Elastomers Used for the Robotic Cilia Shown in Figure A-14.....	A-24
A-6 Types of Distortion Observed in a Long Robotic Cilium When a Torque Is Applied at the Base	A-25

EXPLORATION OF SELF-REGULATION IN THE NATURAL SWIMMING OF THE PARAMECIUM'S CILIUM

1. INTRODUCTION

The paramecium is slipper-shaped ciliate protozoa widely found in oxygenated aquatic environments. Paramecia are 100 – 350 μm long, deformable, and may contain up to 3000 flexible cilia populated around their body, each cilium being about 17 μm long and 0.25 μm in diameter (Pernberg and Machemer, 1995). For propulsion, each cilium beats at about 14.1 Hz in water while undergoing a complicated, three-dimensional, phase-dependent motion. The assemblage of cilia also undergoes a coordinated motion, called metachronic motion—i.e., the assemblage beats with a constant phase difference between neighboring cilia (Machemer, 1972). The paramecium twists while going forward. It backs off and swims in a new direction when it meets an obstruction. The paramecium's swimming speed is about two body lengths per second (0.44 mm/s for a 200- μm -long paramecium (Wurzel, 2003)). The range of maneuvering motion that a paramecium can undergo is limited. In the following paragraphs, the literature on cilia motion and their metachronic assemblage and control is examined.

1.1 LITERATURE REVIEW

Information on the mathematical treatment of the three-dimensional motion of a single cilium can be found in Dillon and Fauci (2000), Hines and Blum (1978, 1983) and Brokaw (1966). Further information on metachronism can be found in Blake (1971), Gueron et al. (1997), Gueron and Levit-Guerevich (1999a, 1999b), Gueron and Liron (1992), Machemer (1972), and Ramia et al. (1993).

Teunis and Machemer (1994) have reported high-speed stereomicroscopic measurements of cilia motion and have derived the variation of curvature and torsion with the beat phase. They have also identified the power and return strokes of cilia motion. (In the present work, the Teunis and Machemer results are revisited.)

Dute and Kung (1978) have given the physiology of a cilium, indicating how the cilium motion is mechanically produced when a torque is applied at the cilium's base. Cilium motion is generated by a combination of a pair of linear tubular actuators (microtubules) at the center, which are surrounded by nine pairs of push-pull microtubules spaced at 40° apart (this actuator configuration of microtubules is called the "(9 + 2) structure"). Dute and Kung offer a mechanical model that bears some similarity to helicopter swashplates.

Hines and Blum (1978, 1983) have carried out a nonlinear theoretical analysis of the motion of a flagellum (approximately a longer cilium) using a sliding filament model. They reproduce bending propagation and argue that the cilium must be twisting. Dillon and Fauci (2000) have hydrodynamically modeled the cilium, incorporating a most detailed (9+ 2 "axenome") internal

elastic actuation structure. In their study, they reproduce the cilium beating as an emergent property of the coupling of the fluid and the actuator architecture. Gueron and Levit-Guerevich (2001) have incorporated the $9 + 2$ architecture in their theoretical model.

Cilium-cilium hydrodynamic interaction has been theoretically examined by Gueron and Liron (1992) and Gueron et al. (1997), extending the substantial earlier theoretical work on the hydrodynamics of a single cilium (see their paper for the earlier works). Their model is two-dimensional. They show that in two cilia beating at a random phase difference, they synchronize within two beat cycles when brought closer together; that is, the metachronal pattern *develops autonomously*. The implication is that metachronism is a self-organizing phenomenon.

How the motion of the cilium (that is, the hydrodynamics) is controlled can be gleaned from the following. Machemer (1972), Nakaoka et al. (1984), and dePeyer and Machemer (1983) have shown that voltage stimulation affects cilia motility. Slow voltage ramps (5 to 10 mV/s) and moderate amplitudes (± 20 mV) are shown to make the membrane properties time dependent, which affects ciliary response (cycle time and relaxation time). Pernberg and Machemer (1995) and Deitmer et al. (1984) have shown that the cilia beating frequency and reverse/forward motion switching are affected by calcium channel activation. Jaffe (2007) has examined 60 data sets on flagella and cilia and has shown that stretch-activated calcium channels cause calcium and other waves to propagate at speeds of 100 to 1000 $\mu\text{m/s}$, which affects the tubular actuators mentioned earlier.

Understanding of the cilium bending at the cellular level due to cross-bridge linking has made rapid strides. Cordova et al (1992) have mechanically modeled the attachment of a single motor molecule. Electrostatic force between the cross-bridge and the binding site is used to generate the cross-bridge link motion, and against an elastic restoring force, the cross-bridge fluctuates and its step size varies nonlinearly with force.

Tamm and Tamm (1989) have studied microtubule sliding experimentally; the attachment of a Ca ion to a cilium is found to involve *locally confined oscillatory bending*.

Some say that the mechanism of metachronism is hydrodynamic coupling, and some say that it is electrical (membrane potential) in origin (Tamm, 1984). The former is largely based on two-dimensional fluid dynamics modeling, and the paramecium's cilia also show electro-mechanical response. (The present report explores these approaches from the point of view of self-regulation in mechanical systems.)

A photon correlation technique has led to the measurement of relaxation times of 5 μs in single muscle fiber (Yeh et al., 1990). A lower frequency of 370 kHz is also present. The high frequency comes from the cross-bridge linking and the low frequency from certain thick filaments.

Bouzarth et al. (2007) have carried out modeling and experiments on the submicron-scale flow of cilia. They found a strong coupling between cilium motion and the flow: the fluid orbit is epicyclical (related to the slow motion of the cilium) with coherent fluctuations (related to the precession rate).

Guirao et al. (2010) have shown that the alignment of ciliary beating to fluid flow direction is controlled by a mechanism in which certain cilia act as sensors for lowpass filtering of hydrodynamic forces and for generating a polarity signal for directional alignment.

Small biorobotic cilia have also been fabricated, although their hardness remains unchanged. Kongthon et al. (2010) have shown that cilia-based PDMS (polydimethylsiloxane) actuators have lower resonant frequency in liquid than in air. They show that this can be explained by added mass effects only. Shields et al. (2010) describe an experiment on PDMS biomimetic cilia stirring. The Peclet number, which is a ratio of advective to diffusive motion, is estimated to be 10; that is, their cilium flow is advection dominated. In both of these papers, phase dependent bending is absent. They find the flow within the conical cilia orbit to be non-unidirectional, but unidirectional beyond the tip, and they term it “mixing” and “pumping,” respectively. They model the flow to be a linear superposition of shear and pressure-driven flow between parallel plates.

Theoretical formulation of the equations of motion of a cilium (and flagellum) remains a difficult problem. Gueron and Liron (1992) have applied corrections to Lighthill's theory. Although a large body of analytical research on flagellum motion was carried out during the 1970s, that research (and interpretation of the research's measurements) did not predict that the motion is, in fact, three-dimensional. The finding by Hines and Blum (1978, 1983) that there is twist indicates an improvement in our understanding of how three-dimensionality evolves in the cilium actuator. Robotic modeling may be viewed as a supplementary tool to our understanding of three-dimensionality. Therefore, it would be useful to build a robotic model of the cilium where the phase-dependent deformations are produced by summing independent orthogonal oscillatory motions (IOOMs), as in typical coordinate systems (robotic simulations using coupled actuators make programming difficult). (The present report considers what these IOOMs are and explores the origin of coupled motions. Contemporary PDMS cilia actuators do not accurately reproduce the cilium motion, and it is hoped that the IOOMs will provide a solution.)

The cilium topic is of interest because it is a model of microscopic, elementary, natural swimming propulsion. A substantial amount of experimental and theoretical information is available on its physiology, motion, theoretical hydrodynamic modeling, metachronism, and control. Metachronism by itself is a very interesting example of cilium-cilium coupling. There is evidence of self-organization, as well as evidence of ionic control of cilium beating. The potential relationship of natural swimming and self-organization plus ionic control has far-reaching consequences in the sense that hydrodynamics and control may have co-evolved—see Llinas (2001).

1.2 PURPOSE OF THIS WORK

The present work addresses autonomy and three-dimensionality. The focus is on different sources of resonant oscillations. Also considered is how three-dimensionality develops in a solid surface, and how the development of this three-dimensionality and control are integrated. The approach taken is that modeling of how the different aspects of the problem are integrated as a whole is a fruitful way of understanding autonomy.

The degree of three-dimensionality and control in the cilium varies with the power and return strokes. Hence, it is important to determine their phase accurately. How long is the propulsion stroke? Per Teunis and Machemer (1994), it is $1/7$ to $2/7$ of the beat period. This finding is revisited here because the cilium motion shows that near the extremities of the power and return strokes, the outer and inner parts of the cilium change the stroke at different phases, which makes it difficult to determine the exact ends of the strokes. For self-regulation to be explored, the phase transition between the power and return strokes needs to be determined accurately.

Voltage stimulation experiments have shown that ion flow in the microtubules controls the torque produced. Theoretical work has shown that (1) the cilium motion emerges when appropriate moments are applied at the cilium microtubules, and (2) neighboring cilia interact and phased motion ensues between them autonomously. The links between autonomous regulation, ion flow-based control, and cilium motion need to be examined because they may provide clues as to how hydrodynamics and control are integrated in natural swimming.

To understand the motion of a cilium, this report brings in several tools that have not been used previously in cilium investigations. These tools—Frenet’s equation, nonlinear oscillatory modeling, biorobotics, and materials science—provide an opportunity to integrate structure, hydrodynamics, and control, whereby a more internally consistent understanding can be reached, and perhaps applied to nonlinear transduction, which is not well developed. Our physical rendition is a way to understand internal consistency when different disciplines such as hydrodynamics and control are being integrated.

In the following sections, a theoretical model on torsional oscillation of the cilium is first developed, and this is followed by a nonlinear model of the moments applied at the base. After this, the motion of the biological cilium is examined by revisiting Teunis and Machemer’s (1994) cilium orbits. The relationship of the analysis of the cilium motion to the models is examined. Cilium motion is robotically reproduced in a scaled-up model and compared with that of the biological cilium. Finally, a synthesis of the results is given and a modified fracture theory is applied to explain the origin of variation in hardness. The process of self-regulation is discussed. The report contains a substantial amount of supporting information in the appendix, which covers the following topics:

- Two-dimensional hydrodynamic modeling based on Frenet’s equations assuming the cilium to be composed of hinged links.
- Robotic exploration of the independent orthogonal oscillatory motions that produce the cilium motion.
- Development of “frictionless” actuators, continuing the theme of resonant oscillation when one expects the amplitude of oscillation and quality factor to increase.
- Hardware operation of the cilium IOOMs via analog olivo-cerebellar dynamics.
- Experimental investigation to understand how torsional modulus affects the development of three-dimensionality.
- Consideration of how the microcosm of actuation and control in the tiny paramecium’s cilium could conceivably be related to natural swimmers at higher Reynolds numbers.

2. MODELING

Here, natural swimming is defined as one where the cilium actuator is forced at the natural frequency of oscillation and the resulting motion is describable by dynamic systems, is nonlinear with the potential for chaotic motion, and has a self-regulating nature.

2.1 MODELING OF THE NATURAL FREQUENCY OF OSCILLATION OF THE BIOLOGICAL CILIUM

Consider the cilium to be a torsional pendulum (as shown in figure 1a) subjected to opposing torque τ and drag D . For small rotational angles θ ,

$$\tau = -^{\tau}k\theta,$$

where $^{\tau}k$ is a torsional spring constant. If I is the moment of inertia,

$$I\ddot{\theta} = \tau = -^{\tau}k\theta,$$

and the solution is, for $\varpi = 2\pi f_o$, with f_o being the natural beat frequency (1/s),

$$\varpi = \sqrt{^{\tau}k/I}.$$

In our case, for Reynolds number $Re \sim 0.1$ and drag coefficient C_D , $C_D \propto Re$ (I is constant),

$$\varpi \propto \sqrt{^{\tau}k} \propto \sqrt{C_D} \propto \sqrt{Re},$$

which gives

$$f_o \propto \sqrt{Re}.$$

For the same cilium in different fluids,

$$f_o \propto 1/\sqrt{\nu} = \sqrt{\rho/\mu},$$

where ν is the kinematic viscosity, μ is the dynamic viscosity, and ρ is the density of the fluid. Assuming ρ to be constant,

$$f_o = K(1/\sqrt{\mu}),$$

where K is a constant. Therefore, as μ drops, the oscillation frequency f_o increases. This relationship is compared with Machemer's measurements in figure 1b. The trend is in agreement with Machemer's (1972) measurements. In view of the variable hardness of the cilium during the power and return strokes, this relationship is approximate.

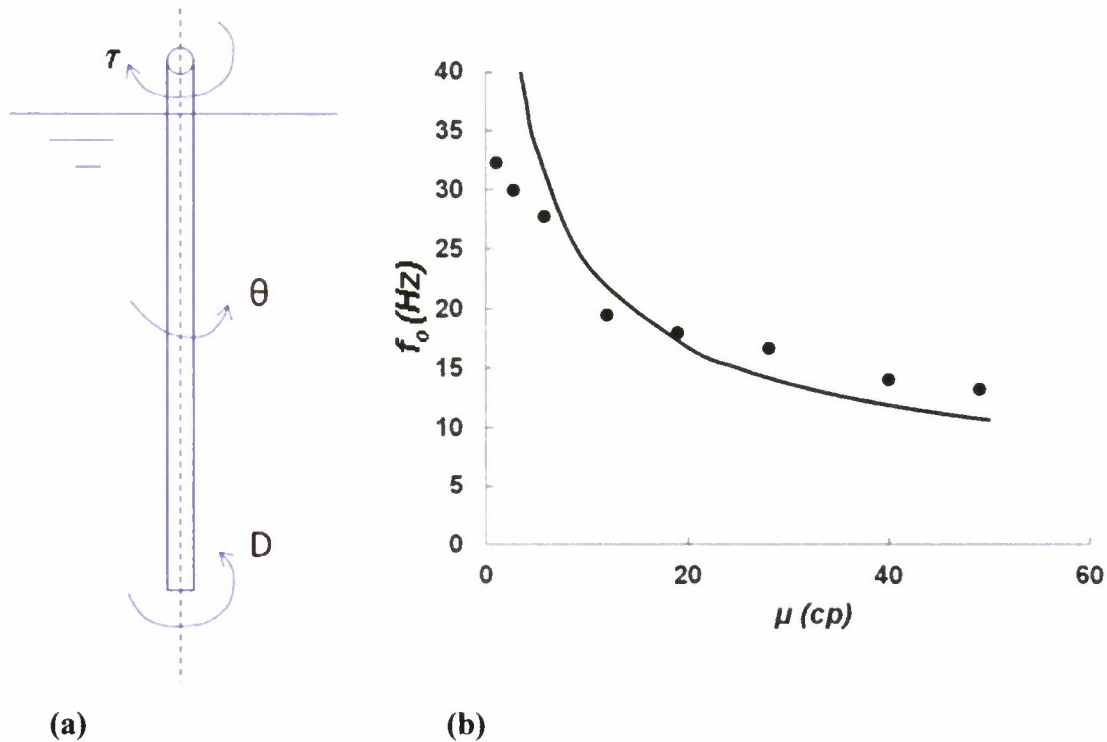


Figure 1. (a) Schematic of the Torsional Pendulum Model of the Cilium; (b) Comparison of the Model (solid line: $f_o = K(1/\sqrt{\mu})$, $K = 75$, and μ in cp) with Measurements (dots) Due to Machemer (1972))

2.2 DYNAMIC SYSTEMS MODELING OF CILIUM MOTION

In this section, olivo-cerebellar dynamics, which owes its origin to the inferior-olive (IO) neuron dynamics work of Llinas and Yarom (1981), and Kazantsev et al. (2003, 2004), is applied to the cilium motion. Direct evidence of the existence of such neurons in paramecium is lacking. However, there is corroborating evidence of a role of Ca ions in paramecium and cilium motion control (describable probably as a primitive neuron), and one can assume that each cilium has its own ion-related control. At the very least, it is noted that IO neurons are merely one of many situations in nature where equations such as that in equation (1) apply.

Following Kazantsev et al. (2003), the model of the I^{th} ion-related controller is given as follows:

$$\begin{bmatrix} \dot{z}_i \\ \dot{w}_i \end{bmatrix} = \begin{bmatrix} p_{iz}(z_i) - w_i \\ \varepsilon_{Ca}(z_i - I_{Ca}) \end{bmatrix} + \begin{bmatrix} 0 \\ -\varepsilon_{Ca} \end{bmatrix} I_{ext}(t), \quad (1)$$

where the variables z_i and w_i are associated with sub-threshold oscillations and low-threshold (Ca -dependent) spiking in olivo-cerebellar dynamics (the higher threshold (Na^+ -dependent) spiking oscillator of Kazantsev et al.'s model is not considered). The constant parameter ε_{Ca} controls the oscillation time scale; and I_{Ca} drives the depolarization levels. The nonlinear function is

$$p_{iz}(z_i) = z_i(z_i - a_i)(1 - z_i).$$

The function $I_{ext}(t)$ is the extracellular stimulus, whose amplitude and duration are used for the purpose of control (changing the motion of paramecium direction, for example). If $I_{ext}(t) = 0$ (independent oscillator), the nonlinear function is given by $p_{iz}(z_i) = z_i(z_i - a_i)(1 - z_i)$, where a_i is a constant parameter associated with the nonlinear function. Equation (1) can be written as

$$\ddot{z}_i + F(z_i)\dot{z}_i + kz_i + \varepsilon I = 0, \quad (2)$$

where F is a cubic polynomial function and k is a constant. Equation (2) bears resemblance to Lienard's oscillator (in contrast, the function F is a well-defined quadratic in the familiar van der Pol's oscillator) (Khalil, 1996; Slotine and Li, 1991). The oscillator exhibits a closed-orbit Γ_i in the state space $(z_i - \dot{z}_i)$; that is, $(z_i - w_i)$, which is also known as limit cycle oscillation (LCO), the constant parameters determining the form of Γ_i . Equation (1) is solved using the analog oscillators described in Bandyopadhyay et al. (2008).

The (z, w) waveform data are gathered from Simulink and saved into files for reading; these are z, w waveforms, their derivatives, and their second derivatives (not shown in figure 2 due to the presence of an inflection point in the first derivative). In figure 2, the phase maps are scaled to the same size as the experimental data and centered at the same point so that waveforms can be compared. The modeled phase maps are also rotated to the proper orientation, which is a 10° rotation for position data (z, w) and -55° for derivative data (\dot{z}, \dot{w}) .

The modeled states (z, w) are compared with measurements in figure 2. Note that the experimental data are for axes shown in figure 13 for the biological cilium for a given value of s . The agreement, even in the first derivative, is rather good for $a_i = 0.015$. *The simulation shows that the cilium follows a track that is describable as a limit cycle. Therefore, it has an autonomic character; the cilium is controlled without sensors.*

The $(\dot{z} = 0, \dot{w} = 0)$ location is an inflection point (figure 2b) in both the biological cilium and the modeled state map. This is a new finding and that is significant from the point of view of the nonlinear oscillatory behavior of the cilium.

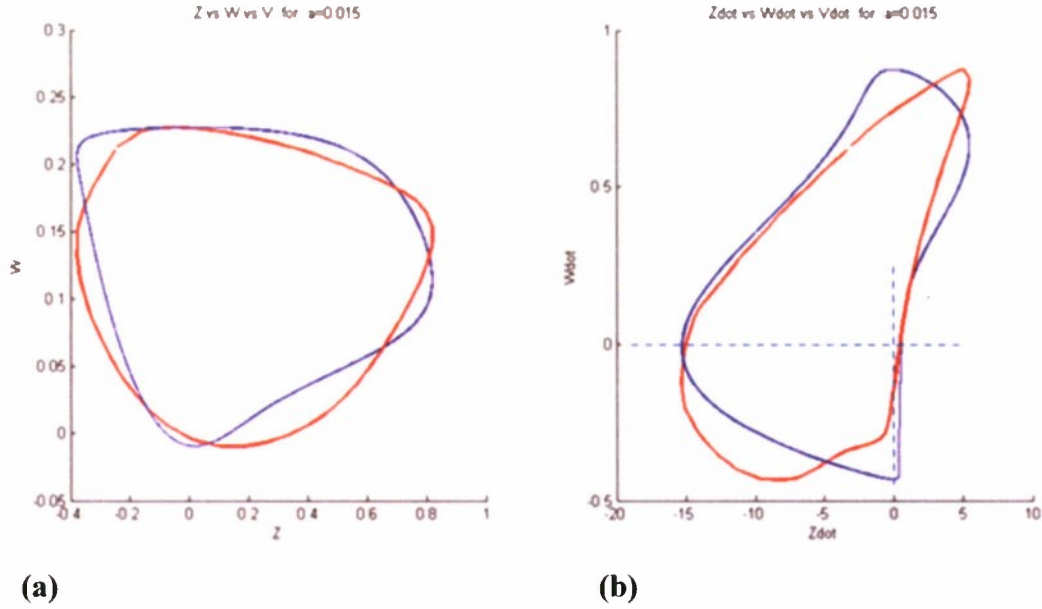


Figure 2. Comparison of the Tracks of the Cilium of a Paramecium as Measured by Machemer (1972) and Per the Present Authors' Computation of LCO (Limit Cycle Oscillation) Using the Lienard Oscillator (Equation (2))
(The model is in blue, and the cilium distal point data are in red. Position is plotted on the left and velocity on the right. The value of a_i is 0.015. (a) (z, w) , and (b) \dot{z}, \dot{w} . Arbitrary units.

The (z, w) waveforms and the attractor basins have been computed (not shown here). There is an option to show the component phases of each waveform. The user may also show a certain percentage of the data saved by Simulink, with small values showing the limit cycle and large values showing the entire limit cycle approach from the initial condition. For comparing waveforms, a small percentage (20% or lower) is most convenient. To see the entire attractor basin paths from multiple initial conditions, the user can show 100% of the data, which is a time-consuming process. These graphs may be obtained from the lead author. When the paramecium hits an obstacle, its return to natural beating would be described by these attractor maps ($I_{ext} \neq 0$).

3. BIOLOGICAL AND ROBOTIC CILIUM DATA

A rigid link modeling of the hydrodynamics of the cilium has been undertaken by our co-worker Norman Toplosky (NUWC Code 1532) (see section A.1 in the appendix). Thus far, a two-dimensional simulation has been completed, and the three-dimensional simulation results are awaited. The cilium stiffness is arbitrarily varied between the power and the return strokes. An asymmetric beating pattern is produced (figure A-2). The base force integral over the beat cycle shows some positive thrust (figure A-3). In the three-dimensional simulation, higher thrust is expected to be produced. To complement this work, the present authors undertook the approach of biorobotic simulation of the fluid-loaded cilium and an analysis of the biological cilium, drawing from the published data of Teunis and Machemer (1994).

3.1 REVISITING BIOLOGICAL CILIUM DATA

3.1.1 *Collection and Processing of the Teunis and Machemer (1994) Data*

To revisit Teunis and Machemer's (1994) experiments, their orthogonal cilium stereo-microscopy pictures were electronically digitized in pixels; the cilium motion given by the position vector (in pixels) of a space curve $r(s,t) = \{x(s,t), y(s,t), z(s,t)\}$. This is shown for the propulsion longitudinal plane in figure A-4 of the appendix. The cilium is divided into 20 segments (initially of non-uniform spacing). Define s as the axial length from the base to the distal point (L) of the particular cilium segment; also define an orthogonal coordinate system (x, y, z) that represents the propulsive (or stream-wise), vertical, and spanwise directions, respectively, and t is time.

The University of British Columbia (UBC) Biology Department has produced a useful *gif* animation of the cilium motion using these stereoscopic data (see figure 13a, left column, 326-kB *gif* image). In this report, the term "revisited TM data" pertains to our (pixel) digitization of the cilium motion as it appears in the UBC *gif* graph, with the data due to Teunis and Machemer (1974), and their subsequent parametric processing and smoothing. The graphs used for digitization are from the UBC *gif* file because the cilium position, velocity, and acceleration do not visually exhibit any spatio-temporal kink (smooth gradients of time and length).

Due to cilium bending, initially, the positions (in pixels) along the length were not equally spaced in the longitudinal and top-view planes. For this reason, the digitization had to be processed in the following manner. With cilium bending, the $(y(s,t))$ distances could be determined more accurately from the $(x(t), y(t))$ view (side view), and the $(x(s,t), z(s,t))$ position values could be determined from the $(x(t), z(t))$ view (top view). The initial length was obtained from the three coordinates obtained this way. From the polynomial fits at each time step (TS), the cilium was digitized at equal length intervals $(r(s, t))$. The data were further smoothed along the orbits. Subsequently, a three-dimensional parametric fit (figure 3c) was applied; see Zwillinger (1996). The result was a smoothed position distribution both along the cilium lengths at each time step and also of their rotational orbits obtained from position vectors at equispaced s locations.

The improvement in the accuracy due to axial and rotational track smoothing of the cilium position vector data is given in the tables A-2 through A-4 in the appendix. The cilium length of $17\text{ }\mu\text{m}$ is maintained at all time steps (the diameter is $0.25\text{ }\mu\text{m}$) (Pernberg and Machemer, 1995); the local lengths are also maintained at all positions along the length of the cilium at all time steps. Figure 6 of Machemer (1972) shows that the biological cilium data used here are for water (viscosity of 40 cP). Figure 3 shows the variation of the cilium surface length for one beat cycle, dividing the cilium into 10 lengths; the top plot shows the raw data, the middle plot shows the smoothed data and the bottom plot shows the parametric fit to the data smoothed along length and orbit.

Top and side views of biological cilium data, with time step (TS) numbers, are shown in figure 4. These plots show that the beat period is composed of two kinds of cilium forms; the cilium remains fairly straight from TS 38 to 14 and its form is substantially curved from TS 14 to 38. The cilium would impart greater momentum into the fluid when it produces higher velocities in the outer region; therefore, TS 38 to 14 are likely to indicate the power stroke. During the power stroke, the cilium stays fairly close to the ($z = 0$) plane. Therefore, the cilium trajectory is shaped approximately like the capital letter D. This observation is used for the robotic simulation; see section A.3 in the appendix.

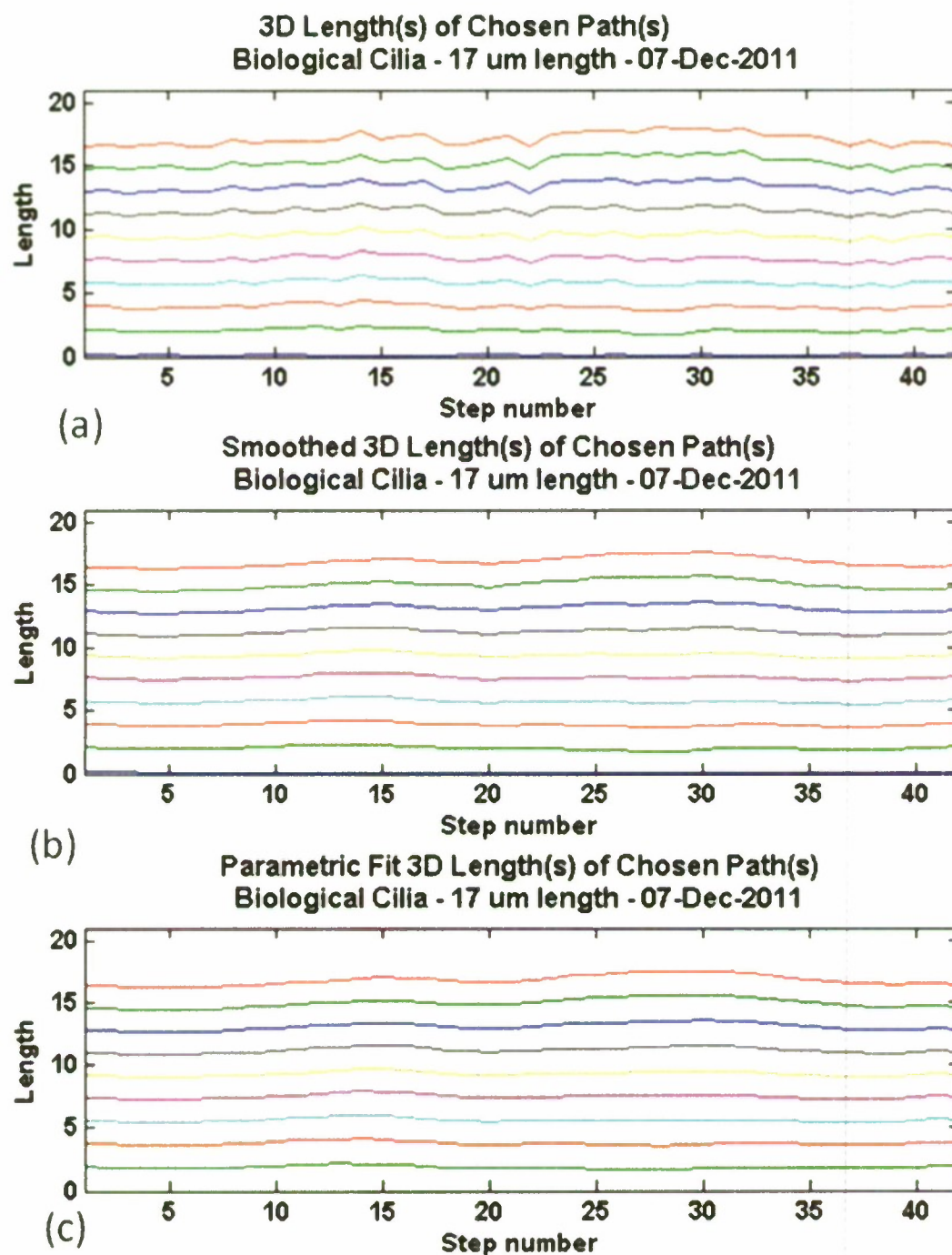


Figure 3. Variation of the Cilium Axial Distance from the Base with Beat Phase (= Time Step Number) in the Digitized Biological Cilium in the Revisited TM Data—(a): Raw Distribution; (b): After Smoothing Along Cilium Length; (c): After Parametric Fit of the Closed Orbits to Smoothed Axial Data

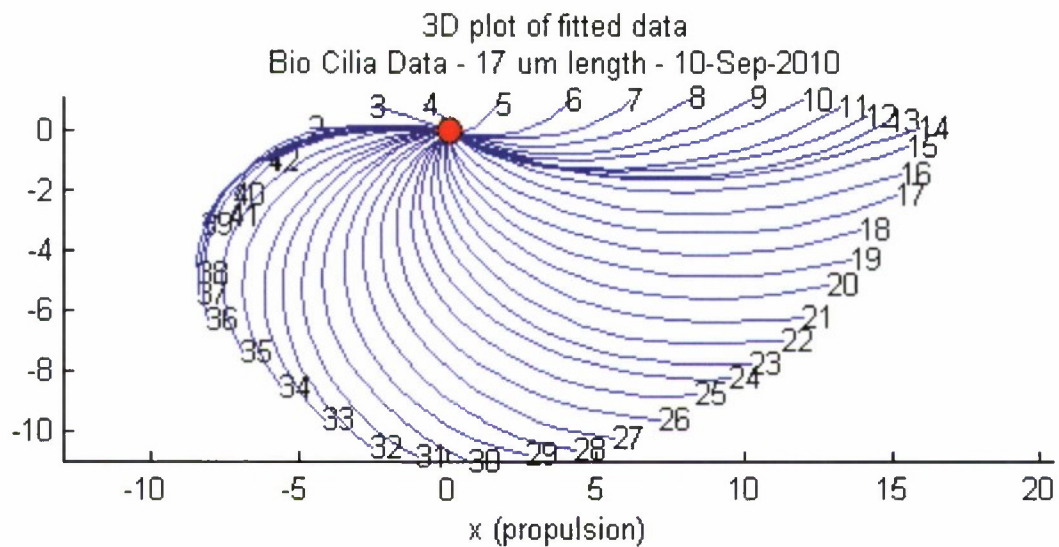


Figure 4a. Top View (x, z) of the Cilium Beat Cycle in the Revisited TM Data (Axes: μm .)

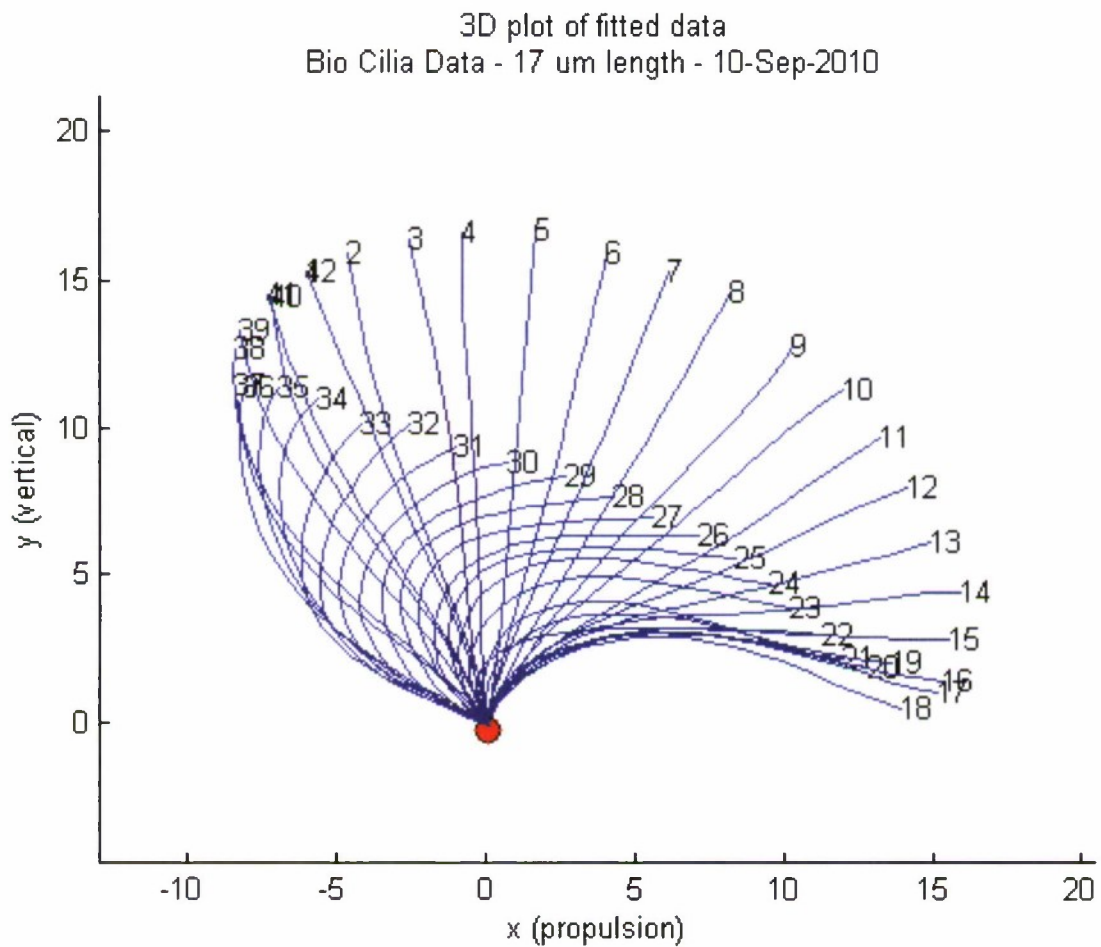


Figure 4b. Side View (x, y) of the Cilium in the Plane of the Power Stroke During the Beat Cycle in the Revisited TM Data (Axes: μm .)

3.1.2 Analysis of the Teunis and Machemer (1994) Data

Using the smoothed biological cilium data, the velocities and accelerations in the $(x(t), y(t), z(t))$ directions were calculated. The units are as follows: length (μm), velocity ($\mu\text{m/s}$), acceleration ($\mu\text{m/s}^2$), curvature ($\text{rad}/\mu\text{m}$), and torsion ($\text{rad}/\mu\text{m}$).

The straightness of the cilium, which is a measure of its hardness, is considered in figure 5. The cilium is divided into 20 axial segments. Figure 5 shows the distributions of (a) the angle of the velocity from the x -axis, and (b) the angle between the axial length segments and the x -axis. See section A.2.5 for definitions. In (a), the velocity angles are nearly equal in all length segments from 45° to 0° to 90° values, a duration that is identified as the power stroke. On the other hand, during the return stroke, the velocity angles vary widely from 90° to 180° to 45° . The velocity angles along the cilium length fan out, pivoting near TS 13 in (a). The significance of this phase is considered later. In (b), the cilium position angle also varies widely during the return stroke.

The velocities are shown in figure 6, and the accelerations are shown in figures 7 and 8. During the power and return strokes, the velocities lie approximately in two separate orthogonal planes. The velocities are high during the power stroke and are reduced during the return stroke. Shields et al. (2010) report tip speeds in their rigid biological cilium of $700\text{--}800\ \mu\text{m/s}$ and tracer speeds of $200\ \mu\text{m/s}$. Figure 7 shows that the cilium produces an inward "tornado," with the magnitude increasing away from the base. Two-dimensional cilium motion cannot produce the tornado. The acceleration limits drop by a factor of 3 if the cilium length is reduced from 50 to $17\ \mu\text{m}$.

The velocity field folds at $(\dot{x} = 0, \dot{y} = 0, \dot{z} = 0)$. The time instant occurs nearly at the shift from the power stroke to the return stroke. This time instant appears in figure 2b as a point of inflection. As per the nonlinear modeling given earlier, this phase denotes neutral equilibrium in a nonlinear pendulum (this is the vertical position in a nonlinear pendulum if the string is replaced by a solid rod; the topology is a saddle—a neutral equilibrium position that is very sensitive to disturbances; 180° later, it is a focus—a stable phase). The physical significance of this phase is further explored later.

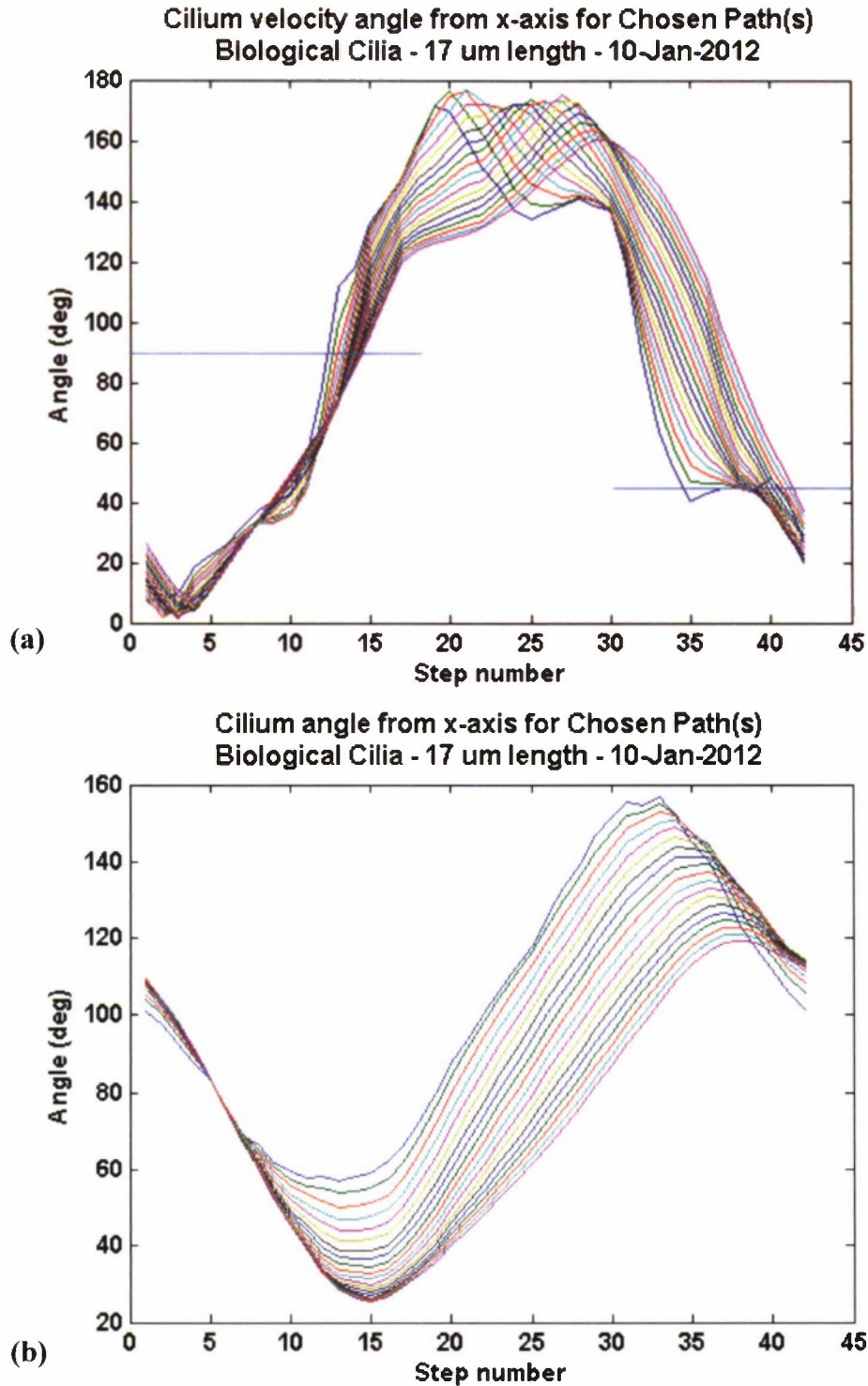


Figure 5. Variation of the Local Axial Angle of the Orbital Velocity and Position of the Biological Cilium Length Segments with Respect to the x-Axis (Power Stroke Axis) During the Beat Cycle in the Revisited TM Data (The graph is independent of cilium length (50 or 17 μm). Color code: Different color signifies every 5% of cilium length starting from the base. The horizontal lines in (a) are at 45° and 90° angles.)

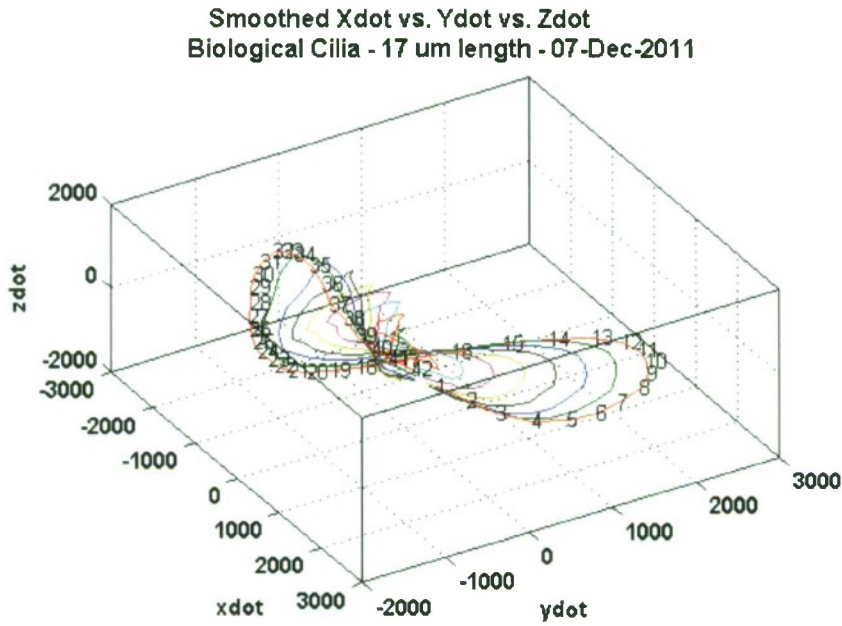


Figure 6. Variation of $X\dot{d}(t)$ ($= \dot{x}(t)$) vs $y\dot{d}(t)$ ($= \dot{y}(t)$) vs $z\dot{d}(t)$ ($= \dot{z}(t)$)
Using the Revisited TM Data
(Color code: Different color every 10% of cilium length
starting from the base; velocities are in $\mu\text{m/s}$.)

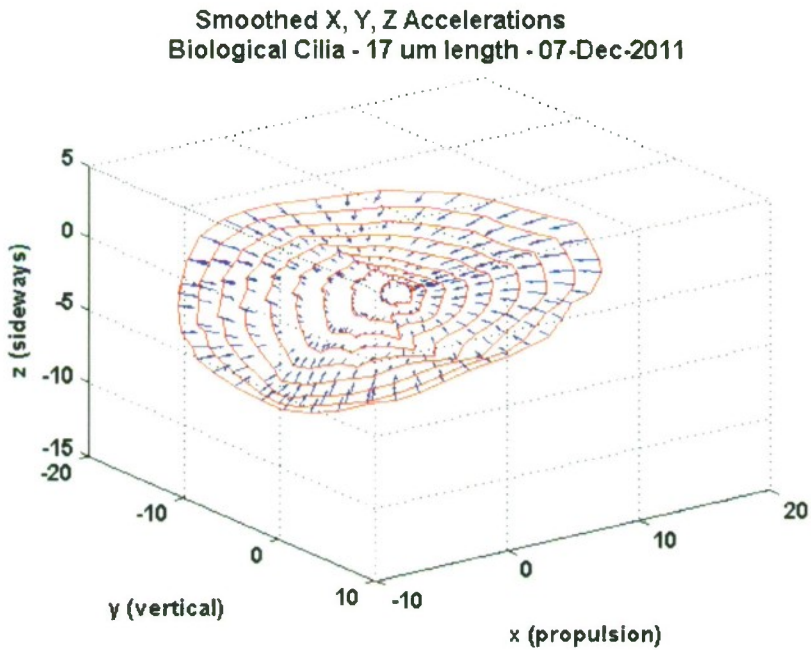


Figure 7. Inward Acceleration for the Revisited TM Data
(Color code: Red loops of constant cilium length appear every 10% of
cilium length; acceleration arrows are in blue; acceleration is in $\mu\text{m/s}^2$.)

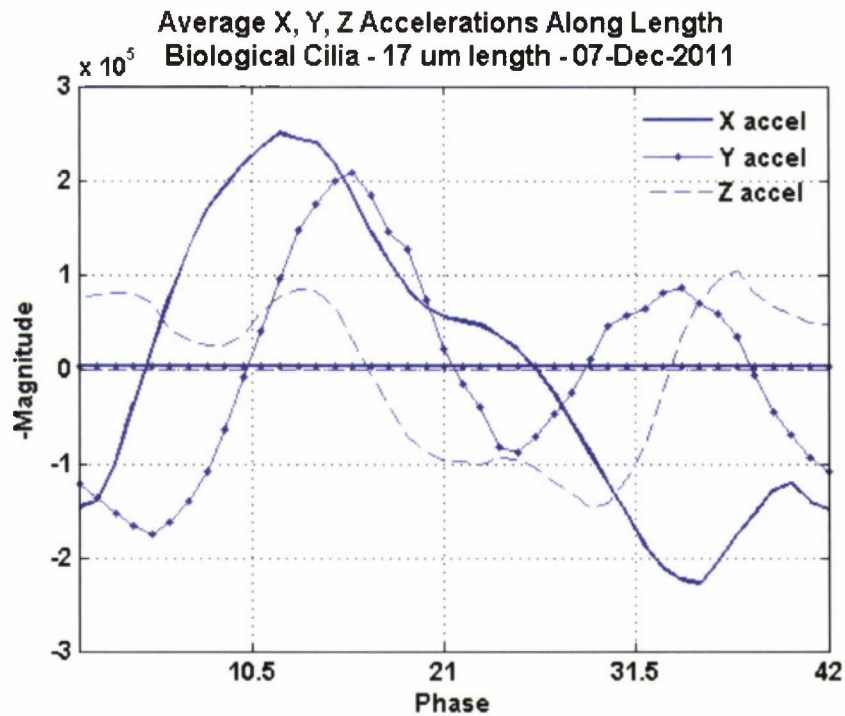


Figure 8. Calculated Acceleration Components ($\mu\text{m/s}^2$) in the Biological Cilium Using the Revisited TM Data

How long is the power stroke? There is some ambiguity as to the boundary of the power stroke. Teunis and Machemer (1994) do not explicitly define the extent of the power stroke but seem to suggest it to be from where x -acceleration crosses the zero value to where it reaches the maximum value. Defining the power stroke as when the cilium is moving in the negative propulsion direction seems most reasonable, thereby pushing the cilium in the positive propulsion direction. This is also when acceleration is increasing in figure 8—approximately from TS 35 to 12. (The end of the power stroke can be ambiguous because the proximal part starts the return stroke prior to the distal part.). The total duration of the power stroke is 0.50 of the beat period, which is larger than the range (0.14 to 0.28) arrived at by Teunis and Machemer (1994). The extent of the power stroke cannot be accurately determined from the cilium position data alone; accurate calculation of acceleration is a more reliable indicator.

An average radius of the cilium R_{avg} was defined, as given in section A.2 of the appendix. The motion of the cilium is modeled as a disc whose velocity varies radially (Wakeling and Ellington, 1997). The disc area is divided equally at R_{avg} such that the momentum imparted to the fluid by the inner and the outer areas is equal. The variation of R_{avg} with phase is shown in figure 9.

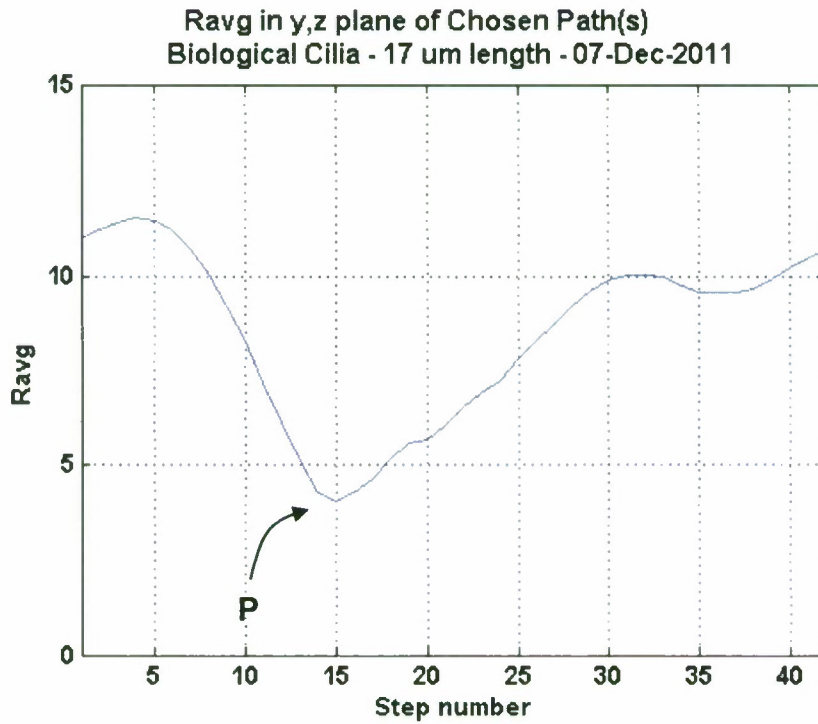


Figure 9. Variation of Calculated Average Radius (R_{avg} in μm) of the Biological Cilium During the Beat Cycle in the Revisited TM Data
(Location P is a point of inflection on the cilium at TS 14; see figure 17a.)

The R_{avg} (this is a curved length radius average) values were multiplied by the local velocity in the propulsion direction (x-axis) to determine the directionality and relative scale of the momentum imparted to the fluid. The results are shown in figure 10. At TS 15, R_{avg} is a minimum; P is a point of inflection on the cilium at TS 14, just prior to when R_{avg} is a minimum. The variable ($\text{velocity} \times R_{avg} \text{ length}$) crosses zero at TS 35 and 14 (figure 10). This is an indication that the power stroke extends from TS 38 to 14, and the return stroke extends from TS 14 to 38. Recall that the demarcating phases (TS 14 and 38) have been identified as saddle and focus, respectively. Figures 9 and 10 show that the reduction of R_{avg} (the reduction in the hardness causing an “unfurling” of the cilium, as discussed later) is a mechanism for reducing drag during the cilium return stroke; conversely, the full extension of R_{avg} (increase in hardness) is a mechanism for maximizing the output power during the power stroke. The x-acceleration in figure 8 has maxima and minima at the boundaries of the strokes. The use of R_{avg} has produced consistent results. Considering the area about the zero crossings, the thrust efficiency (the difference between the positive and negative areas divided by the total area under the curve) is estimated to be 0.125.

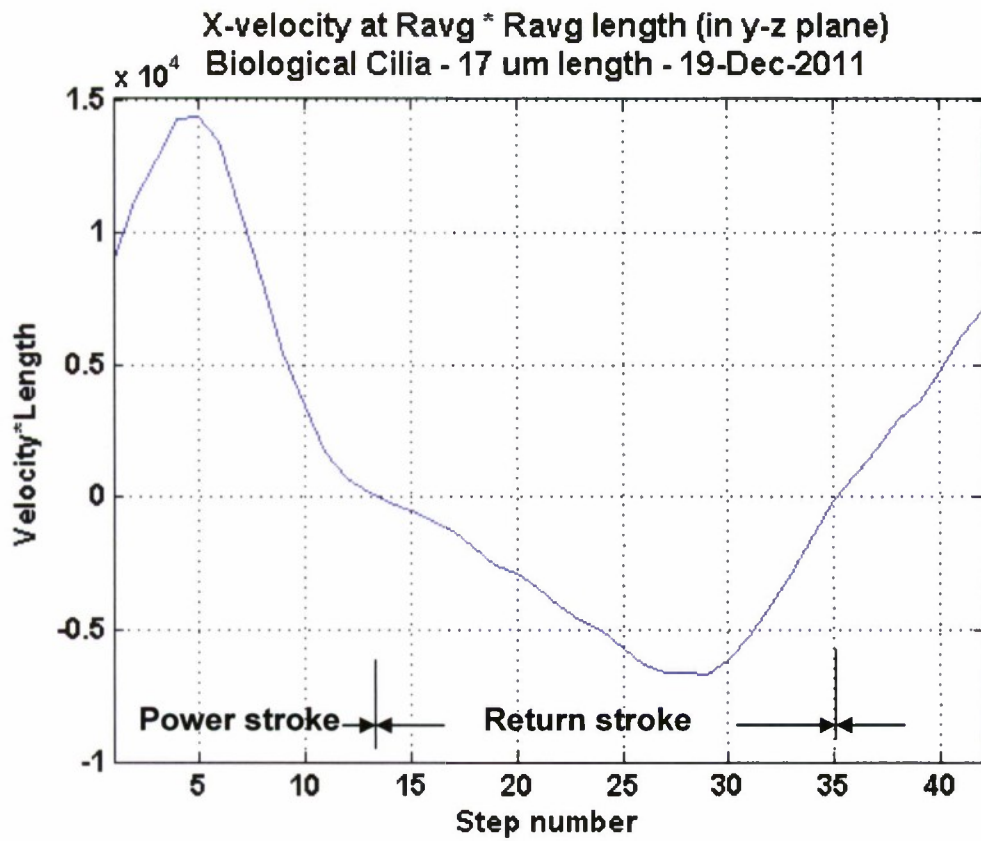


Figure 10. Calculated Variation of the Variable (Velocity $\times R_{avg}$ in $\mu\text{m}^2/\text{s}$) of the Biological Cilium in the Revisited TM Data

3.2 ROBOTIC CILIUM

Before arriving at the final design of the cilium drive, several studies were carried out to better understand the nature of cilium motion. These included a computer-aided design (CAD) simulation, the development of a *hardware D-cam pendulum*, development of an early drive mechanism using orthogonal bucket handles, and a robotic cilium design for bending motion (see appendix sections A.3 and A.4 for details of these studies).

The inset in figure 11 shows a set of independent orthogonal oscillatory motions (IOOMs) in a Cartesian coordinate system that has been used to generate the motion in the final design of the biorobotic cilium. It has two roll oscillations in orthogonal x - and z -axes. Also, a twist oscillation in the y -axis and a bending oscillation have been added to account for the variation of R_{avg} during the power and return strokes.

In section A.4 of the appendix and in the DVD in Bandyopadhyay (2009), it is noted that these IOOMs have the ability to reproduce the motion of the pectoral fins in larger swimming animals as well; see section A.7. Among the robotic IOOMs, the x and z roll motors and the twist motor apply moments, and the push-pull forces are applied to generate in-plane bending.

Figure 11 is a photograph of the four-oscillating-motor apparatus producing the actuations shown in the inset. Each motor (Maxon) has position encoders, and the torque can be determined from the input current. The bending oscillation is produced by a pair of sliding flats as shown in figure A-9 of the appendix; a flexible tube encapsulates the push-pull sliding flats. The robotic cilium length is 0.21 m.

Figure 12 is a strobe picture sequence of cilium position during the return stroke produced in the apparatus shown in figure 11. The strobe picture may be compared with figure 4b.

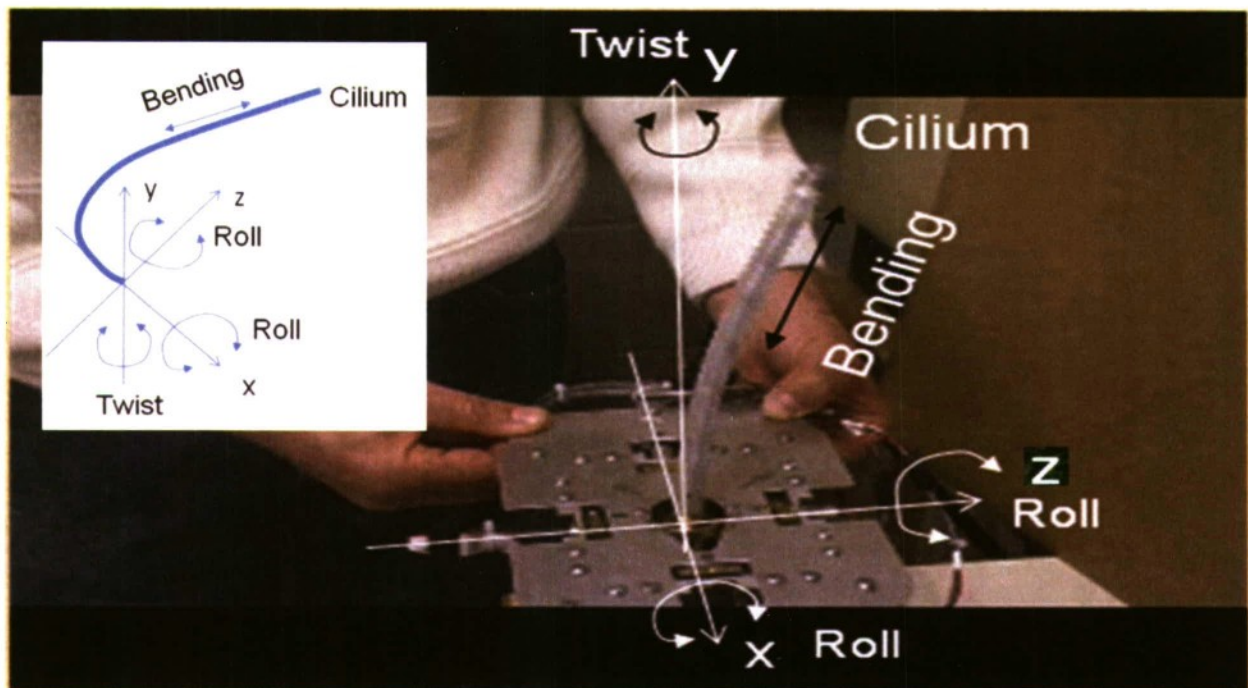


Figure 11. Photograph of the Scaled-Up Model of a Single Robotic Cilium
(The x- and z-motors (roll) lie in the plane of the horizontal aluminum frame and are visible. The y-motor (twist) and the bending motor lie underneath the flat aluminum frame. Inset: Elementary orthogonal oscillations of a cilium protruding from a surface (x, z). Power stroke lies predominantly in the (x, y) plane; (y, z) is the transverse plane.)



Figure 12. Strobe Picture of the Cilium in the Apparatus Shown in Figure 11
(Return stroke is shown; -X is upstream direction.)

3.3 COMPARISON OF ROBOTIC CILIUM AND BIOLOGICAL CILIUM

In this section, the motions of the scaled-up robotic cilium are compared with those of the biological cilium. Note that the robotic cilium motion in air is being evaluated when it is made to reproduce the fluid-loaded cilium. The beat period of the robotic cilium is immaterial and is lower by a factor of 10 to remove inertia effects. The units in the biological cilium are: length (μm), velocity ($\mu\text{m/s}$), acceleration ($\mu\text{m/s}^2$), curvature ($\text{rad}/\mu\text{m}$), and torsion ($\text{rad}/\mu\text{m}$). The units in the robotic cilium are length (m), velocity (m/s), acceleration (m/s^2), curvature (rad/m), and torsion (rad/m).

3.3.1 Comparison of Position

In figure 13a, side and top views ($\{x(t), y(t)\}$ and $\{x(t), z(t)\}$ distributions, respectively) of cilium position during the beat cycle are compared for the biological cilium and the robotic cilium. The green arrow indicates the power stroke, and the red arrow indicates the return stroke. The patterns in the biological cilium and robotic cilium are similar.

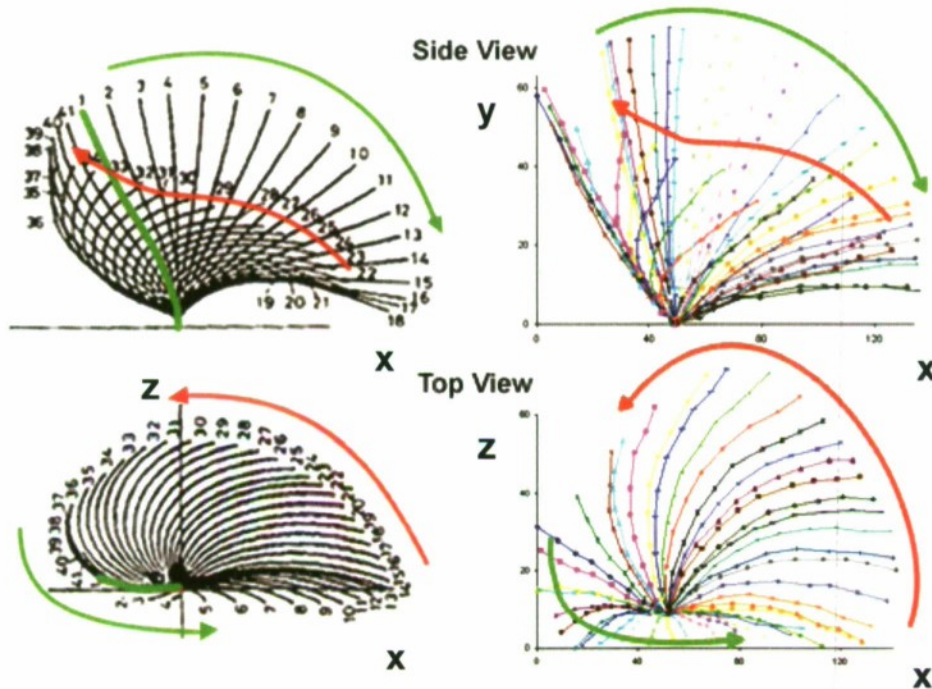


Figure 13a. Comparison of the Biological Cilium (left column) and Robotic Cilium (right column) Positions—Side View: $(x(t), y(t))$, and Top View: $(x(t), z(t))$ (x -axis is in the horizontal direction; green arrow is the power stroke; red arrow is the return stroke. Color code: Different time steps. Biological cilium is the UBC version of Teunis and Machemer (1994) data.)

Figures 13b and 13c compare the biological and robotic cilium rotational tracks; in figure 13b, 20 positions along the length of the cilium are shown; in figure 13c, 3 locations are shown. The topology in figure 13b has a variable precession rate, and the coupling between the cilium beating and the precession rate (Bouzarth et al., 2007) that the fluid particles experience has a cyclic variation. The topology resembles a bent horn, but is not easily describable by a complex Fibonacci function although a start from negative integers gives the bending.

3D Path fits with respect to time
Normalized bio and mechanical cilia - 14-Dec-2011

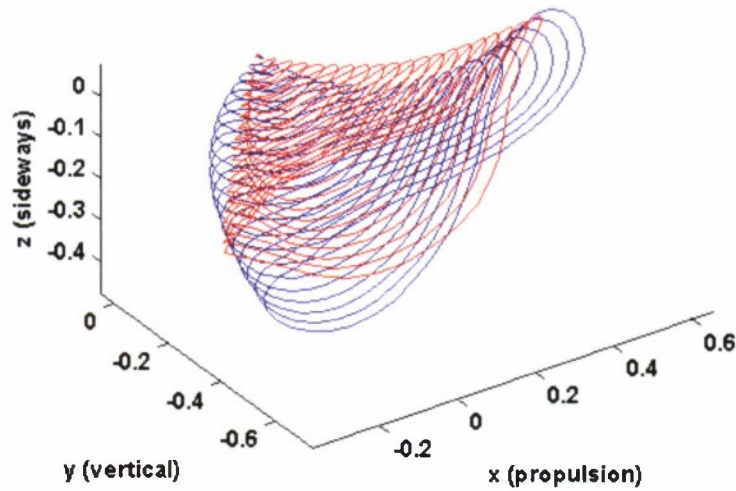


Figure 13b. Comparison of Tracks in the Biological Cilium (blue) and Robotic Cilium (red)

3D Path fits with respect to time
Normalized bio and mechanical cilia - 14-Dec-2011

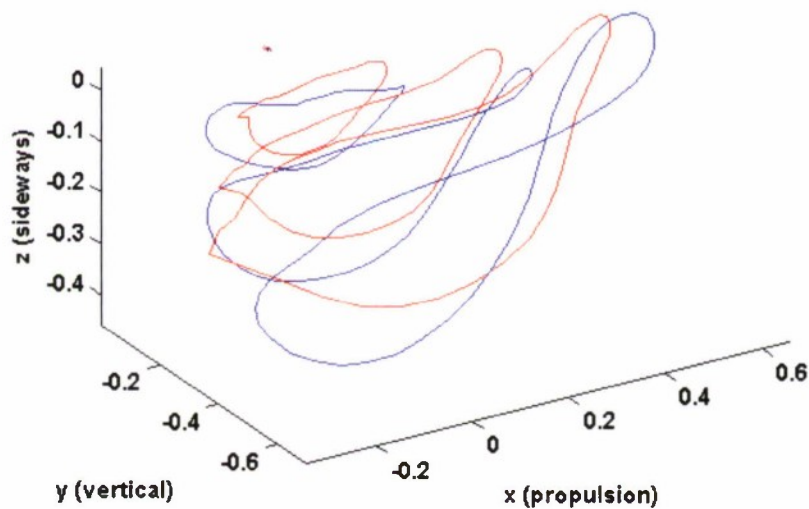
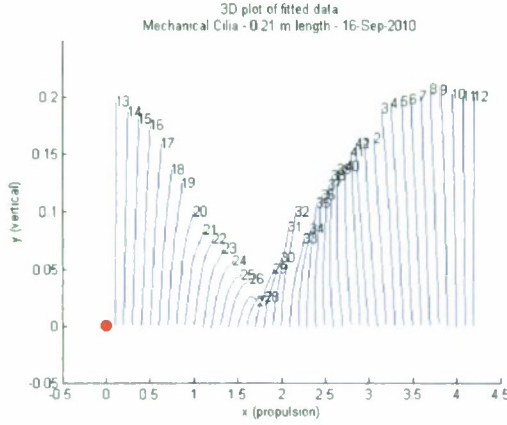
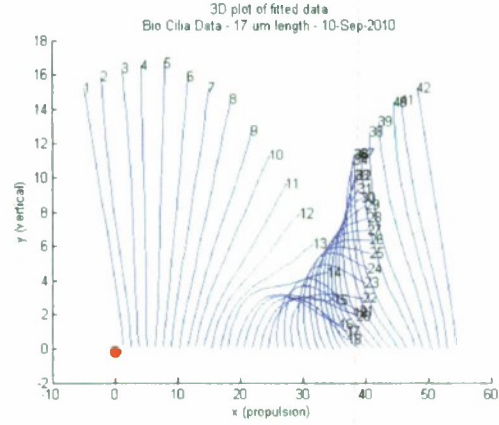


Figure 13c. Comparison at Cilia Axial Distances of $S/L = 0.33, 0.66$, and 1.0
(The base ($S/L = 0$) is indicated by the dot; blue: biological cilium; red: robotic cilium.)

Figure 14 shows the projection of the cilium on the propulsion plane. (In a redesigned version of the cilium, the bending amplitude has been increased, which would allow better agreement with the biological cilium in figure 14.) The cilium is precipitously losing its hardness at $TS > 13$. It is suspected that in the biological cilium, the material property is changing abruptly at $TS > 13$, over the beat cycle. The torsional pendulum and the autonomic modeling given earlier imply that the cilium is acting like a spring, storing and releasing energy during the return and power strokes, respectively. This view will be synthesized later.



(a) Robotic Cilium



(b) Biological Cilium (Revisited TM Data)

Figure 14. Comparison of the Robotic and Biological Cilium Positions at Each Time Step on the Longitudinal Plane
(The red dot shows the base location; the base cilium is shifted horizontally to avoid clutter.)

3.3.2 Comparison of Curvature and Torsion

Define $r(s, t)$ as the position vector of a point on the surface of the cilium, with primes denoting the derivatives with respect to t , and \mathbf{x} denoting the cross product; $||$ as magnitude, sign is retained. The following equations were used to calculate curvature and torsion for the biological cilium and the robotic cilium data (Zwillinger, 1996). Curvature is defined as

$$\kappa = \frac{||r' \mathbf{x} r''||}{||r'||^3}. \quad (3)$$

Torsion is defined as

$$\tau = \frac{r' \cdot (r'' \mathbf{x} r''')}{||r' \mathbf{x} r''||^2}. \quad (4)$$

Curvature measures the deviance of a curve from being a straight line relative to the osculating plane. In the elementary differential geometry of curves in three dimensions, the torsion of a curve measures how sharply it is twisting. If the torsion is zero, the curve lies completely in the same osculating plane (there is only one osculating plane). Note that the curvature and the torsion of a helix are constant; when they are not constant, the geometry is not helical.

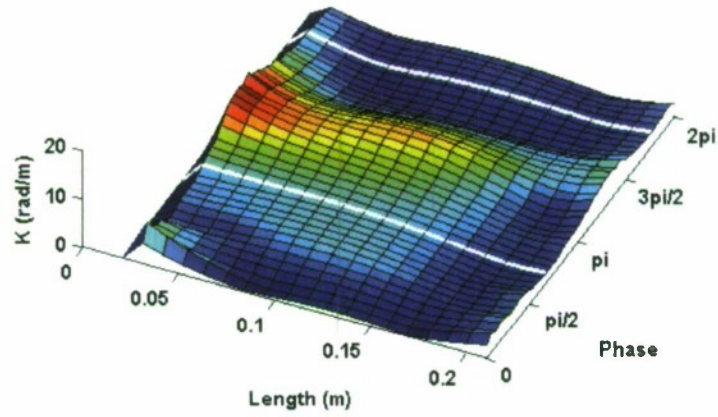
Curvature K and torsion T in the robotic and biological cilium are compared in figures 15 and 16. The biological cilium's curvature and torsion shown are from the revisited TM data. The white lines in figures 15 and 16 indicate the boundaries of the power and return strokes; the return stroke lies between the white lines. These results are different from those of Teunis and Machemer (1994). In our definition, the power and return strokes are of equal extent—not 1/7 to 2/7 for power, as given by Teunis and Machemer. In figures 15 and 16, TS 1 and 42 are assigned phase of 0 and 2π , that is, the phase at the n^{th} time step is $\phi = 2n\pi / N$, where $N (= 41)$ is the total number of time steps.

In figures 15 and 16, for the robotic cilium data after lowpass filtering, $0 \leq K \text{ (rad/m)} \leq 10.8117$, $-1.78 \leq T \text{ (rad/m)} \leq 35.87$. For the biological cilium data after lowpass filtering, $0 \leq K \text{ (rad/}\mu\text{m)} \leq 0.2178$, $-0.0729 \leq T \text{ (rad/}\mu\text{m)} \leq 0.4834$. The minimum values are in blue and the maximum values are in red. The biological cilium and the robotic cilium have approximately similar curvature and torsion distributions.

The calculation of curvature is consistent with the conclusion of Teunis and Machemer in that there is little curvature during the power stroke. This finding can be further verified by looking at the position data in figure 14. The torsion calculation also matches the conclusions above. In the biological cilium, curvature is high near the base after the return stroke has started. Torsion reaches a peak approximately halfway along the length when the power stroke ends (marked as point P in figure 16b).

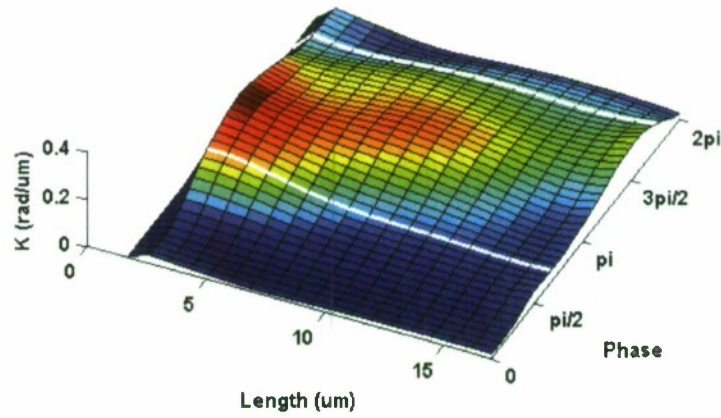
Curvature and torsion limits widen if the cilium length is reduced from 50 to 17 μm . Teunis and Machemer (1994) state that curvature and torsion are small during the power stroke (that is the cilium is stiff). They state that, “Both curvature and torsion return to minimal values by the beginning of the power stroke” (see figures 15 and 16).

Curvature
Mechanical Cilia - 0.21 m length - 08-Dec-2011



(a)

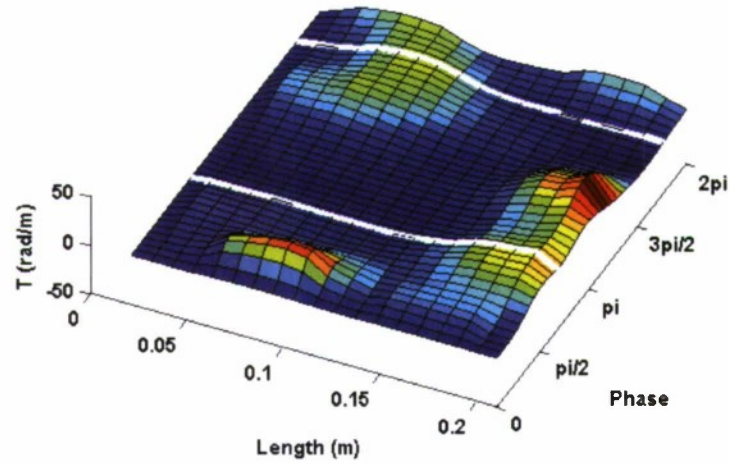
Curvature
Biological Cilia - 17 μm length - 08-Dec-2011



(b)

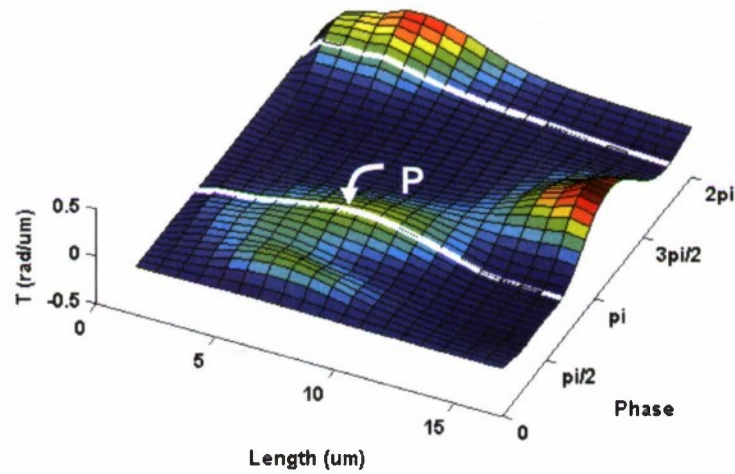
Figure 15. Comparison of the Curvature of the Robotic Cilium (a) and the Biological Cilium (b) Using the Revisited TM Data (See text for color code.)

Torsion
Mechanical Cilia - 0.21 m length - 08-Dec-2011



(a)

Torsion
Biological Cilia - 17 μm length - 08-Dec-2011



(b)

Figure 16. Comparison of Torsion in the Robotic Cilium (a) and the Biological Cilium (b)
(See text for color code; P is a point of inflection on the biological cilium (see figure 17).)

4. SYNTHESIS OF RESULTS

4.1 MODELING THE INCREASE AND DECREASE OF THE BIOLOGICAL CILIUM'S HARDNESS

The curvature and torsion results are synthesized in figure 17 to understand the behavior at the transition from the power to the return stroke when the hardness of the cilium changes precipitously.

The model schematic in figure 17 shows projections of the cilium onto the propulsion plane at TS 9, 14, and 16. These are copies from figure 14b. Between TS 13 and 14, the time derivative of the angle subtended by the cilium at the base changes sign (the cilium positions converge in figure 14b). This is depicted in figure 17 by the change in the sign of the moments applied at the base m . The directions of velocities V of the cilium and of the drags D acting on it are shown. At TS 14, while the lower part of the cilium turns anti-clockwise, the distal part turns in the opposite direction. As a result, a point of inflection is produced in between (marked as P) where the finite radius of curvature r changes sign. The cilium precipitously droops after TS 14, which indicates a decrease in hardness. The cilium is straight during the power stroke. Therefore, the question is: How does the hardness drop and recover in every beat cycle? This process is modeled in the insets P, P1, and P2 in figure 17a and in figure 16b by applying fracture mechanics.

Figure 16b shows that at point P curvature is not large, but torsion reaches a peak because the cilium is being twisted in the transverse plane. This is shown in the insets in figure 17a. Inset P shows that at P, the neutral plane of stress undergoes a reversal in compressive C and tensile T stresses. The two ends of P also experience a reversal in the sign of the applied torque τ between the cilium base and the distal point. Inset P1 shows that, as a result, two otherwise parallel circular cross-sections shear and open ajar due to the switching of the regions labeled C and T .

The literature suggests that in the 9+2 axoneme the central microtubule pair is responsible for hardness control. It can also be surmised that motor protein molecules climb up the microtubule, find attachment spots, and lock (Cordova et al., 1992). This process is modeled in figure 17b and inset P2 in figure 17a. The circular part of inset P2 shows the central microtubule pair (CM_{a14} and CM_{b14}) and the cross-bridge link (CB_{P14}). The presence of many such cross-bridge links along the central microtubule pair increases the moment of inertia I , increasing the property GI , which is responsible for resistance to torsion, where G is the modulus of torsional rigidity of the material. (The cross-bridges are similar to cross-links in polymers where they are closer when unstressed, and the polymer chain is straightened when the links are pulled apart by the application of stress.)

It is modeled that, when torsion at P reaches the maximum value, the cross-bridge attachment cracks; this is shown in the boxed part of inset P2. The cross-bridge at location P at TS 14 is the proverbial "last straw"—when the cross-bridge breaks, there is no hardness left for the power stroke to continue. Inset P2 shows how a crack develops (the sphere is the foot of the cross-bridge) at the sites where the cross-bridge is attached. The cross-bridge motor protein and the host microtubule site are of dissimilar materials conformationally held in place.

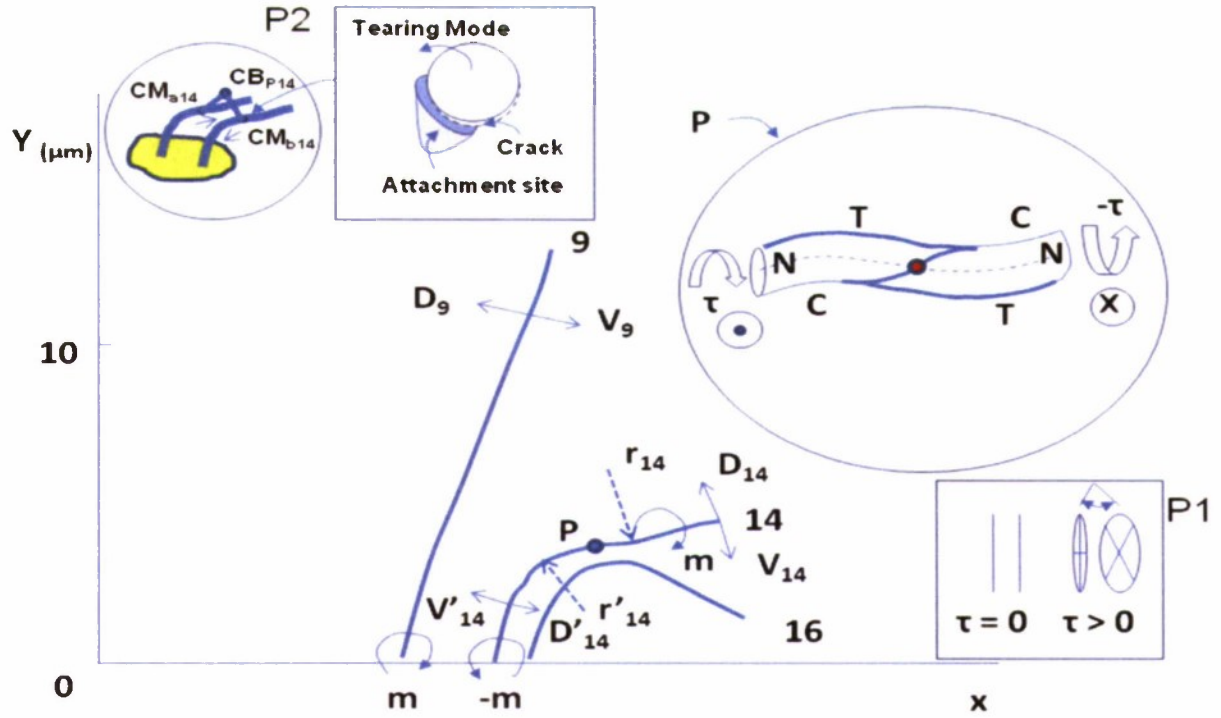


Figure 17a. Schematic of Compression-Tension Neutral-Plane Flipping at Point P on the Cilium at the Beat Phase of Neutral Equilibrium (See Inset P)
 (Symbols: 9, 14 and 16 are time steps; m and $-m$ are moments in the x - y plane at the base; D , V , and r are drag, velocity, and the radius of curvature; the prime sign (') denotes values near the base; C and T are compressive and tensile stresses; and N = neutral plane. The cilium is shifted along X with time step to avoid clutter. Left inset: CM_{a14} is the central microtubule a at TS 14; CM_{b14} is the other central microtubule of the pair at TS 14; CB_{p14} is the cross-bridge at the point of inflection P at TS 14. The cross-bridge link can be expected to fail first at the point marked by the red dot in inset P .)

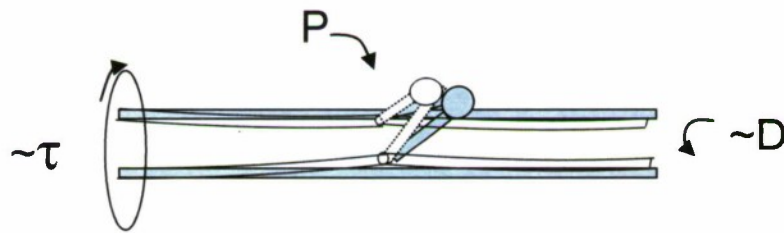


Figure 17b. Modeling of Cross-Bridge Link Between the Pair of Central Microtubules (the 2 of the 9 + 2)
 (Only the cross-bridge at point P is shown; this is the only one that cracks because torsion reaches high values at this point; other cross-bridges add to the hardness, but they do not crack because the torsion is not high (the region near the cilium tip is ignored). Broken lines represent later times. Curvature is small near point P at TS 14; therefore, planar vibrations have a negligible effect on cracking.)

One expects cracks to develop where the cross-bridge is attached to the microtubule and not at its apex because the microtubule attachment site has to be vacated fully for the new beat cycle to resume accepting a new cross-bridge attachment. Our modeling considers the cross-bridge cracking at the attachment site at TS 14 at point P. The model includes cross-bridges all along the length of the microtubules, but only the one at the point P at TS 14 cracks at the contact site and needs replacing.

4.2 MODELING OF THE CROSS-BRIDGE DETACHMENT/SOFTENING

As per Karp (2005), one end of the protein attaches to one microtubule and the other end to another microtubule, creating a cross-bridge structure. Cordova et al. (1992) give an electrostatic model of the cross-bridge attachment and detachment although not in the context of the paramecium's cilium beating. Here, fracture mechanics are applied to model the detachment. The cross-bridge-microtubule contact is modeled to be brittle (like glass), rather than plastic (like metal); in other words, Griffith's law (1920) applies and Irwin's (1948) does not. Griffith's law states that the product of fracture stress and the square root of the crack length remains constant as the crack progresses until the difference between the surface and elastic energy reaches the peak value, at which point failure occurs.

Griffith's relationship may be applied as follows:

$$\sigma_f = \frac{C}{\sqrt{a}}, \quad (5)$$

$$C = \sqrt{\frac{2E\gamma}{\pi}}, \quad (6)$$

where σ_f is the stress at fracture, a is the crack length, C is a constant, E is Young's modulus of elasticity ($= 2$ GPa for polyethylene; $= (10 \text{ to } 30) \times 10^9 \text{ N/m}^2$ for myosin (Adamovic et al., 2008)), and γ is the surface energy density ($= 0.72 \text{ J/m}^2$ for water, 1.0 J/m^2 for glass, and $\geq 2 \text{ J/m}^2$ for polymers; bulk cilium is modeled as a water-like polymer). Other parameters are: equilibrium spacing of the cross-bridge $= 10 \text{ nm}$, and the radius of the actin filament $= 5.5 \text{ nm}$ (Cordova et al., 1992). Assume the value of a to be $(5.5\pi) \text{ nm}$ (hemispherical arc length), $E (= 0.50 \text{ GPa})$ of human tendon (Lauder et al., 2011) to be applicable, (A , the hemispherical area $2\pi(5.5 \text{ nm})^2$; and note that $1 \text{ J} = 1 \text{ Nm}$; $1 \text{ Pa} = 1 \text{ N/m}^2$; $\text{G} = 10^9$; $\text{n} = 10^{-9}$; $\text{p} = 10^{-12}$; $\text{y} = 10^{-24}$, then fracture stress (σ_f) would be

$$\begin{aligned} \sigma_f &= \sqrt{\frac{2(0.5 \times 10^9)}{\pi^2 5.5 \times 10^{-9}}} \\ &= \sqrt{2 \times 10^{16}} \\ &= 1.36 \times 10^8 \text{ N/m}^2. \end{aligned}$$

The force F required to fracture one of the foot anchors of the cross-bridge $= 2.6 \times 10^{-8} \text{ N} = 26 \text{ nN} = 26 \times 10^3 \text{ pN}$.

Earth's gravity exerts a force of 10 – 100 pN on cells in bio-physical systems. In their artificial gravity experiments with paramecia, Guevorkian and Vales (2006) show that they respond to gravity and regulate swim speed primarily due to the buoyancy of the cell. In their thermal cum electrostatic modeling of the motion of a single motor protein (myosin) molecule, Cordova et al. (1992) assume a maximum cross-bridge force of 5 pN. So, a cross-bridge detachment force of 26×10^3 pN is too high, and 5 pN is more reasonable.

On the other hand, Cordova et al. (1992) state that (1) the attachment and detachment sites of the cross-bridge differ by the presence of ATP when detached; and that (2) the “binding of ATP weakens the attachment of the cross-bridge to the fiber.” (ATP (adenosine-tri-phosphate) transports chemical energy within cells for metabolism; it is recycled; it is also a messenger molecule; it is sometimes called “the molecular unit of currency.”)

In linear elastic fracture mechanics, Griffith's theory (equations (5) and (6)) states that free energy is given by the difference between the surface energy and the elastic energy, and increases with the crack length. Failure occurs when the free energy attains a maximum value at a critical crack length beyond which the free energy decreases by increasing the crack length. The free energy in Griffith's theory may be corrected due to the hydrolysis of ATP at the detachment site when the chemical energy is released. One can back-calculate what this should be as follows:

The force F that leads the cross-bridge to detach = $[A, \text{the hemispherical attachment area} \times \sigma_f]$
 $= 2\pi(5.5 \times 10^{-9})^2 \sigma_f (\text{N}) = 190 \times 10^{-18} \sigma_f (\text{N})$. For this force F to be 5 pN, $\sigma_f = 5 \times 10^{-12} / (1.876 \times 10^{-15}) = 2.665 \times 10^3 \text{ N/m}^2 = 2.665 \text{ kPa}$. Assuming as before $E = 0.5 \times 10^9 \text{ N/m}^2$, the surface energy density γ would have to be $(1 \text{ J} = 1 \text{ Nm}) 3.856 \times 10^{-10} \text{ J/m}^2 = 38.56 \text{ nJ/m}^2$.

The ATP hydrolysis has to convert the chemical energy at the detachment site to make the surface energy density to be 38.56 nJ/m^2 for the force F required (produced practically at a point) to detach the cross-bridge to be 5 pN. The total energy (= surface energy – strain energy = $2\gamma L - \sigma_f^2 \pi a^2 L / (2E) = \gamma L$, where L is the third dimension of crack, and strain energy is the elastic energy released in the fracture area due to the fracture; the strain energy comes from the torsion) spent per detachment is $75 \times 10^{-24} \text{ J} = 75 \text{ yJ}$ (yocto joules).

Attributing the total energy to the chemical energy, the chemical energy spent is estimated as follows:

One mol has 6.02×10^{23} molecules; the energy released per ATP mol is 45.6 kJ. Therefore, the energy released per molecule of ATP is $76 \times 10^3 \text{ yJ}$, which can power 1000 cross-bridge detachments. For 3000 cilia in one paramecium, 3 ATP molecules are needed per beat cycle to detach one cross-bridge in each cilium; so, at 14 Hz, 42 ATP molecules are needed per second (fewer are needed if the absolute viscosity drops).

A full modeling of the ATP hydrolysis process is needed to quantitatively complete the evaluation of the mechanism. The hardness control model should include the mechanisms of softening at the detachment point due to the presence of ATP, subsequent enhanced bonding due to ATP hydrolysis, the effect of torsion, and sliding between the microtubules.

5. DISCUSSION

5.1 DEVELOPMENT OF THREE-DIMENSIONAL DEFORMATION IN CILIUM AND THE ROLE OF CRITICAL HARDNESS

The role of the modulus of torsional rigidity in the generation of torsion (= three-dimensionality) in the cilium was investigated experimentally and is presented in section A.5 of the appendix. Three-dimensionality can lead to stability of cruising and facilitation of food gathering. The paramecium cruises in a stable corkscrew path about an imaginary axis while rotating about its own body's axis. Compared to two-dimensional motion, the three-dimensional motion of the cilium imparts more momentum to the water and allows the thrust vector to be slanted to the plane of the power stroke (figure 7). In three-dimensional motion, all phases of the motion contribute to the production of an inward acceleration of the tiny tornadoes. These tornadoes (or their agglomerations) could allow the food elements to be drawn in as well.

Section A.5 of the appendix shows the curvature and torsion in several models of long cilia made of materials of different hardness but operated by the same type of actuator, consisting of three doublets (pairs of push-pull strings) spaced 120° apart. The hardness varied from near zero to a Shore hardness of A53-63. When hardness was very low, a helix was produced (a helix has a constant curvature and torsion). In contrast, in the high-hardness samples, only planar curvature was produced and torsion was zero (there was no off-plane curvature). The conclusion was that Shore hardness should be below a certain critical value for torsion to be manifested. *At the critical value of hardness, the cilium would be sensitive to any attempt at reduction or increase in hardness.* The detachment of only one cross-bridge in the biological cilium right after TS 14 at a strategic location on the cilium (location P), and the attachment of a new one at the same location P in the following phases would seem to allow control of the hardness at a critical level for low cost (a behavior akin to a high quality factor in resonant systems).

5.2 BIO-PHYSICAL SELF-REGULATION OF CILIUM HARDNESS

The dynamic systems analysis, the modeling of hardness control, and the preceding discussion on the value of designing a cilium of critical hardness point to the existence of the phase of neutral equilibrium and minimal energy expenditure. The authors deem this to be self-regulation.

It is known that when a paramecium hits an obstacle, it backs away at an angle and proceeds in a new direction (dePeyer and Machemer, 1978). The collision with the obstacle can be modeled via the amplitude and duration of the extra-cellular impulse term I_{ext} in equation (1). The cilium motion follows a limit cycle. The return path to the limit cycle is unique for a given value of I_{ext} and the phase of the system when I_{ext} is applied.

The 3000 cilia in a paramecium are each a nonlinear oscillator. The self-referential phase reset (SPR) property of equation (1) allows for synchronization between actuators that receive the extracellular impulse (Kazantsev et al., 2003 and 2004; and Bandyopadhyay et al., 2008). So far, the evidence for this process is conflicting.

Yeh et al. (1990) have observed spectral peaks at 370 kHz (attributed to the myosin thick filament) and a relaxation time of 5 μ s (attributed to cross-bridge motion). To straighten the cilium during the return stroke, the paramecium fuel cell needs to provide energy. The power stroke makes use of this energy. At the resonant frequency, maximum current flows through R in an RLC circuit. If C is 10 nF and L is 10 nH, the resonance frequency ($f_o = (1/(2\pi)) * [1/\sqrt{LC}]$) is 16 MHz. This is $\times 10^6$ of 14 Hz, the beat frequency of the cilium in water at 20° C. If more cross-bridges link the microtubule pair increasing C and L to 10 μ F, and 10 μ H, respectively, the resonant frequency would be 16 kHz, which is $\times 10^3$ of 14 Hz—a value much closer to that observed by Yeh et al. Parametric oscillators with second-order nonlinear interactions can produce lower frequencies from two higher frequencies by differencing their frequencies; however, there is no known evidence that this is happening.

If ϕ is torsional angle, the equation of torsional motion, as per a spring-mass-damper model is

$$I\ddot{\phi} + 2\zeta\omega_o\dot{\phi} + ({}^{\tau}k)\phi = 0,$$

where $f_o = \frac{1}{2\pi}\sqrt{\frac{{}^{\tau}k}{I}}$ is the natural frequency of torsional oscillation of the system ($\omega_o = 2\pi f_o$),

and $\zeta = \frac{{}^{\tau}c}{2\sqrt{({}^{\tau}k)I}}$ is the damping ratio, ${}^{\tau}c$ is the torsional damping (apart from viscous damping,

there may be structural damping also, which is hysteretic), ${}^{\tau}k$ is the torsional spring constant, (applied torque (${}^{\tau}k\phi$) + damping torque (${}^{\tau}c\dot{\phi}$) is the total torque), and I is the moment of inertia.

The description of a novel hemispherical motor (“frictionless”) cilium actuator is given in section A.4 of the appendix. The present authors have successfully operated the IOOMs of the robotic cilium with the real-time analog solution of equation (1), as described in Bandyopadhyay et al. (2008). This integrated operation of the controller and the actuator is discussed in section A.6 of the appendix. These two developments take us one step closer to fuller robotic simulation of cilium motion.

5.3 RELATIONSHIP WITH LARGER SCALE NATURAL SWIMMING: A SYNTHETIC VIEW

As per Llinas (2001), Llinas and Yarom (1981), and Llinas et al. (2004):

1. Motion control neurons follow self-regulating, dynamic systems principles.
2. The neurons can be clustered together on demand (self-referential phase reset (SPR) property (Kazantsev et al., 2004).
3. Neuronal development in animals parallels that of biomechanics, the former being mature in motion control over many species and remaining unchanged.

Extending these principles further, if sensors, actuators, and their control follow the same dynamic systems principles to remain in persistent synchrony with the environment, then they home faster on moving targets if they are assumed to have a 10-15% stereoscopic bias in sensing and actuation (Bandyopadhyay, 2012a).

A flapping fin is lift based and it flaps cross stream to the thrust. On the other hand, a cilium is drag based and it flaps both in the plane of thrust and in the transverse plane. How does the transition from small to large and from drag-based to lift-based propulsion take place?

Ellington (1999) has considered the wing flapping in insects to be a resonant oscillation that has low friction and high amplitude. Triantafyllou and Triantafyllou (1995) have shown that varieties of fish flap their caudal fins in a range of preferred frequency called the Strouhal number (0.2 to 0.4). Note that the length scale in Strouhal number is given by the amplitude of oscillation, which can be expected to reach a large value in resonant oscillation. In recent work, the present authors have been able to operate penguin-wing-like flapping fins in large scale for ocean engineering purposes while flapping at the above range of Strouhal number (Bandyopadhyay et al., 2011).

Paramecia have pressure-sensitive mechanoreceptors (dePeyer and Machemer, 1978 and 1983), sliding microtubules that produce curvature in cilia, phased beating of cilia along their body surface that produce the animal's tumbling motion in a corkscrew path, and a 9+2 axoneme architecture. Fish have pressure-sensitive lateral lines, hemitrich bone pairs in their pectoral fins for producing curved shapes (Lauder et al., 2011), central pattern generators for producing tail beat, and 11 hemitrich bones on their pectoral fin spaced with a common origin (Lauder and Drucker, 2004). These similarities were assumed to owe their origin to co-evolution of sensors, actuators, and control, and a common oscillatory framework of a dynamic system. In section A.7 of the appendix (see Bandyopadhyay, 2009), the outline of a notional synthetic description vividly shows the common lineage of large and small swimming animals.

Each of the tiny individual cilium propulsors appears to have the intrinsic, dormant kinematic and structural building blocks required to optimize at both low and high Reynolds numbers. The tentative conclusion is that the integrated autonomous sensory, actuating, and controlling architecture of the paramecium is invariant of Reynolds number.

6. CONCLUSIONS

Modeling and analysis of the motion of the paramecium's cilium have been carried out, with a focus on the motion's oscillatory nature. Theoretical modeling included considerations of a torsional pendulum, dynamic systems, and fracture mechanics. A revised analysis of Teunis and Machemer's (1994) photo-microscopy of biological cilium has been compared with a robotic simulation of the biological cilium. The role of torsional rigidity in three-dimensional deformation has been examined. The aspects of integrating sensors, controller, and actuators that remain invariant with Reynolds number have been robotically simulated and discussed.

The following conclusions can be drawn:

1. The variation of the cilium beat frequency with fluid viscosity can be modeled by describing the beat frequency as the natural frequency of a torsional pendulum.
2. The cilium track is a limit cycle describable by dynamic systems theory. There exists a phase of neutral equilibrium lying at the boundary where the power stroke changes to the return stroke and the cilium velocity is zero.
3. Several long, mechanical cilia have been fabricated, and it was found that their hardness has to be below a certain level for torsion to be manifested.
4. The three-dimensional motion of each cilium produces a tiny tornado of fluid having an inward acceleration. The inward acceleration is produced during both the power and return strokes.
5. The local angle that the cilium orbital velocity and the cilium position makes with the propulsion axis remain nearly constant, along the length of the cilium during the power stroke, but it varies widely during the return stroke.
6. The average radial length of the cilium in the transverse plane remains large during the first two-thirds of the power stroke, dropping precipitously during the remaining one-third. The average cilium radial length increases during the return stroke. This variation of the average radial length should help increase thrust during the power stroke and lower drag during the return stroke.
7. The zero crossings of the product of the average radial length of the cilium in the transverse plane and of the cilium velocity are used to define the extents of the power and return strokes. The power stroke is 0.50 of the beat period, which is larger than the 0.14 to 0.28 range given by Teunis and Machemer (1994).
8. Using four independent orthogonal oscillatory motor drives, a robotic cilium has been constructed whose curvature and torsion distributions are in fair agreement with those of the biological cilium. The robotic cilium has also been controlled by analog olivo-cerebellar dynamics.

9. A bio-physical model of self-regulation of cilium hardness is given where cross-bridge links between the microtubule pairs, ATP molecules, and torsion play a key role in hardness control. Fracture mechanics has been applied to the cross-bridge detachment at the phase of neutral equilibrium at the cilium location where a point of inflection is created. Synthesis of the results suggests that the cilium is torsionally wound (like a spring) during the return stroke and the energy is expended during the power stroke.

10. The similarities in the sensory, actuating, and control architecture of paramecia and fish are noted.

7. FUTURE WORK

Future work should be carried out in the following areas:

1. Polymer Nano-Micrometer Scale Mechanical Cilium: Such a cilium can be fabricated as follows. It is known that when solvated polymer is ejected through a positively charged conducting syringe by a pump, the laminar jet flow, when allowed to dry, forms a cylindrical fiber. The instability of such jets is considered by Rallison et al. (1995), Hohman et al. (2001), and Shin et al. (2001). From a wide range of polymeric materials, such an electrospinning technique can be used to make cylindrical nanofibers of length $17\text{ }\mu\text{m}$ with a diameter of less than $1\text{ }\mu\text{m}$ (see Lu et al. (2009), Burger et al. (2006), Shin et al. (2001), Reneker and Chun (1996), Reneker et al. (2007), Ramaswamy et al. (2011), Ojha et al. (2008), and McCullen et al. (2007)). Such cilia would have the Reynolds number of the biological cilium. The mechanical rendition consists of a pair of such electrospun polymer fibers, closely spaced but attached at the distal point. The base of the assembly is mounted on a pair of stacked MEMS (micro-electro-mechanical systems) tables. The table assembly is oscillated orthogonally as in figure 11. The pair of nanofibers is given a push-pull oscillation to generate bending. Using another MEMS table underneath the stacked pair, the entire assembly described above is given a twisting oscillation as in figure 11 (Bandyopadhyay, 20012b).

2. “Frictionless Actuation” with a Hemispherical Motor Drive: Using programmable logic circuits and the 0.21-m-long robotic cilium (or the polymer nano-cilium) base torque actuation with the hemispherical motor drive can be explored. Such a gearless, noncontact drive can be expected to be nearly frictionless. This would simulate the condition of resonant oscillation.

3. Disturbance Rejection Verification: Further verification of the limit cycle nature of the cilium trajectory can be made using the hemispherical motor. Disturbances can be applied to the cilium to see the trajectory it takes to return to the LCO. The return paths can be compared with the theoretical trajectories. This experiment would verify the autonomic nature of cilium swimming.

4. Three-Dimensional Hydrodynamic Modeling: Such modeling would bring us one step closer to exploring three-dimensional metachronism.

5. Origin of Metachronism: Application of dynamic systems theory is a new approach to the understanding of cilium autonomy. A parallel exploration of metachronism due to hydrodynamic coupling of neighboring cilia and that due to term I_{ext} in equation (1) could be carried out.

6. Modeling Torsional Effects: The effect of torsion on the cross-bridge linking between microtubules could be theoretically modeled to understand how hardness can be varied to store and release mechanical energy in a torsional oscillatory system with minimal energy expenditure.

8. BIBLIOGRAPHY

- Adamovic, I., S. M. Mijailovich, and M. Karplus (2008), "The Elastic Properties of the Structurally Characterized Myosin II S2 Subdomain: A Molecular Dynamics and Normal Mode Analysis," *Biophysics Journal*, vol. 94, pp. 3779-3789.
- Au, W. (1993), *The Sonar of Dolphins*, Springer-Verlag, New York.
- Bandyopadhyay, P. R. (2012a), "Handedness Helps Homing: Smart Materials, Structures and Systems," CIMTEC 2012, June 10-14, 2012, Montecatini Terme, Italy.
- Bandyopadhyay, P. R. (2012b), "A Nano-Micrometer Scale Mechanical Cilium for Dynamic Transduction," Invention Disclosure, Navy Case (to be submitted), Naval Undersea Warfare Center Division, Newport, RI.
- Bandyopadhyay, P. R. (2011), "An Acousto-Optical Method of Encoding and Visualization of Underwater Space," Invention Disclosure, Navy Case Number 101454, submitted November 2011 (patent pending).
- Bandyopadhyay, P. R. (2009), "Origin of Propulsion: A Synthetic View," DVD (edited with audio), Naval Undersea Warfare Center Division, Newport, RI 02841.
- Bandyopadhyay, P. R. (2005), "Trends in Biorobotic Autonomous Undersea Vehicles," *IEEE Journal of Oceanic Engineering*, vol. 30, no. 1, pp. 109-139.
- Bandyopadhyay, P. R. (2004), "Biology-Inspired Science and Technology for Autonomous Underwater Vehicles," *IEEE Journal of Oceanic Engineering*, vol. 29, no. 3, pp. 542-806.
- Bandyopadhyay, P. R., H. A. Leinhos, J. D. Hrubes, N. Toplosky, and J. Hansen (2011), "Turning of a Short Length Cable Using Flapping Fin Propulsion," *IEEE Journal of Oceanic Engineering*, vol. 36, pp. 571-585.
- Bandyopadhyay, P. R., S. N. Singh, D. P. Thivierge, A. M. Annaswamy, H. A. Leinhos, A. R. Fredette, and D. N. Beal (2008), "Synchronization of Animal-Inspired Multiple Fins in an Underwater Vehicle Using Olivo-Cerebellar Dynamics," *IEEE Journal of Oceanic Engineering*, vol. 33, no. 4, pp. 563-578.
- Blake, J. R. (1971) "A Spherical Envelope Approach to Ciliary Propulsion," *Journal of Fluid Mechanics*, vol. 46, part 1, pp. 199-208.
- Bouzarth, E. L., A. Brooks, R. Camassa, H. Jing, T. J. Leiterman, R. M. McLaughlin, R. Superfine, J. Toledo, and L. Vicci (2007), "Epicyclic Orbits in a Viscous Fluid About a Precessing Rod: Theory and Experiments at the Micro- and Macro-Scales," *Physical Review E Statistical, Nonlinear, and Soft Matter Physics*, vol. 76 (part 1 of 2), 016313.

- Brokaw, C. J. (1966), "Bend Propagation Along Flagella," *Nature (London)*, vol. 209, p. 161.
- Burger, C., B. S. Hsiao, and B. Chu (2006), "Nanofibrous Materials and Their Applications," *Annual Review of Materials Research*, vol. 36, pp. 333-368.
- Cordova, N. J., B. Ermentrout, and G. F. Oster (1992), "Dynamics of Single-Motor Molecules: The Thermal Ratchet Model," *Proceedings of the National Academy of Sciences, Biophysics*, vol. 89, pp. 339-343.
- Dean, P., J. Porril, C-F. Ekerot, and H. Jornteli (2010), "The Cerebellar Microcircuit as an Adaptive Filter: Experimental and Computational Evidence," *Nature Reviews: Neuroscience*, vol. 11, pp. 30-43.
- Deitmer, J. W., H. Machemer, and B. Martinac (1984), "Motor Control in Three Types of Ciliary Organelles in the Ciliate Stylonychia," *Journal of Comparative Physiology A*, vol. 154, pp. 113-120.
- dePeyer, J., and H. Machemer (1978), "Are Receptor-Activated Ciliary Motor Responses Mediated Through Voltage or Current?" *Nature*, vol. 276, pp. 285-287.
- dePeyer, J. E., and H. Machemer (1983), "Threshold Activation and Dynamic Response Range of Cilia Following Low Rates of Membrane Polarization Under Voltage-Clamp," *Journal of Comparative Physiology*, vol. 150, pp. 223-232.
- Dillon, R. H., and L. J. Fauci (2000), "An Integrative Model of Internal Axoneme Mechanics and External Fluid Dynamics in Ciliary Beating," *Journal of Theoretical Biology*, vol. 207, pp. 415-430.
- Dute, R., and C. Kung (1978), "Ultrastructure of the Proximal Region of Somatic Cilia in Paramecium Tetraurelia," *Journal of Cell Biology*, vol. 78, pp. 451-464.
- Ellington, C. P. (1999), "The Novel Aerodynamics of Insect Flight: Applications to Micro-Air Vehicles," *Journal of Experimental Biology*, vol. 202, pp. 3439-3448.
- Griffith, A. A. (1920), "The Phenomena of Rupture and Flow in Solids," *Philosophical Transactions of the Royal Society*, vol. A221, pp. 163-198.
- Gueron, S., and K. Levit-Gurevich (2001), "A Three-Dimensional Model for Ciliary Motion Based on the Internal 9 + 2 Structure," *Proceedings of the Royal Society of London B*, vol. 268, pp. 599-607.
- Gueron, S., and K. Levit-Guerevich (1999a), "Energetic Considerations of Ciliary Beating and the Advantage of Metachronal Coordination," *Proceedings of the National Academy of Sciences*, vol. 96, no. 22, pp. 12240-12245.

- Gueron, S., and K. Levit-Guerevich (1999b), "A Three-Dimensional Model of Ciliary Motion Based on Internal 9+2 Structure," *Proceedings of the Royal Society*, vol. 96, no. 22, pp. 12240-12245.
- Gueron, S., K. Levit-Gurevich, N. Liron, and J. J. Blum (1997), "Cilia Internal Mechanism and Metachronal Coordination as the Result of Hydrodynamical Coupling," *Proceedings of the National Academy of Sciences, Applied Mathematics*, vol. 94, pp. 6001-6006.
- Gueron, S., and N. Liron (1992), "Ciliary Motion Modeling, and Dynamic Multicilia Interactions," *Biophysics Journal*, vol. 63, pp. 1045-1058.
- Guevorkian, K., and J. M. Valles (2006), "Swimming Paramecium in Magnetically Simulated Enhanced, Reduced, and Inverted Gravity Environments," *Proceedings of the National Academy of Sciences*, vol. 103, no. 35, pp. 13051-13056.
- Guirao, B. (and fifteen others) (2010), "Coupling Between Hydrodynamic Forces and Planar Cell Polarity Orients Mammalian Motile Cilia," *Nature Cell Biology*, vol. 12, pp. 341-350.
- Gittes, F., B. Mickey, J. Nettleton, and J. Howard (1993), "Flexural Rigidity of Microtubules and Actin Filaments from Thermal Fluctuations in Shape," *Journal of Cell Biology*, vol. 120, no. 4, pp. 923-934.
- Hines, M., and J. J. Blum (1978), "Bend Propagation in Flagella, I. Derivation of Equations of Motion and Their Simulation," *Biophysics Journal*, vol. 23, pp. 41-57.
- Hines, M., and J. J. Blum (1983), "Three-Dimensional Mechanics of Eukaryotic Flagella," *Biophysics Journal*, vol. 41, pp. 67-79.
- Hohman, M. M., M. Shin, G. Rutledge, and M. P. Brenner (2001), "Electrospinning and Electrically Forced Jets, II. Applications," *Physics of Fluids*, vol. 13, no. 8, pp. 2221-2236.
- Irwin, G. R. (1948), "Fracture Dynamics," in *Fracturing of Metals*, American Society for Metals, Cleveland, OH, pp. 147-166.
- Jaffe, L. F. (2007), "Models and Speculations Stretch-Activated Calcium Channels Relay Fast Calcium Waves Propagated by Calcium-Induced Calcium Influx," *Biological Cell*, vol. 99, pp. 175-184 (printed in Great Britain, doi:10.1042/BC20060031 Scientiae forum).
- Karp G. (2005), *Cell and Molecular Biology: Concepts and Experiments*, Fourth Edition, John Wiley and Sons, Hoboken, NJ, pp. 346-358.
- Kazantsev, V. B., V. Nekorkin, V. Makarenko, and R. Llinas (2003), "Olivary-Cerebellar Cluster-Based Universal Control System," *Proceedings of the National Academy of Sciences*, vol. 100, no. 22, pp. 13064-13068.

- Kazantsev, V. B., V. Nekorkin, V. Makarenko, and R. Llinas (2004), "Self-Referential Phase Reset Based on Inferior Olive Oscillator Dynamics, *Proceedings of the National Academy of Sciences*, vol. 101, pp. 18183-18188.
- Khalil, H. K. (1996), *Nonlinear Systems*, Prentice-Hall, Upper-Saddle River, NJ.
- Kongthon, J., B. McKay, D. Iamratanakul, K. Oh, J.-H. Chung, J. Riley, and S. Devasia (2010), "Added-Mass Effect in Modeling of Cilia-Based Devices for Microfluidic Systems," *ASME Journal of Vibration and Acoustics*, vol. 132, 024501-1.
- Lauder, G.V. (2009), Private Communication with P. Bandyopadhyay, Naval Undersea Warfare Center Division, Newport, RI.
- Lauder, G. V., and E. G. Drucker (2004), "Morphology and Experimental Hydrodynamics of Fish Fin Control Surfaces," *IEEE Journal of Oceanic Engineering*, vol. 29, pp. 556-571.
- Lauder, G. V., P. G. A. Madden, J. L. Tangora, E. Anderson, and T. V. Baker (2011), "Bioinspiration from Fish for Smart Material Design and Function," *Smart Materials and Structures*, vol. 20, 094014.
- Li, F., and X. Yin (2009), "Axisymmetric and Non-Axisymmetric Instability of an Electrified Viscous Coaxial Jet," *Journal of Fluid Mechanics*, vol. 632, pp. 199-225.
- Llinas, R. R. (2009), "Inferior Olive Oscillation as the Temporal Basis for Motricity and Oscillatory Reset as the Basis for Motor Error Correction," *Neuroscience*, vol. 162, no. 3, pp. 797-804.
- Llinas, R. R. (2001), *I of the Vortex from Neurons to Self*, MIT Press, Cambridge, MA.
- Llinas, R. R., E. Leznik, and V. I. Makarenko (2004), "The Olivo-Cerebellar Circuit as a Universal Control System," *IEEE Journal of Oceanic Engineering*, vol. 29, pp. 631-639.
- Llinas, R. R., and Y. Yarom (1981), "Electrophysiology of Mammalian Inferior-Olive Neurons in Vitro, Different Types of Voltage Dependences in Conductances," *Journal of Physics (London)*, vol. 315, pp. 549-567.
- Lu, X. F., C. Wang, and Y. Wei (2009), "One-Dimensional Composite Nanomaterials: Synthesis by Electrospinning and Their Applications, *Small*, vol. 5, pp. 2349-2370.
- Machemer, H. (1972), "Ciliary Activity and the Origin of Metachrony in Paramecium: Effects of Increased Viscosity," *Journal of Experimental Biology*, vol. 57, pp. 239-259.
- Machemer, H., and A. Ogura (1979), "Ionic Conductances of Membranes in Ciliated and Deciliated Paramecium," *Journal of Physiology*, vol. 296, pp. 49-60.

- Machemer, H., and S. Machemer-Rehnisch (1984), "Mechanical and Electric Correlates of Mechanoreceptor Activation of the Ciliated Tail in Paramecium," *Journal of Sensory and Comparative Physiology A*, vol. 154, pp. 273-278.
- McCullen, S. D., K. L. Stano, D. R. Stevens, W. A. Roberts, N. Monteiro-Riviere, L. I. Clarke, and R. E. Gorga (2007), "Development, Optimization, and Characterization of Electrospun Poly(Lactic Acid) Nanofibers Containing Multi-Walled Carbon Nanotubes," *Journal of Applied Polymeric Science*, vol. 105, pp. 1668-1678.
- Nakaoka, Y., H. Tanaka, and F. Oosawa (1984), " Ca^{2+} -Dependent Regulation of Beat Frequency of Cilia in Paramecium," *Journal of Cell Science*, vol. 65, pp. 223-231.
- Ojha, S.S., D. R. Stevens, K. Stano, T. Hoffman, W. E. Krause, L. I. Clarke, and R. E. Gorga (2008), "Characterization of Electrical and Mechanical Properties for Coaxial Nanofibers with Poly-Ethylene Oxide (PEO) Core and Multiwalled Carbon Nanotube/PEO Sheath," *Macromolecules*, vol. 41, pp. 2509-2513.
- Omoto, C. K., and C. Kung (1980), "Rotation and Twist of the Central-Pair Microtubules in the Cilia of Paramecium," *Journal of Cell Biology*, vol. 87, pp. 33-46.
- Pernberg, J., and H. Machemer (1995), "Voltage-Dependence of Ciliary Activity in the Ciliate Didinium Nasutum," *Journal of Experimental Biology*, vol. 198, pp. 2537-2545.
- Rallison, J. M., and E. J. Hinch (1995), "Instability of a High-Speed Submerged Elastic Jet," *Journal of Fluid Mechanics*, vol. 288, pp. 311-324.
- Ramaswamy, S., L. I. Clarke, and R. E. Gorga (2011), "Morphological, Mechanical, and Electrical Properties as a Function of Thermal Bonding in Electrospun Nanocomposites," *Polymer*, vol. 52, pp. 3183-3189.
- Ramia, M., D. L. Tullock, and N. Phan-Thien (1993), "The Role of Hydrodynamic Interaction in the Locomotion of Microorganisms," *Biophysical Journal*, vol. 65, pp. 755-778.
- Reneker, D. H., and I. Chun (1996), "Nanometre Diameter Fibres of Polymer Produced by Electrospinning," *Nanotechnology*, vol. 7, pp. 216-223.
- Reneker, D. H., A. L. Yarin, E. Zussman, and H. Xu (2007), "Electrospinning of Nanofibers from Polymer Solutions and Melts," *Advances in Applied Mechanics*, vol. 41, pp. 43-195.
- Shin, Y. M., M. M. Hohman, M. P. Brenner, and G. C. Rutledge (2001), "Electrospinning: A Whipping Fluid Jet Generates Submicron Polymer Fibers," *Applied Physics Letters*, vol. 78, pp. 1149-1151.
- Shields, A. R., B. L. Fiser, B. A. Evans, M. R. Falvo, S. Washburn, and R. Superfine (2010), "Biomimetic Cilia Arrays Generate Simultaneous Pumping and Mixing Regimes," *Proceedings of the National Academy of Sciences*, vol. 107, no. 36, pp. 15670-15675.

- Slotine, J.-J. E., and W. Li (1991), *Applied Nonlinear Control*, Prentice-Hall, Englewood Cliffs, NJ, pp. 160-163.
- Tamm, S. L. (1984), "Mechanical Synchronization of Ciliary Beating within Comb Plates of Tenophores," *Journal of Experimental Biology*, vol. 113, pp. 401-408.
- Tamm, S. L., and S. Tamm (1989), "Calcium Sensitivity Extends the Length of ATP-Reactivated Ciliary Axonemes," *Proceedings of the National Academy of Sciences, Cell Biology*, vol. 86, pp. 6987-6991.
- Teunis, P. M. F., and H. Machemer (1994), "Analysis of Three-Dimensional Ciliary Beating by Means of High-Speed Stereomicroscopy," *Biophysical Journal*, vol. 67, pp. 381-394.
- Triantafyllou, M. S., and G. S. Triantafyllou (1995), "An Efficient Swimming Machine," *Scientific American*, vol. 272, no. 3, pp. 64-70.
- Yeh, Y., R. J. Baskin, S. Shen, and M. Jones (1990), "Photon Correlation Spectroscopy of the Polarization Signal of Single Muscle Fibers," *Journal of Muscle Research and Cell Motility*, vol. 11, no. 2, pp. 137-146.
- Wakeling, J. M., and C. P. Ellington (1997), "Dragonfly Flight, III. Lift and Power Requirements," *Journal of Experimental Biology*, vol. 200, pp. 583-600.
- Wurzel, S. E. (2003), "Prospects for Studying Negative Gravitaxis in Paramecium Using Magnetic Field Gradient Levitation," Senior Thesis, Brown University, Department of Physics, Providence, RI.
- Zwillinger, D. (1996), *Standard Mathematical Tables and Formulae*, CRC Press.

APPENDIX—SUPPLEMENTARY INFORMATION

A.1 TWO-DIMENSIONAL HYDRODYNAMIC MODELING

Note: This section is due to Norman Toplosky (Code 1532).

As a first step in modeling the dynamics of cilium motion, a two-dimensional dynamic model was constructed to develop familiarity with the solution technique. Following the biorobotic approach mentioned earlier, the authors made no direct effort at modeling the actual physiology of the cilium, but instead concentrated on driving the base of a mechanically-equivalent cilium with the same motion as observed in the data of Teunis and Machemer (1994), and then attempted to adjust the rigidity and drag parameters so as to reproduce the motion of the entire cilium. The two-dimensional model was considered to be an important first step and building block toward the eventual development of a full three-dimensional model. The latter model would be different from the former in two important ways; first, a third dimension would allow out-of-plane bending and torsion, and second, the three-dimensional model would possibly allow inclusion of torsional rigidity and a driving torque at the cilium base.

In the initial two-dimensional model, the cilium is modeled as N rigid links connected by nodal ball joints in which the cilium bending rigidity is lumped. The bending rigidity lumped at the nodes can vary both with time (depending on where one is in the power-recovery stroke cycle) and with length along the cilium. Fluid drag loads—due both to the mean advance of the cilium (velocities U , V) and to the rotational motion of the cilium about its base—act on each link and depend on both the orientation of the link (x , y , and z coordinates of the bracketing nodes) and the in-water velocity of the link (u , v , and w velocity components of the bracketing nodes). The bending moment in the nodal ball joints is proportional to the local curvature, estimated by the change in orientation of the two links joined at that node. Internal forces also act at each node. Figure A-1 shows this setup. Note that in the biological cilium and the robotic cilium, y represents the vertical direction and z represents the spanwise direction; but in the two-dimensional hydrodynamic simulation, z represents vertical direction.

The polar angle of the first link (the angle between the link and the vertical z -axis) and its rate (θ and $d\theta/dt$) are taken as kinematic boundary conditions at the base. Zero force and moment conditions are applied at the distal node of the last link.

The physics-based two-dimensional model using N links is well-posed: Not counting the origin (cilium base is node 0), there are N nodes and at each of these there are two position coordinates, two velocity components, and two force components, for a preliminary total of $6N$ unknowns (see table A-1). On each of the N links there are two force balances (in the x - and z -directions), one moment balance (in the y -direction), one geometric constraint ensuring that the link's bracketing nodal positions are a link length apart, and two kinematic relations relating the distal node's velocity components to the time derivatives of the position coordinates, for a

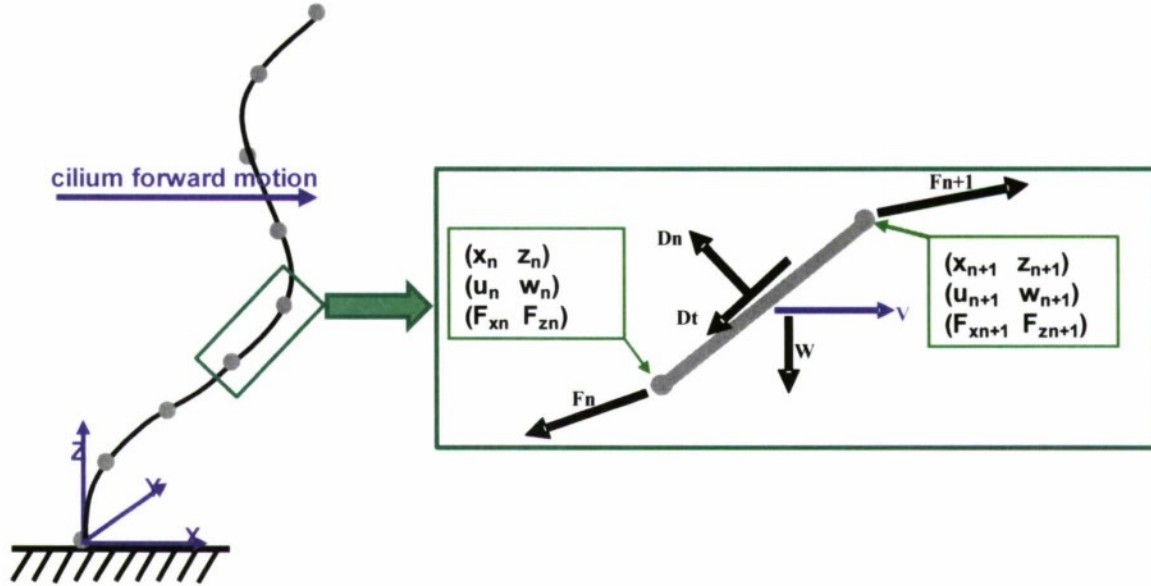


Figure A-1. Rigid Link Model of Cilium

preliminary total of $6N$ equations. However, this preliminary set of $6N$ equations in $6N$ unknowns is slightly modified by the additional constraints and unknowns at the base and distal node.

The resulting equations (see table A-1) were programmed in MATLAB. The base link was driven by a harmonic motion (the polar angle was sinusoidal). Cilium stiffness was increased during the power stroke and relaxed during the recovery stroke, and a mean speed-of-advance (as a fraction of the cilium tip speed midway through the power stroke) was added to the base motion. The profiles in figure A-2 were computed.

The development of the three-dimensional cilium model is still in progress. As mentioned earlier, there are two major changes when going from two dimensions to three. The first change is that all vectors have three components instead of two, and because bending is no longer confined to the y -direction, the cilium develops torsion as the bending direction (the unit bi-normal vector \hat{b}) changes direction. The second change is that one can include a driving base torque and resulting twist, if one wishes.

Table A-1 provides background information regarding the two-dimensional hydrodynamic modeling. This section also lists the Frenet equations, which describe the geometry of a curve in space; here, k is curvature, τ is torsion, \hat{t} and \hat{n} are unit tangent and normal vectors, \hat{b} is the unit bi-normal vector, and s is the axial length.

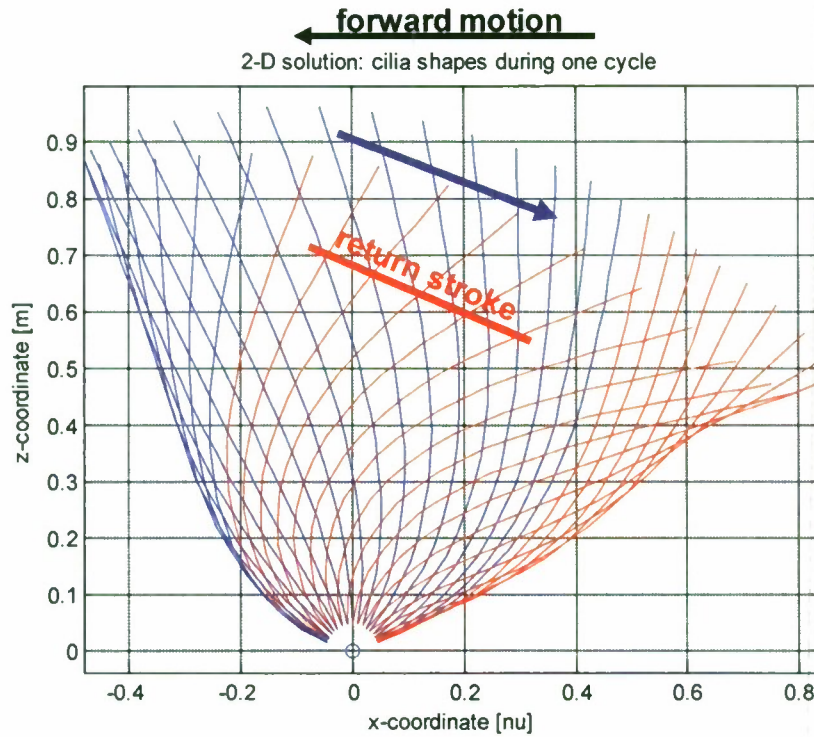


Figure A-2. Two-Dimensional Cilium Profiles (nu: normalized unit)

The integral of the base force over a beat cycle is the net impulse from that cycle. The asymmetric beating pattern and mean advance of the base allows for a non-zero thrust, even in two dimensions, as shown in figure A-3.

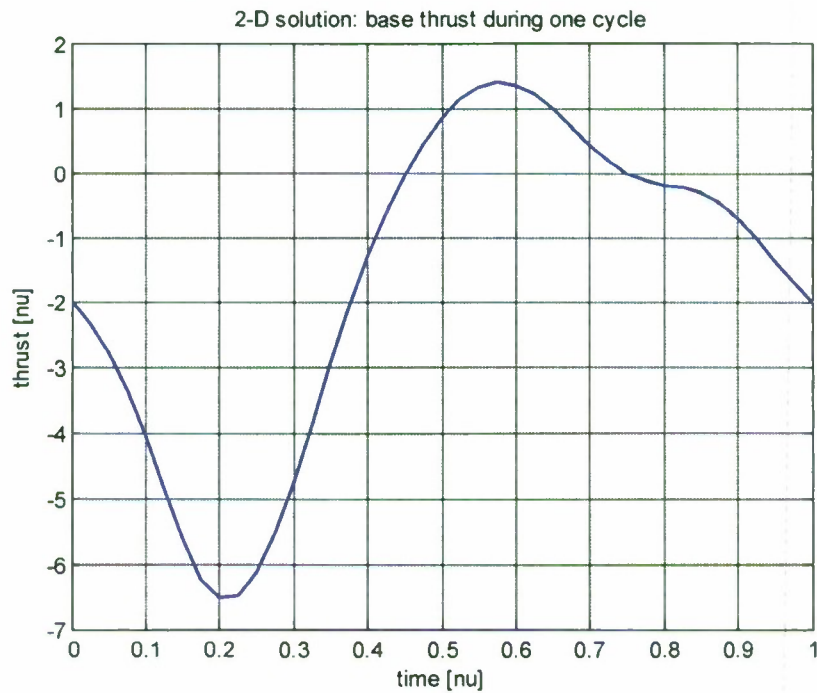


Figure A-3. Two-Dimensional Base Thrust (nu: normalized unit)

Table A-1. Hydrodynamic Modeling Background Information

	Unknowns	Equations
Node 0 (base)	F_x F_z M_y	
Node 1	x z u v F_x F_z	$x = L\sin\theta$ $z = L\cos\theta$ $u = L(d\theta/dt)\cos\theta$ $v = -L(d\theta/dt)\sin\theta$
Nodes 2... $N - 1$	x z u v F_x F_z	$U = dx/dt$ $V = dy/dt$
Node N (distal node)	x z u v	$U = dx/dt$ $V = dy/dt$
Link 1		F_x force balance F_y force balance M_y moment balance
Link 2... N		F_x force balance F_y force balance M_y moment balance Link-length constraint
Total:	$6N+1$	$6N+1$

Frenet Equations:

$$\frac{d\hat{t}}{ds} = +\kappa\hat{n}$$

$$\frac{d\hat{n}}{ds} = -\kappa\hat{t} + \tau\hat{b}$$

$$\frac{d\hat{b}}{ds} = -\tau\hat{n}$$

A.2 VALIDATION OF DIGITIZATION OF PUBLISHED BIOLOGICAL CILIAM DATA

A.2.1 Parametric Fits

The digitized biological cilium in pixels in the longitudinal plane is shown in figure A-4. The steps for obtaining the three-dimensional parametric fits and associated lengths are as follows:

1. Find the base of the top and side views and adjust the pixel values for a base of (0, 0).
2. Obtain the length in the orthogonal axis (from the alternate view) for the top and side projections (the y-value in the top view is z (width) and the y-value in the side view is y (height)):
 - a. for the side view, this is the top view vertical axis.
 - b. for the top view, this is the side view vertical axis.
3. Interpolate the orthogonal lengths (from above) to match the number of points from the alternate view. This is required since the top view and side view of a particular time step have a different number of points.
4. Calculate the lengths for each view by $\sqrt{(\Delta x^2 + \Delta y^2 + \Delta z^2)}$, where x and y are from the top and side planar views and z is the orthogonal axis differences from step 3. Note that inconsistent data between the two views result in the lengths for each view being different.
5. Obtain *two-dimensional parametric fits* for the top and side views using the lengths calculated above, with the length as the independent variable.
6. Choose the x, y, z values (to use in the three-dimensional parametric fit later) as follows:
 - a. x = top view x (could also choose side view x values).
 - b. y = side view y.
 - c. z = top view y.
7. Calculate the lengths as the cumulative sum of $\sqrt{(\Delta x^2 + \Delta y^2 + \Delta z^2)}$ for each time step. See figure 3a in the main text.
8. Use the parametric equations for both views to calculate an arbitrary, user-selected number of orbits for analysis.
9. Fit a *three-dimensional parametric equation* to the data for each orbit using the x, y, z values, with the step number as the independent variable.
10. Calculate the lengths as the cumulative sum of $\sqrt{(\Delta x^2 + \Delta y^2 + \Delta z^2)}$ for each time step, through each orbit. See figure 3c.

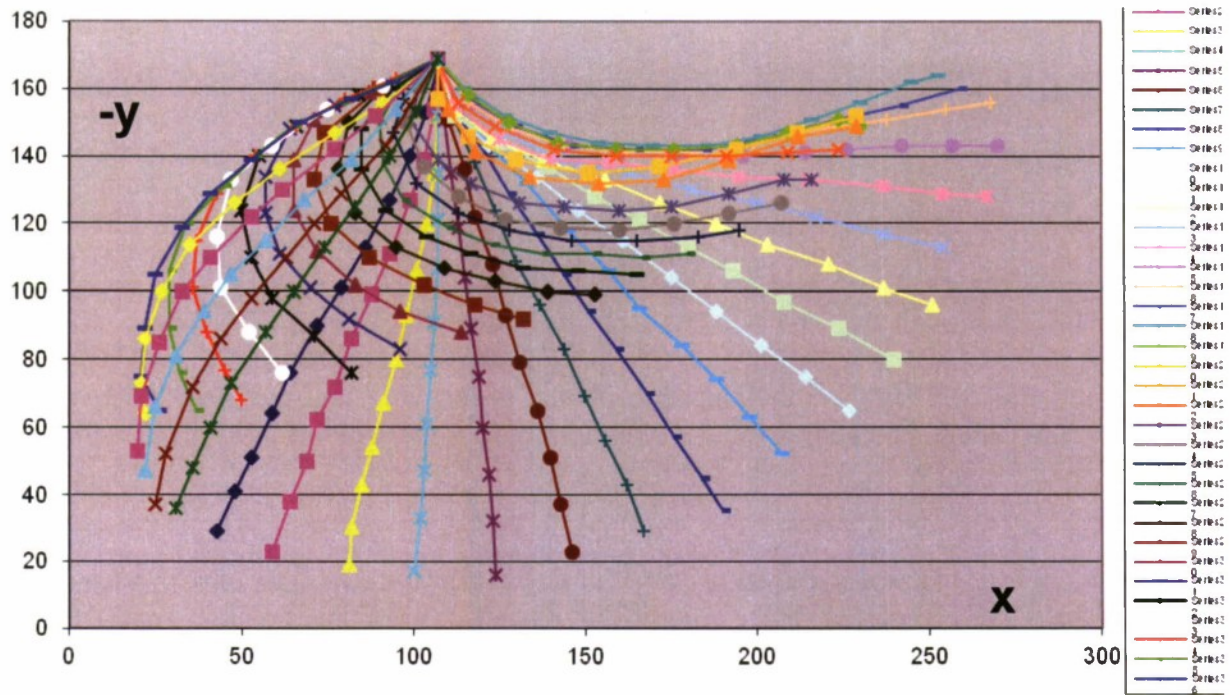


Figure A-4. Graph of Digitized Cilium Prior to Parametric Processing and Smoothing
(Each color is a different time step; length units are in pixels.)

A.2.2 Notes on Data Smoothing and Definitions

1. A length of 156 is the original pixel data (digitized biological data); a length of 17 μm is for the adjusted biological cilium; and a length of 0.21 m is for the robotic cilium.
2. The polynomial used along the length of the cilium is fourth order, although it is used only to calculate an equal number of points for each time step.
3. The polynomial for each orbit (concentric path) is 15th order.
4. Parametric equations are independent for x , y , z and are based only on length and themselves, i.e., $x = f(x, l)$, $y = f(y, l)$, $z = f(z, l)$, where l is the length of the cilium ($l = s$).

5. Smoothing is done with a five-point moving average to obtain the average cilium radius (curved length projected on the transverse plane y-z) at a given time instant:

$$R_{avg}(t) = \sqrt{\{l_{yz}(t)\}^2 / 2},$$

where $l_{yz}(t)$ is the curved length of the entire cilium in the y-z plane (transverse plane) (sum of the y- and z-components of each length segment of the cilium) at a given time instant; to clarify, R_{avg} is not a radial distance from the origin to the point on the cilium where R_{avg} lies.

6. The accuracy of the Teunis-Machemer data digitization and length calculation is as given in tables A-2 through A-4. The cilium length is divided into 20 segments and the lengths are measured from the base.

A.2.3 Accuracy of Parametric Fits and Smoothing

The accuracy of the parametric fits and smoothing is shown in tables A-2 through A-4. These tables show how the mean and rms distances (μm) of 20 points on the cilium counting vary. Table A-2 is for the entire beat cycle; tables A-3 and A-4 are for the power and return strokes, respectively. (In the column headings of these tables, “top”, “mid”, and “bot” refer to the top (a), middle (b), and bottom (c) frames in figure 3 in the main text.) Although the cilium is curved during the return stroke, the cilium lengths are close (within 4%) to those during the power stroke when the cilium is fairly straight. The data processing, therefore, is accurate.

Table A-2. Variation of RMS in Length Estimation in the Revisited TM Data (Entire Beat Cycle)

Mean and RMS Cilium Lengths (All Positions) (μm)					
Mean (top)	Mean (mid)	Mean (bot)	RMS (top)	RMS (mid)	RMS (bot)
0.1128	0.0875	0	0.1271	0.0940	0
1.0402	1.0026	0.9157	1.0465	1.0073	0.9193
1.9508	1.9021	1.8157	1.9573	1.9071	1.8199
2.8514	2.7915	2.7053	2.8572	2.7958	2.7091
3.7456	3.6739	3.5878	3.7504	3.6774	3.5909
4.6355	4.5513	4.4651	4.6395	4.5541	4.4676
5.5220	5.4249	5.3386	5.5257	5.4273	5.3408
6.4064	6.2962	6.2097	6.4098	6.2982	6.2116
7.2900	7.1665	7.0799	7.2932	7.1685	7.0818
8.1746	8.0379	7.9511	8.1777	8.0397	7.9529
9.0621	8.9121	8.8253	9.0653	8.9139	8.8271
9.9546	9.7910	9.7041	9.9578	9.7928	9.7060
10.8531	10.6755	10.5887	10.8565	10.6774	10.5908
11.7578	11.5658	11.4792	11.7616	11.5680	11.4815
12.6675	12.4608	12.3744	12.6718	12.4633	12.3772
13.5795	13.3578	13.2717	13.5846	13.3609	13.2751
14.4896	14.2529	14.1672	14.4955	14.2566	14.1712
15.3925	15.1409	15.0555	15.3991	15.1452	15.0602
16.2822	16.0154	15.9305	16.2893	16.0202	15.9357
17.1533	16.8702	16.7857	17.1605	16.8752	16.7911

Table A-3. Variation of RMS in Length Estimation in the Revisited TM Data (Power Stroke)

Mean and RMS Cilium Lengths (Power Stroke: TS 38-14) (μm)					
Mean (top)	Mean (mid)	Mean (bot)	RMS (top)	RMS (mid)	RMS (bot)
0.1253	0.1062	0	0.1420	0.1106	0
1.0862	1.0541	0.9496	1.0915	1.0572	0.9529
2.0113	1.9682	1.8649	2.0168	1.9723	1.8691
2.9130	2.8590	2.7564	2.9180	2.8630	2.7605
3.8002	3.7344	3.6320	3.8045	3.7380	3.6357
4.6788	4.6000	4.4975	4.6826	4.6031	4.5008
5.5525	5.4595	5.3568	5.5559	5.4622	5.3597
6.4235	6.3154	6.2124	6.4267	6.3178	6.2150
7.2929	7.1692	7.0660	7.2961	7.1715	7.0684
8.1615	8.0222	7.9187	8.1647	8.0243	7.9210
9.0299	8.8749	8.7714	9.0330	8.8769	8.7736
9.8983	9.7279	9.6246	9.9015	9.7298	9.6267
10.7672	10.5816	10.4787	10.7703	10.5834	10.4807
11.6366	11.4361	11.3337	11.6397	11.4377	11.3356
12.5064	12.2909	12.1893	12.5094	12.2925	12.1911
13.3759	13.1454	13.0447	13.3789	13.1469	13.0464
14.2442	13.9984	13.8987	14.2472	13.9998	13.9003
15.1099	14.8480	14.7494	15.1127	14.8493	14.7509
15.9711	15.6918	15.5943	15.9739	15.6931	15.5957
16.8264	16.5271	16.4306	16.8292	16.5283	16.4320

Table A-4. Variation of RMS in Length Estimation in the Revisited TM Data (Return Stroke)

Mean and RMS Cilium Lengths (Return Stroke: TS 15-37) (μm)					
Mean (top)	Mean (mid)	Mean (bot)	RMS (top)	RMS (mid)	RMS (bot)
0.1025	0.0721	0	0.1133	0.0777	0
1.0021	0.9600	0.8877	1.0078	0.9640	0.8905
1.9008	1.8475	1.7750	1.9068	1.8515	1.7782
2.8005	2.7357	2.6631	2.8059	2.7391	2.6658
3.7006	3.6239	3.5513	3.7052	3.6266	3.5534
4.5997	4.5110	4.4383	4.6037	4.5132	4.4400
5.4969	5.3964	5.3236	5.5005	5.3982	5.3251
6.3924	6.2803	6.2075	6.3958	6.2820	6.2089
7.2876	7.1643	7.0914	7.2909	7.1659	7.0928
8.1853	8.0509	7.9779	8.1885	8.0525	7.9792
9.0888	8.9429	8.8698	9.0919	8.9444	8.8711
10.0010	9.8430	9.7698	10.0041	9.8445	9.7711
10.9240	10.7530	10.6796	10.9272	10.7544	10.6809
11.8579	11.6730	11.5994	11.8613	11.6744	11.6008
12.8006	12.6011	12.5273	12.8045	12.6027	12.5288
13.7477	13.5333	13.4592	13.7521	13.5351	13.4610
14.6923	14.4632	14.3890	14.6974	14.4653	14.3911
15.6260	15.3828	15.3084	15.6317	15.3853	15.3110
16.5392	16.2828	16.2083	16.5453	16.2856	16.2112
17.4234	17.1536	17.0791	17.4294	17.1565	17.0821

A.2.4 Definitions

In figure 5, the angles off the x-axis are defined as:

$$\text{position_angle} = \text{acos}(x_length/\text{total_length}) * 180/\pi,$$

and

$$\text{velocity_angle} = \text{acos}(x_velocity/\text{total_velocity}) * 180/\pi.$$

A.2.5 Waveforms Used for Robotic Control

In the early phase of the work, the data in figure A-4 were compared with a sine wave, applying a phase difference to determine if the biological cilium motion could be reproduced by sine waveform in the robotic cilium. Comparison of the angles with sine waves was made by adding a phase shift of 90° or 120°, and the result is shown in figure A-5. A sine wave is a good approximation of the biological cilium position and the 120° phase difference has a better fit to the biological cilium than the 90° phase difference does. Both the Cartesian and the polar coordinates can be used for robotic control.

The fit of the sine wave suggests that the moment applied at the base and the motion of the biological cilium are related, although the cilium is alternately taut and slack during the power and return strokes, respectively.

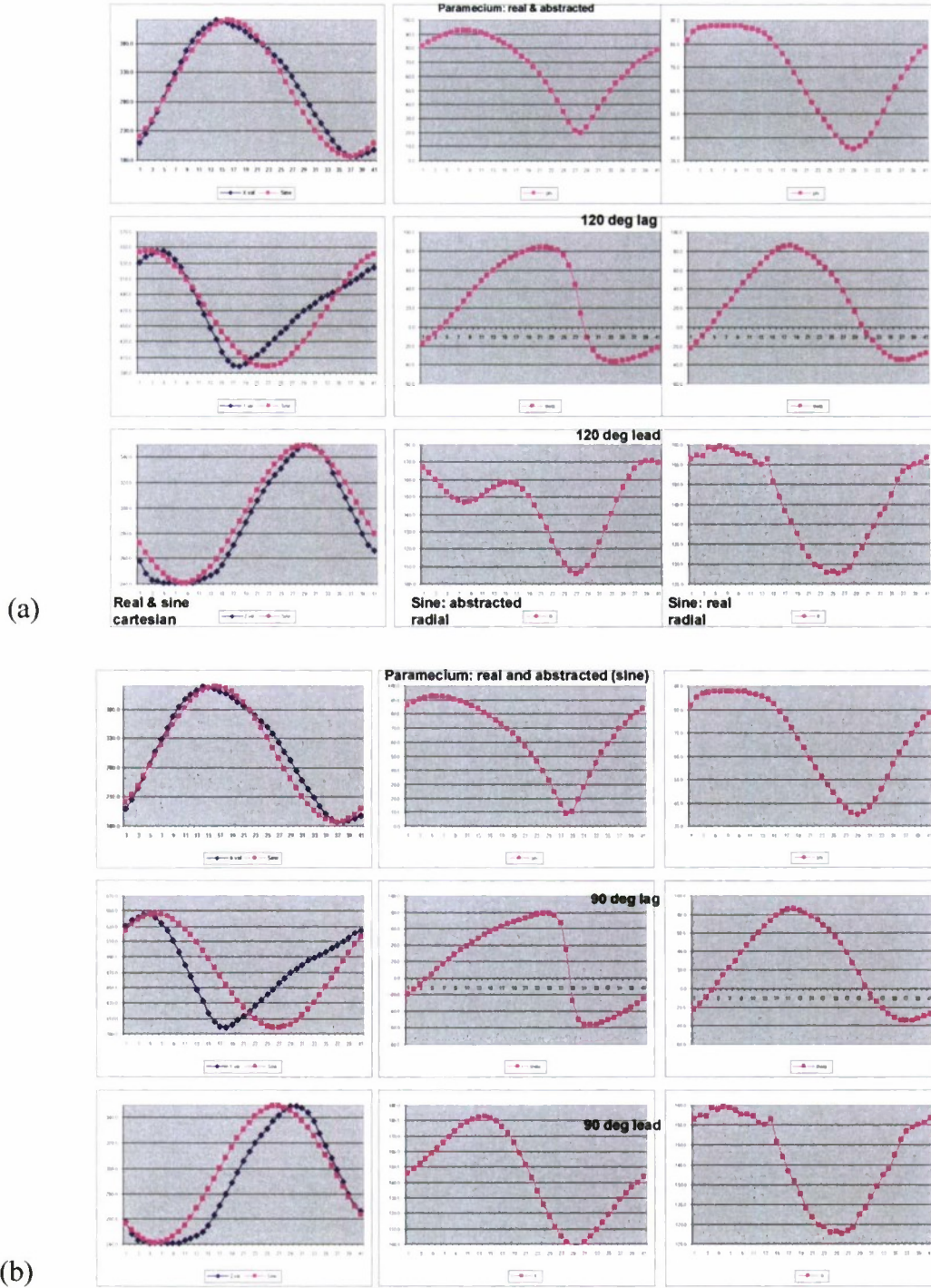


Figure A-5. Biological Cilium Waveform from the Revisited TM Data (Termed “real” in Figure Legend) at the Distal Point Compared with Sine Waveforms in Cartesian and Polar Coordinates (The sine waveforms (termed “abstracted”) are also compared with sine waves at phase lead/lag differences of 120° (upper set of plots) and 90° (lower set of plots). Left Column: Cartesian; middle column: polar (real: biological cilium; dark symbols); right column: polar (abstracted: sine wave; light symbols).)

A.3 ROBOTIC CILIUM

A.3.1 Early Work on CAD Simulation with D-Cam Guide and Fabrication of a D-Cam Pendulum

A.3.1.1 CAD Simulation. Computer-aided design (CAD) is an accurately dimensioned, three-dimensional geometric relationship between objects that is also precisely defined at all instants of time when relative motion between the components exists. Hydrodynamic simulations of living animals frequently lack fluid-structure interactions because the structural properties are unknown. Therefore, at an early stage, it was thought to be prudent to carry out a CAD simulation to understand the IOOMs that are involved in the cilium motion (see figure 11a in the main text).

It is hypothesized that a D-cam would force the cilium to generate the observed motion verifiable in orthogonal planes. Figure A-6 shows successive frames from the CAD simulation. The cilium was given planar bending only; hence, it will not produce torsion and the question arises: What is the origin of torsion? (see section A.4 of this appendix). In view of the similarities of the robotic motion to the biological cilium, it is concluded that the points at any fixed distance from the base circumscribe the shape given by the letter D in planform—see figure 13a (left column). The power stroke roughly extends over the straight part of the D, and the return stroke traces the curved part. This exercise helped build the cilium actuation apparatus shown in figures A-7 and A-8.

A.3.1.2 Fabrication of a D-Cam Pendulum. Section A.3.1.1 suggests that the cilium could be modeled as a compound pendulum. Figure A-7 shows a schematic and a photograph of the drive and guide of such a pendulum (the cilium is not shown). The positive and negative cams d^+ and d^- act as the guide of cilium track. The pendulum base is located at X. The cilium would be attached to the end of C.

In figure A-7, T, M, and B are three stacked discs; disc B has a cutout of shape D labeled “ d^- ”; there is a D-shaped cam (d^+) between discs M and T; a bar (L-C) runs from d^+ to d^- at the bottom of which the cilium hangs; there is a universal support bearing X where this bar meets disc M; there is a paper clip L that is used by a lever above the disc T (hidden under the hand in the photograph) to turn the C-bar along the path shown by the broken line at the top of the schematic whereby the C-bar runs while hugging the two D-cams along the arrows shown or in the reverse direction.

Note the similarity between figures A-6 and A-7—the CAD and the hardware renditions.

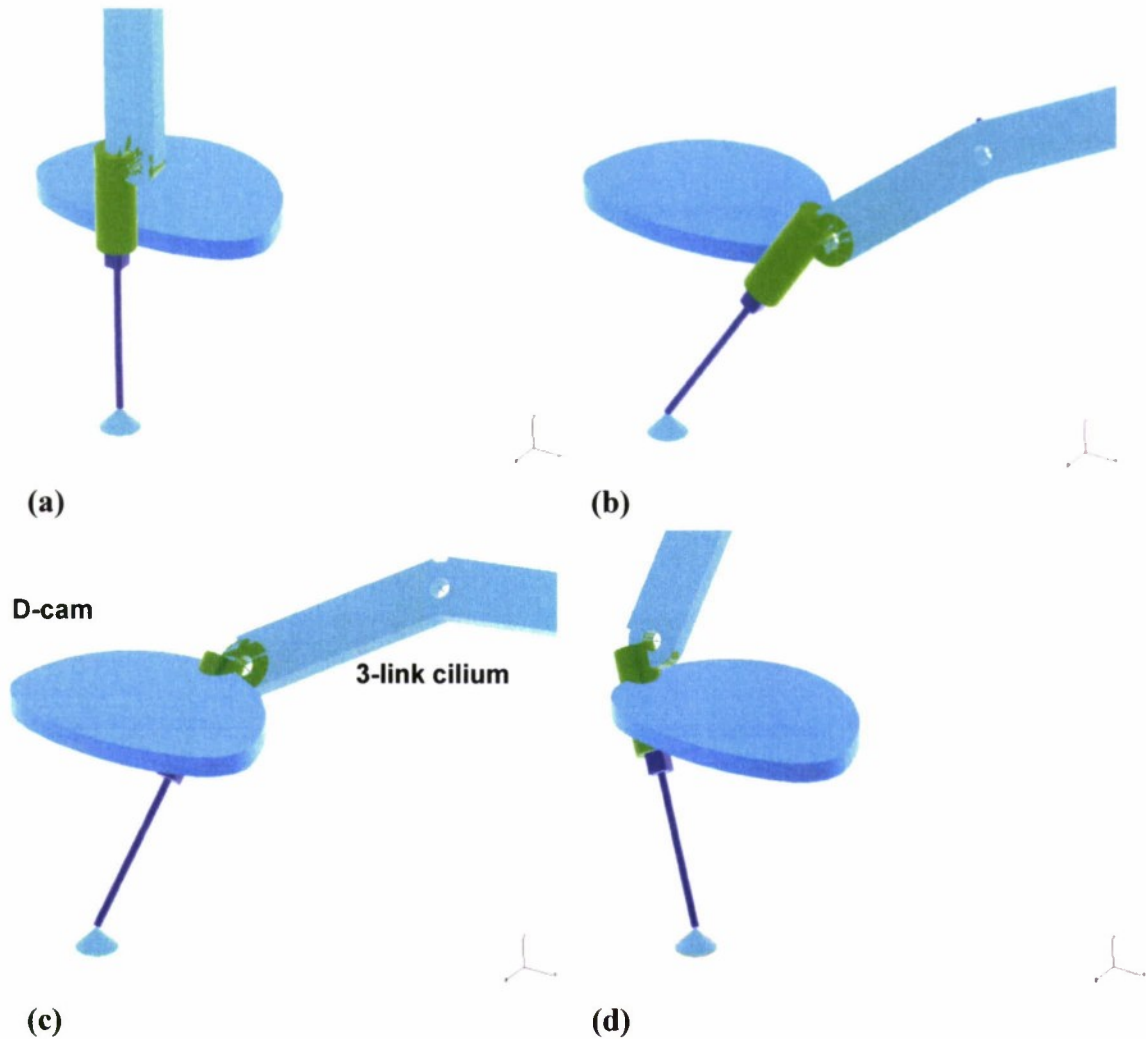


Figure A-6. Successive Frames (Time Increases from a to d) from CAD Simulation of D-Cam-Guided Three-Link Robotic Cilium (The robotic cilium is straight in the flat portion of the D-cam, and it droops while in the round part of the cilium.)

Note: See the operation of the D-cam in the CAD video file titled “flagellum_dual.mov” in shared folder D:\Documents and Settings\promode.bandyopadhyay\My Documents\Cilium (also available from the lead author).

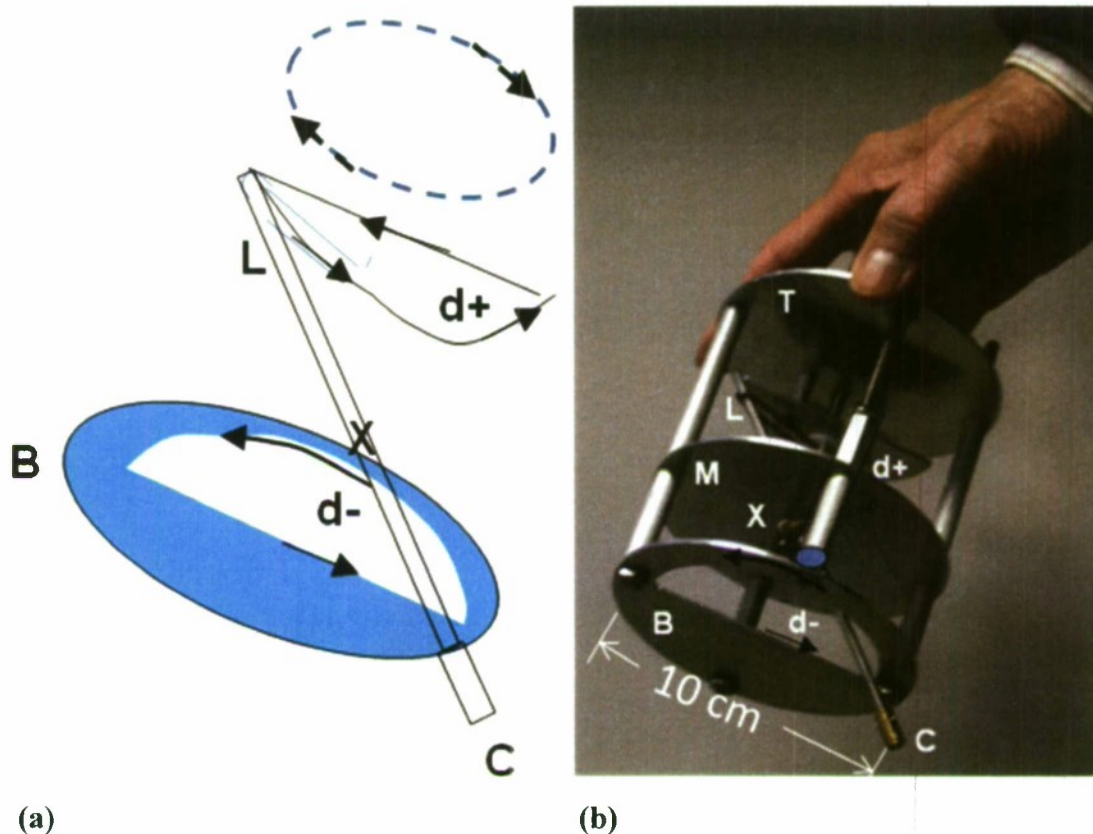


Figure A-7. Pendulum Apparatus for Understanding Cilium Motion:
(a) Schematic, (b) Photograph of the Apparatus

A.3.2 Early Version of Robotic Cilium Apparatus

Figure A-8 provides a schematic and photograph of the early version of the robotic cilium, and figure A-9 shows how planar bending is produced in the robotic cilium using a pair of antagonistic sliders.

In figure A-8, the symbols are as follows: U: universal joint, R: cilium bending mechanism (see figure A-9), 1-1 and 2-2 make one pair of bucket handles, and 3-3 and 4-4 make another pair (the bucket handles allow the base of the cilium (U) to remain at the same location while the IOOM motors impart motion to the cilium); and M_x , M_z , and M_b are x, z, and bending motors. Note that in this apparatus, the twist motor (M_y) is absent, the need for which became clear later. This apparatus worked, but it was desirable to replace the bucket handle design to reduce friction.

Note: See the video “FlagModel” (9,855-kb Windows Media; available from the lead author) to observe the operation of the dual-strip cilium model in figure A-9, and of the dual bucket handle mechanism shown in figure A-8.

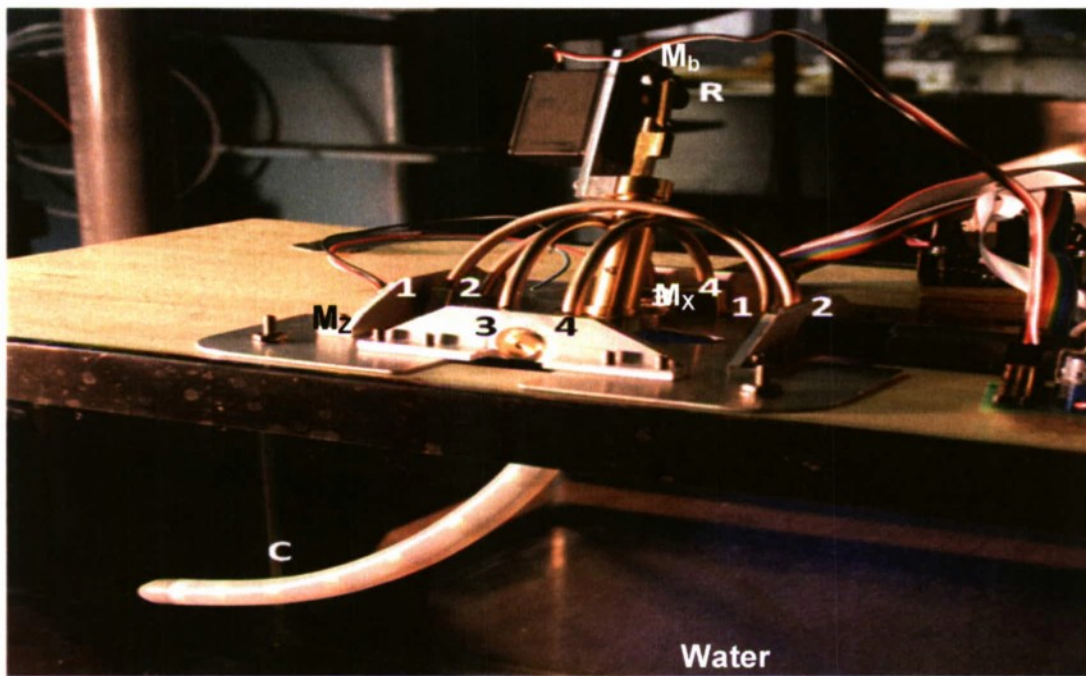
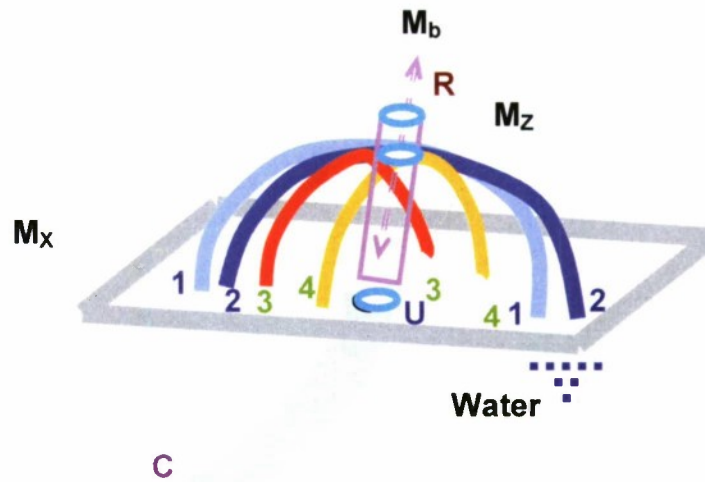


Figure A-8. Schematic and Photograph of Early Version of the Biorobotic Cilium Apparatus

**Robotic Paramecium:
How it bends in 2d**

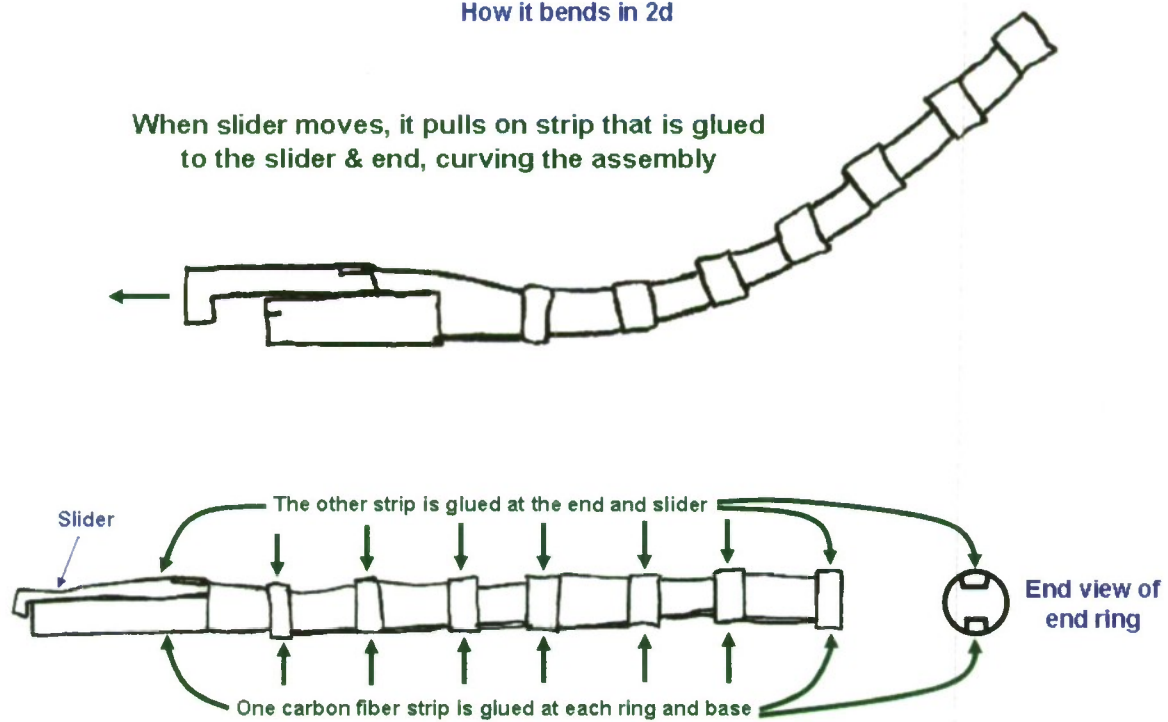


Figure A-9. Schematic of Mechanism Showing How Planar Bending Is Produced in the Robotic Cilium by Sliding the Top Strip Relative to the Bottom Strip (Both sketches are side views.)

A.3.3 Experimental Simulation of Cilium Reynolds Number

Using catheter tubing of 1 mm diameter for a flow velocity U scale of 1 mm/s, and water at 5°C, the kinematic viscosity is $1.5 \times 10^{-6} \text{ m}^2/\text{s}$, giving a Reynolds number Re of 0.66, which is < 1.0 for the same drag-versus- Re relationship to apply. Therefore, using a magneto-rheological fluid, it may be possible to simulate the property of variable hardness in a realistic Re number and perhaps neutral buoyancy. An even lower Reynolds number is desirable and this is achievable for $U = 0.1 \text{ mm/s}$, which gives an $Re = 0.066$ (which is < 0.1).

A.4 “FRICTIONLESS” CILIUM ACTUATION USING A HEMISPHERICAL MOTOR DRIVE

In a pendulum design, it is important to lower friction. Figure A-10 shows photographs of a hemispherical motor, and figure A-11 is a schematic of the magnets and air gaps. This motor should be an extremely low friction pendulum, which is an alternative to the Maxon motor drives used in figures 11 and A-8.

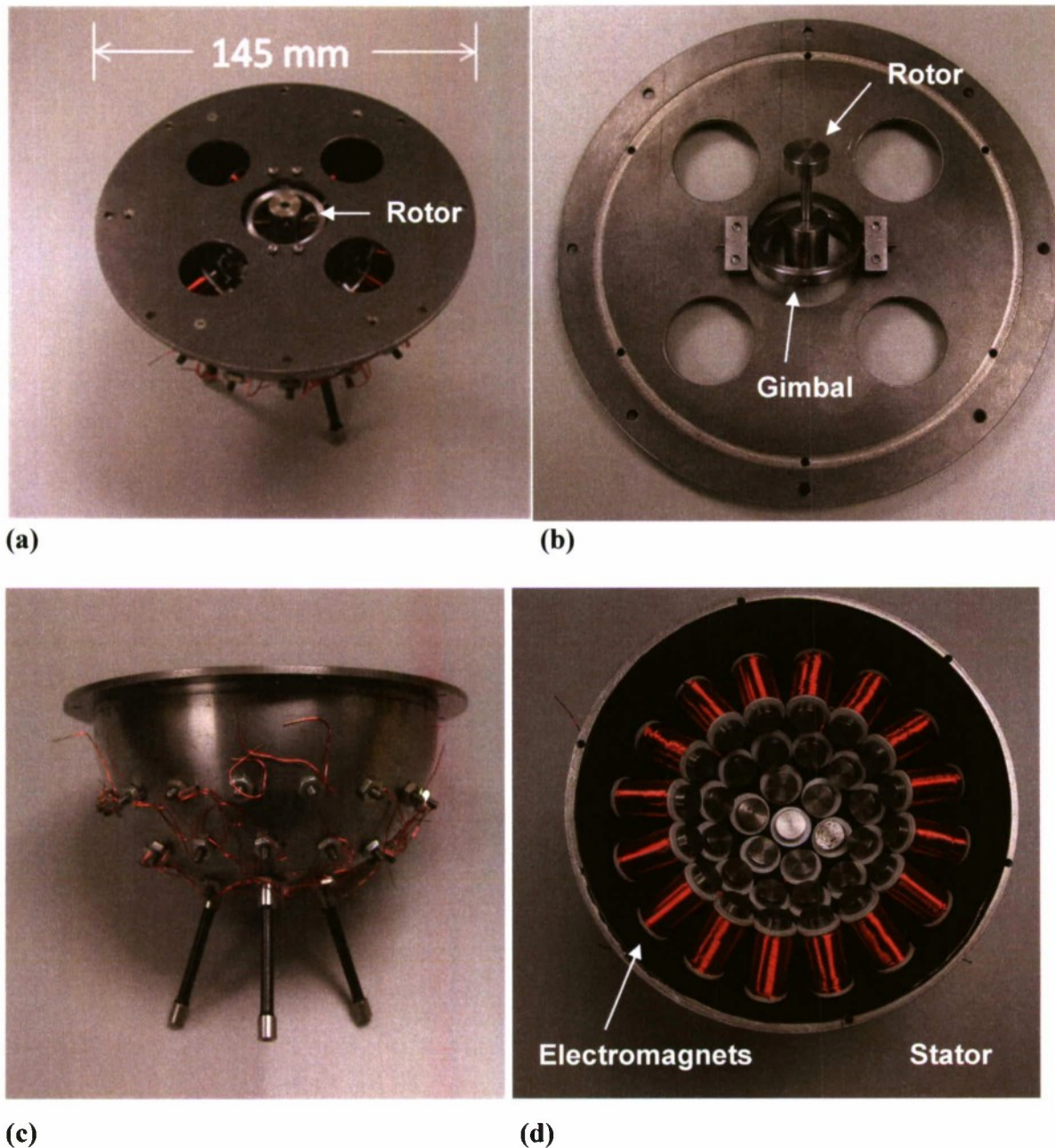


Figure A-10. Photographs of the Rotor (b) and Stator (d) of a Hemispherical Motor (a, c) Assembly

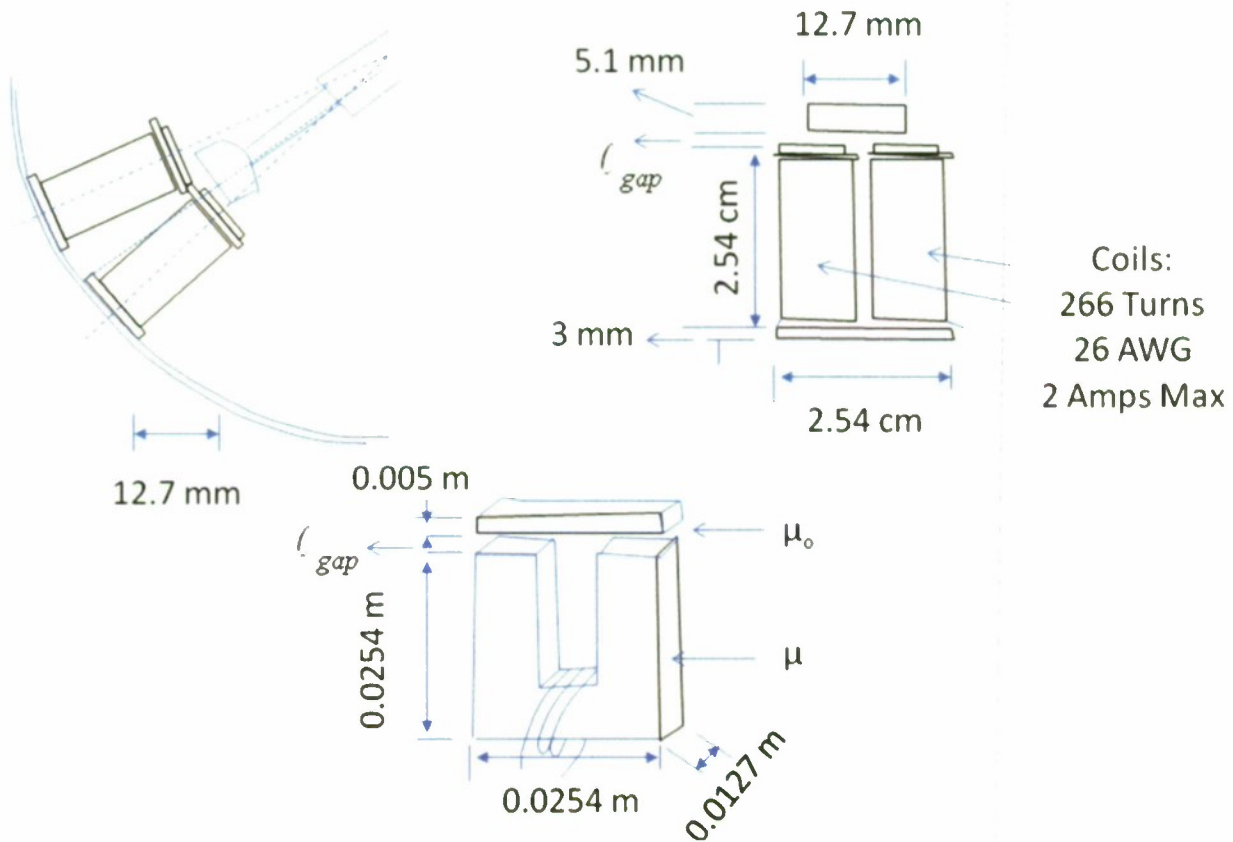


Figure A-11. Schematic of Electromagnets and Gaps in the Hemispherical Motor

The hemispherical motor has 35 electromagnets. The power supply to these motors is to be programmed to drive the rotor. The program should ensure that the required IOOMs are imparted on the cilium. Figure A-10a is view of the assembly; A-10b shows the underside of the top plate of the pendulum drive and the gimbal; A-10c shows a side view of the assembly; and A-10d shows the 35-electromagnet assembly exposed; the pendulum ball in figure A-10b skirts the hemispherical surface resulting from the assembly shown in A-10d with a small clearance.

Figure A-11 is a schematic of the electromagnets and of the air and steel gaps. This schematic was used to model the force produced by each electromagnet. The following formulation is due to J. Dana Hrubes (NUWC Code 8233), who had used this relationship and measurements with a moment arm to estimate the viability of the hemispherical motor shown in figures A-10 and A-11. The magneto-motive force F is given by

$$F = \frac{(ni)^2 \mu_0 A}{2\ell_{gap}^2}, \quad (A-1)$$

where n = the number of turns in the coil in each electromagnet, i = the current through the coil, μ_0 = the magnetic permeability in a vacuum, A = area, and ℓ_{gap} = the air gap between the magnet and steel in the direction of the magnetic flux. Compared to μ_0 , the magnetic permeability of cold rolled steel is 2000 times larger. For a gap ℓ_{gap} of 3 to 4 mm at $i = 1.5$ A, both equation (A-1) and measurement of maximum force lead to a force of 0.74 N. The tentative conclusion is that the design in figure A-10 would produce the required cilium motion.

A.5 ROLE OF TORSIONAL RIGIDITY IN THE MANIFESTATION OF TORSION

The objective is to understand the role of material properties (such as torsional elasticity and moment of inertia) in the manifestation of torsion (production of off-plane curvature) in a surface under fluid loading. Several three-doublet-long robotic cilia have been fabricated. As figure A-12 shows, the three doublets consist of three pairs of fixed-length, inextendable tension wires positioned diametrically across within the pair, and 120° apart between pairs; within a pair, the tension wire is continuous and is given two windings over the pulley. There is also a spring-loaded central tension wire. The tension wires pass through the cilium, which is made of segments of Plexiglas rods. There is a gap of about 1 mm between these rod segments; a small ball, which acts as a pivot, is positioned at the center between adjacent rod segments. A real cilium has 9+2 doublet (“axenome”) construction (Dute and Kung, 1978). Like the biological doublets, the robotic doublets also produce relative motion (sliding) between a pair of axial bars. Three-dimensionality develops in the abstracted robotic cilium in figure A-12 as follows:

When neutrally buoyant, the geometric deformation (k, τ) in the robotic cilium is given by

$$(k, \tau) = fn(G, E, I, C_d, T),$$

where G and E are the moduli of torsion and elasticity, respectively, I is the moment of inertia, C_d is the coefficient of drag, and T is the applied distortion torque.

In the particular example in figure A-13, when a torque is applied to one of the levers, a helical spiral is produced (curvature κ and torsion τ are both constant) and the deflection is not planar. This finding came as a surprise, because a planar distortion (as shown in figure A-12) was expected. The levers were found to be coupled (if one is rotated, the others also rotate). So, the question was: *What is the mechanism of the three-dimensional distortion produced?*

As figure A-14 shows, when sheathing is tightly slipped over the three-doublet cilium, planar deflection is produced; that is, a helical spiral is not produced. (The robotic cilium in figure A-14 is shorter than that shown in figure A-13.) The torsion does not manifest itself this time. This behavior can be understood by recognizing the role of the modulus of torsional rigidity. Note that (as figure A-12 shows) the robotic cilium has air gaps between the segments,

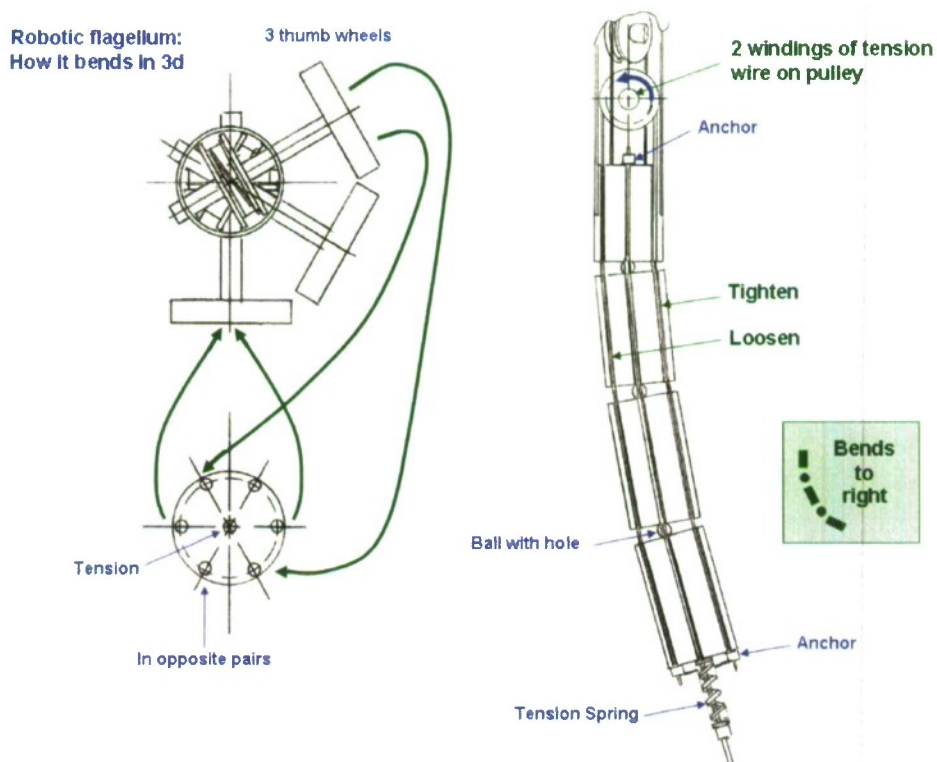


Figure A-12. Schematic of Mechanism for Actuating a Long Robotic Cilium

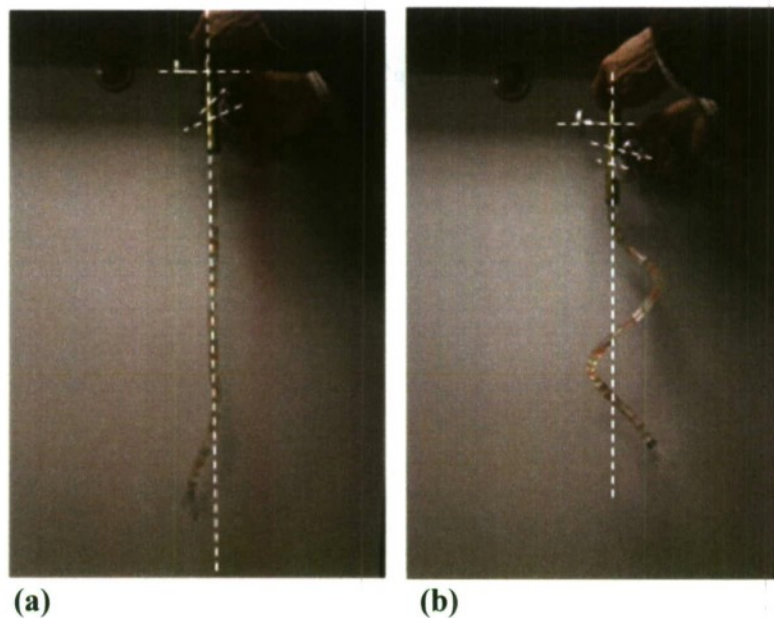


Figure A-13. Development of Torsion in a Low-Hardness "Rod"
(In (a) and (b), the lower thumbwheel is being turned in the clockwise direction. Broken lines: Lever and baseline robotic cilium axes. Deformation is propagated from the distal point to the base.)

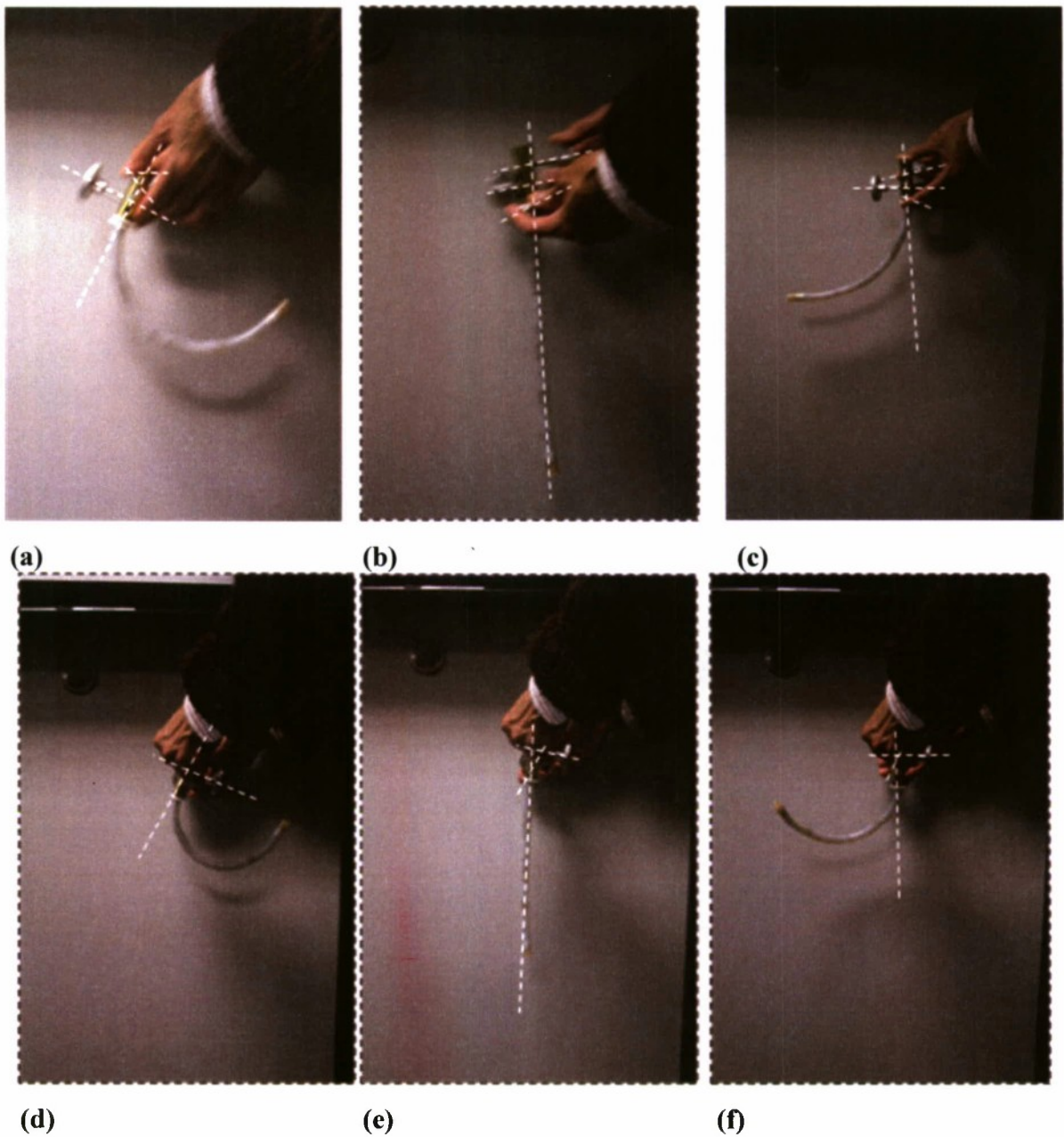


Figure A-14. Effects of Clockwise and Anti-Clockwise Turning of a Doublet of a Two-Doublet Sheathed Cilium Oriented Orthogonally: (a) and (c) - Doublet 1; (d) and (e) - Doublet 2 (Broken lines: Lever and baseline robotic cilium axes.)

which makes the torsional rigidity of the cilium extremely low (close to zero). On the other hand, when tight sheathing is slipped over it, the cilium becomes hard. Therefore, *high hardness resists the manifestation of torsion, but low hardness does not. Importantly, a critical hardness should exist at the boundary of the two hardnesses in the hardness versus torsion relationship, where a slight increase, or decrease in hardness, would produce substantial change in the manifestation of torsion.*

Let ψ be the angular distortion/axial length. Then,

$$GI = T\psi.$$

If ψ remains the same in samples 1 and 2,

$$T_2 / (GI)_2 = T_1 / (GI)_1.$$

For the given angular deflection, when GI is low, less torque would be required to shear to the same angle over the same axial distance. (When G is reduced from a high value, the levers in figure A-13 are easier to turn.) Therefore, GI should be as low as possible so that the work required to deform is reduced.

The sensitivity of resulting torsion and applied torque to hardness was further verified in the following manner. Two robotic rubber cilia (figure A-15) of two different hardnesses were fabricated (the segment gaps shown in figure A-12 were absent); the properties of these robotic cilia are listed in table A-5. The doublet driving mechanism shown in figure A-12 was used. In figure A-15a, the lower level is being turned, and in figure A-15b, the upper lever is being turned. In both cases, the cilium is bending in the plane normal to the level axis, and there is no torsion.

Table A-6 summarizes the in-plane and off-plane curvature tendencies and torque required. In summary, the sheathing and hardness of A53-63 and A20-30 prevent manifestation of the torsion; the radius of the curling is lower in A20-30 because the curvature k is higher (radius of curvature $\sigma_k = 1/k$), less torque is needed to turn the lever the same angle; and torsion is manifested only in the case when torsional rigidity is nearly zero. The hardness needs to be below A20-30 for the torsion to be manifested.

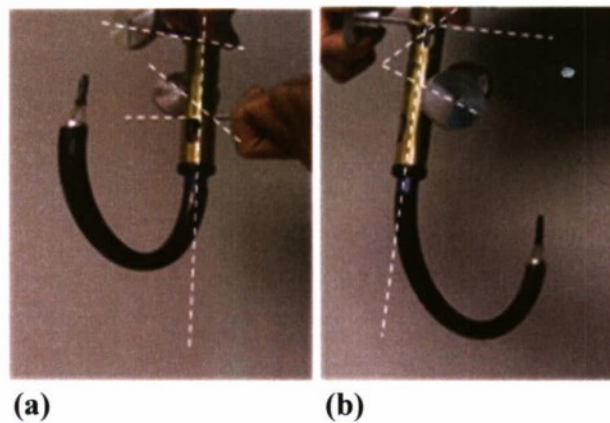


Figure A-15. Cilia Constructed of Continuous Rubber
(see Table A-5) (Hardness A53-A63)
(Broken lines: Lever and baseline robotic cilium axes.)

Table A-5. Physical Properties of Two Low-Viscosity Two-Component Urethane Casting Elastomers Used for the Robotic Cilia Shown in Figure A-14
(Source: H. B. Fuller Company, PO Box 64683, St. Paul, MN 55164)

Property	Ultralite FH-3140	Ultralite FH-3138
These elastomers are designed to make flexible molds for use with thermosetting resins; they pour and cure at room temperature.	Used to make tough, yet flexible molds; not moisture sensitive	Soft and flexible, yet tough compound can reproduce finest detail and will flex to release from undercuts without tearing
Shore A Hardness	53 – 63	20 – 30
Specific Gravity	1.03	0.992

**Table A-6. Types of Distortion Observed in a Long Robotic Cilium
When a Torque Is Applied at the Base**

Sample No.	Hardness	Length	Observation of Distortion When Moment Is Applied at the Base	Torque Required to Shear 1° per 1 cm of Axial Length; Scale: 0 (low), 10 (high) (not yet measured)
1	Little resistance to torque/deg due to the presence of gaps between segments	Full	Perfect helical spiral of uniform diameter and pitch (figure A-13)	1 – 3
2	Little resistance to torque/deg due to the presence of gaps between segments	Half	Spiral	2
2	Sheathed sample 2 resulting in high hardness	Half	Planar bending only; no spiraling (figure A-14)	9 – 10
3	A20-30	Half	Planar bending only; no spiraling	4 – 5
4	A53-63	Half	Planar bending only; no spiraling (figure A-14)	9 – 10

A.6 PROGRESS TOWARD ROBOTIC EMULATION OF NATURAL SWIMMING

Dynamic systems modeling (see figure 2 in the main text) has shown that the biological cilium track is a limit cycle. In this section, the effects of parameters on the quality of agreement of the model to the measurements of the biological cilium are considered, along with the progress made in the robotic emulation of natural swimming.

A.6.1 Effects of Equation Parameters on the Dynamic Systems Modeling Results

The exact form of the limit cycle in equation (1) depends on the values of the main parameter a (see Bandyopadhyay et al., 2008). The effects of a on the comparison between the Lienard equation model (equation (1)) and measurements is shown in figure A-16. The units shown are arbitrary; the modeling results are in arbitrary units of volts; and the units (μm) of the biological cilium tracks have been removed to scale them to the model (the \dot{v} results are not shown).

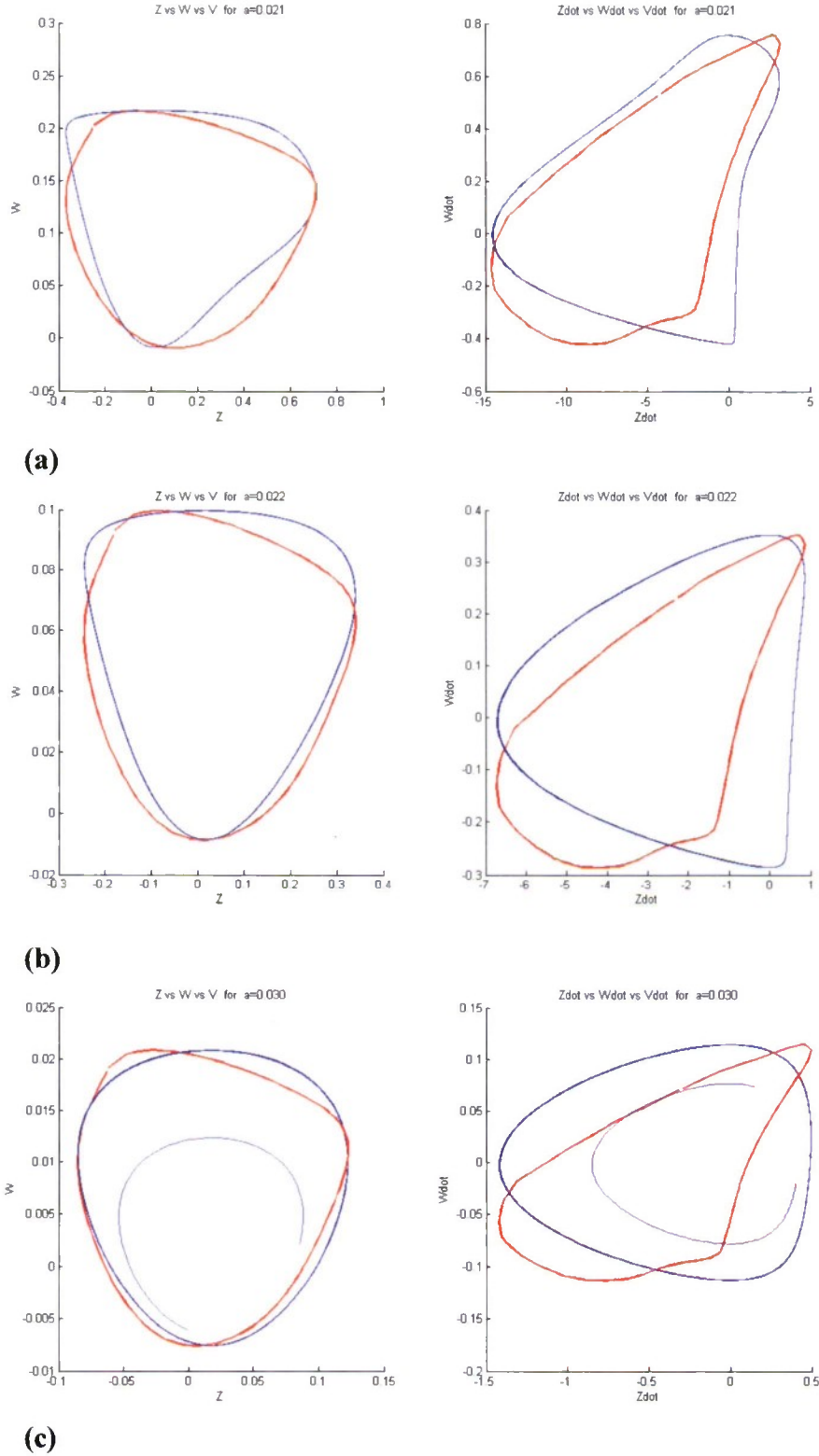


Figure A-16. Effects of the Parameter a on Olivo-Cerebellar Modeling of Cilium Motion (Model: blue; cilium distal point: red. Left column: position. Right column: velocity. Values of a are: (a) 0.021, (b) 0.022, and (c) 0.030.)

A.6.2 Electronic Analog Dynamic Systems Actuation of Robotic Cilium

To provide theoretical support to the patent applications on the nonlinear transduction described in Bandyopadhyay (2011 and 2012b), this section describes how the robotic cilium can be actuated using the dynamic systems model in equation (1). Figure A-17 shows the apparatus for future use in documenting the perturbation sensitivity of a cilium (disturbance rejection) to which torque is applied and which takes a limit cycle track (see figure 2). (Also see Bandyopadhyay et al., 2008.)

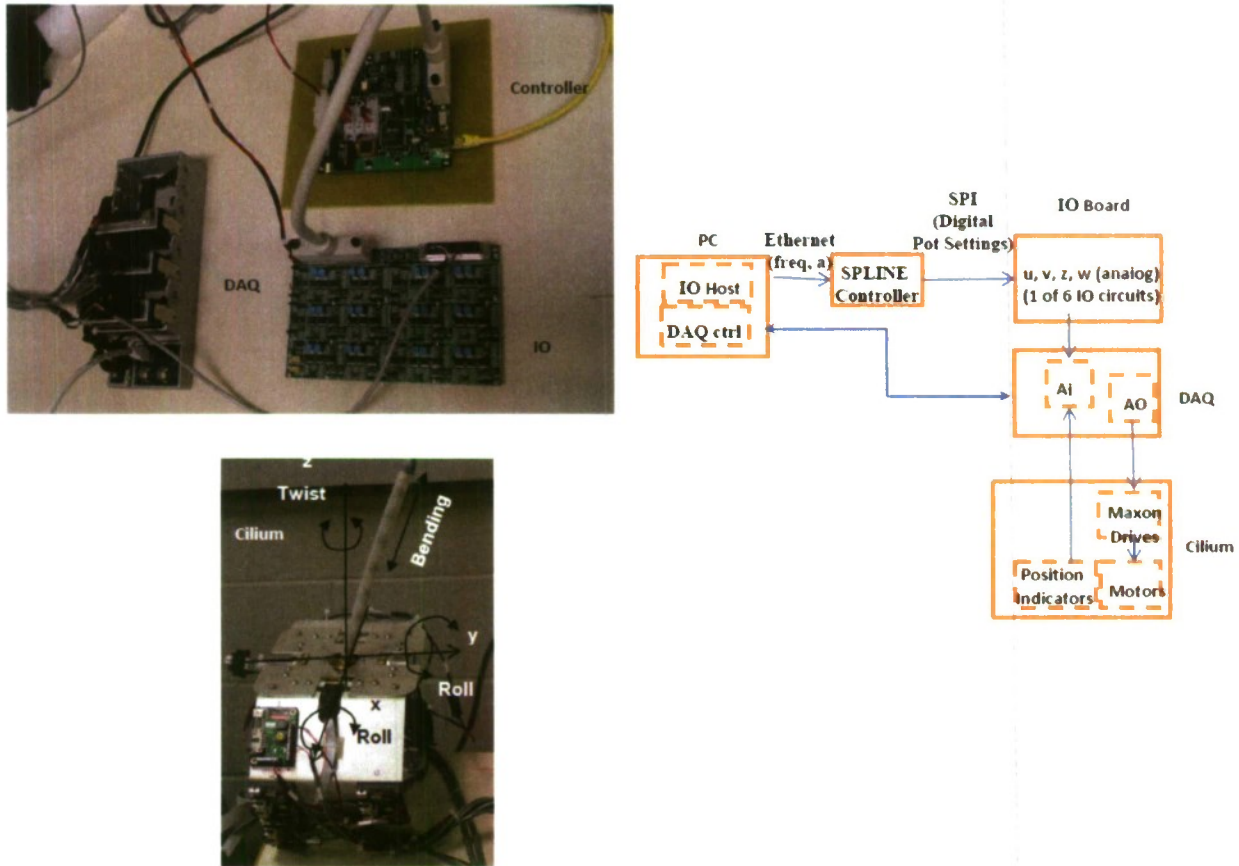


Figure A-17. Apparatus for Driving the Robotic Cilium Using the Electronic Rendition of Dynamic Systems Equation (1)

The schematic on the right in figure A-17 describes the relationship of the components in the upper left and lower left photographs. The lower left photograph is from figure 11 in the main text and shows the robotic cilium and the four-motor IOOM drive. The upper left photograph shows the analog circuit (labeled IO for inferior-olive motion control neuron (Llinas et al., 2004)) for generating the solution to equation (1), the digital controller, and the digital data acquisition circuit (DAQ: digital to analog and analog to digital) for relating the analog component to the digital IOOMs. The wiring is shown in the schematic on the right. (A video showing the operation of the robotic cilium using the analog (IO) device is available from the lead author.)

A.7 SYNTHETIC MODELING OF THE TRANSFORMATION FROM SMALL TO LARGE VIA OPTIMIZATION MECHANISMS OF METACHRONISM AND SELF-REGULATION

A meta analysis by Bandyopadhyay (2011) shows that the propulsion density (kW/m^3) of small and large swimming animals (considering their red muscles only for cruising) remains invariant of whether they are large or small. (In fact, this relationship extends to engineering underwater swimming vehicles, irrespective of the propulsion mechanism.)

Is there any relationship between the microscopic cilium propulsors of the paramecium (Reynolds number $Re \sim 0.1$) and the larger propulsors of fish ($Re \sim 1$ to 10 to 100 's) (which have flexible pectoral flapping fins) and even larger animals such as penguins, dolphins, and whales (which have larger, stiffer fins) ($Re \geq 1000$)?

Information on how the oceans changed over time is contained to some extent in the boundary conditions and optimization rules followed by swimming animals. To aid the hydrodynamic study of such synthetic evolution, the relationship of cilium actuator to eel and fish fins was notionally explored and is given in Bandyopadhyay (2009).

Consider the following two steps showing how one could conceivably go from small (S) to medium (M) and from small to large (L), as shown schematically in figures A-18 through A-21:

1. Metachronism as the Mechanism of Optimization for Transformation from S to M. Apply metachronism as the dominant mechanism to optimize from S to M, the Reynolds number range being smaller than that in S to L. Assume that S to M is a “bifurcation” whereby higher orders of freedom are introduced while retaining the intrinsic dynamic system (equation (1)). The metachronic coupling of the downstream cilia may now be added to generate the sinuous motion of the dorsal fin. Metachronism is a two-dimensional mechanism and is applied to the motion of a two-dimensional array of cilia, shown in figure A-19. The cilium motion is three-dimensional, and the array is wrapped longitudinally with a membrane, whereby spanwise eel motion can be produced. Time increases from (a) to (d); the bunching of the cilia denotes a switch-over from the power stroke to the return stroke. The inset in figure A-19 is a top view showing the D-tracks of the cilia and how they alternate in the transverse plane with the fin wave. Qualitatively, the synthetic trans-species evolution result is a morphological motion of the eel dorsal fin from the cilium motion. This hypothesis requires verification.

2. Self-Regulation as the Mechanism of Optimization for Transformation from S to L. Assume that self-regulation continues as Re is increased from S to L and that equation (1) applies. The re-mix of the following variables is considered in this rule: material (G , E) and conformational properties (I), Re range, lowering of the natural frequency with the increase in Re and forcing at this frequency, and the parameter a in equation (1).

Consider the progression from S to L directly. The cilium has nine pairs of push-pull microtubules spread over a circular rim and two microtubules at the center for actuation (figure A-20a). To generate L, imagine that the cilia are unwrapped, as shown in figures A-20b and



Figure A-18. Thrust Actuators from S to M to L Considered in Bandyopadhyay (2009)

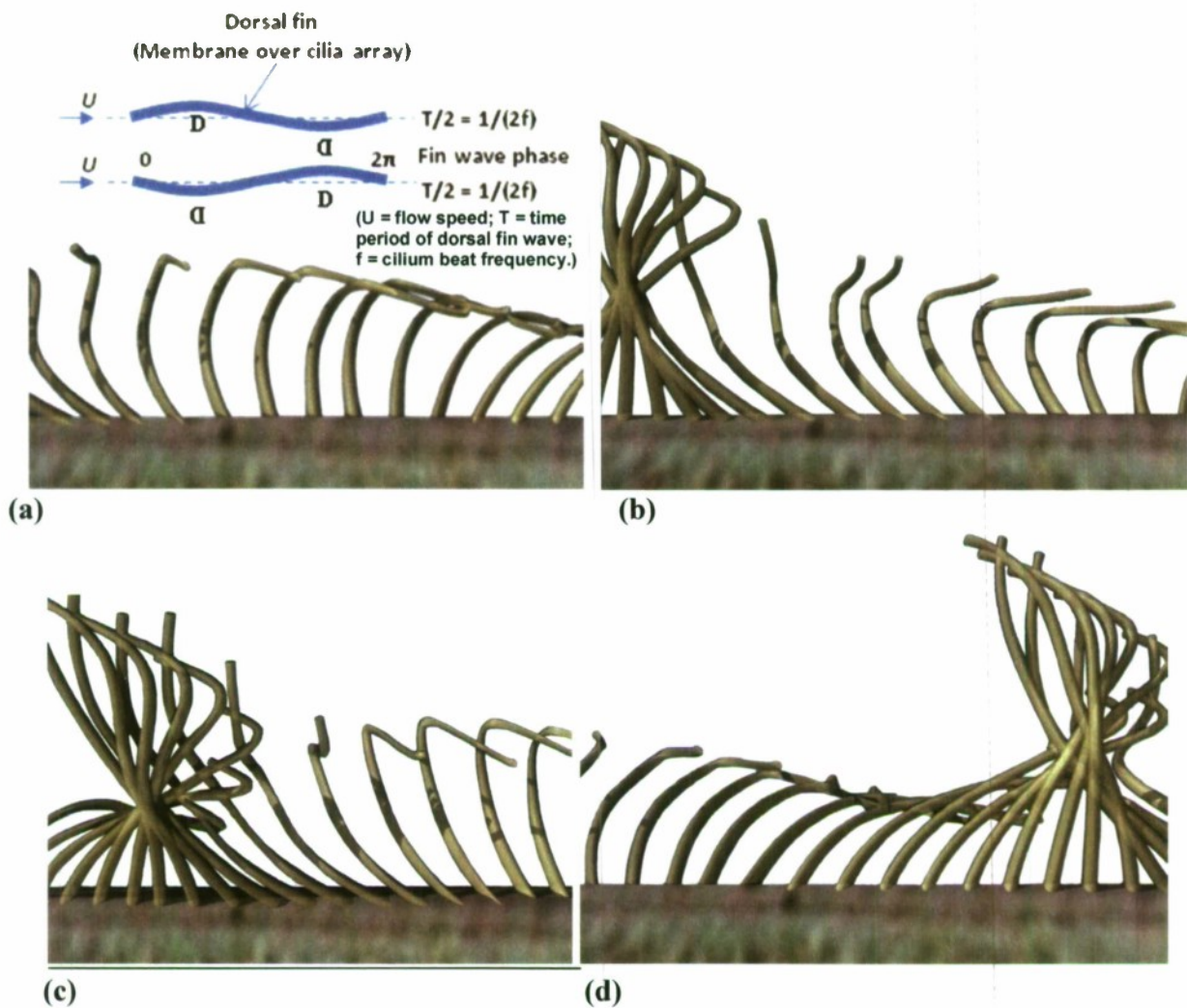


Figure A-19. Schematic of How a Metachronal Wave Produced with a Densely Packed and Membrane-Wrapped Two-Dimensional Array of Cilia Can Emulate an Eel (Time increases from a to d.)

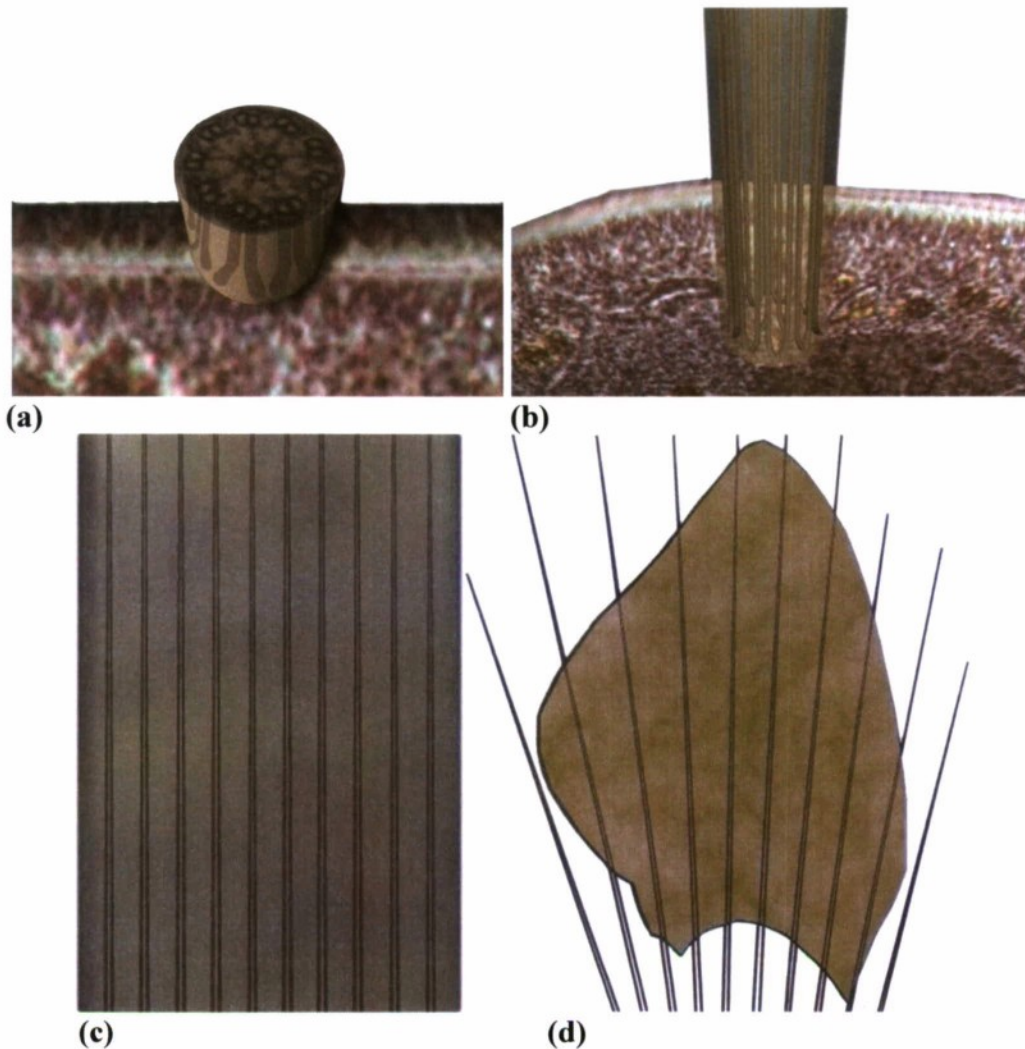


Figure A-20. Schematic of Progressive Unwrapping of the Cilium to Produce a Fish's Pectoral Fin

A-20c. Assume that as in the cilium (Dute and Kung, 1978), the fin in L also has a virtual origin, and the push-pull microtubules are spread out from their virtual origin as a fan and are shortened in the sequence shown in figure A-20d. The end result is a fish's pectoral fin (see Lauder and Drucker, 2004). Each push-pull pair continues to be welded at the tip (hemitrich), whereby a sliding motion at the base would bend the fin bone as shown. To generate larger forces at higher Re , the fins are sheathed as in the eel optimization above. Oscillatory parameters are determined by minimization of drag.

The fin sequence in figure A-21a is from Drucker and Lauder (2004), with a virtual origin added. Figure A-21d shows the fin undergoing a beat cycle similar to the motion of a fish's pectoral fin, as in the video of Lauder (2009).

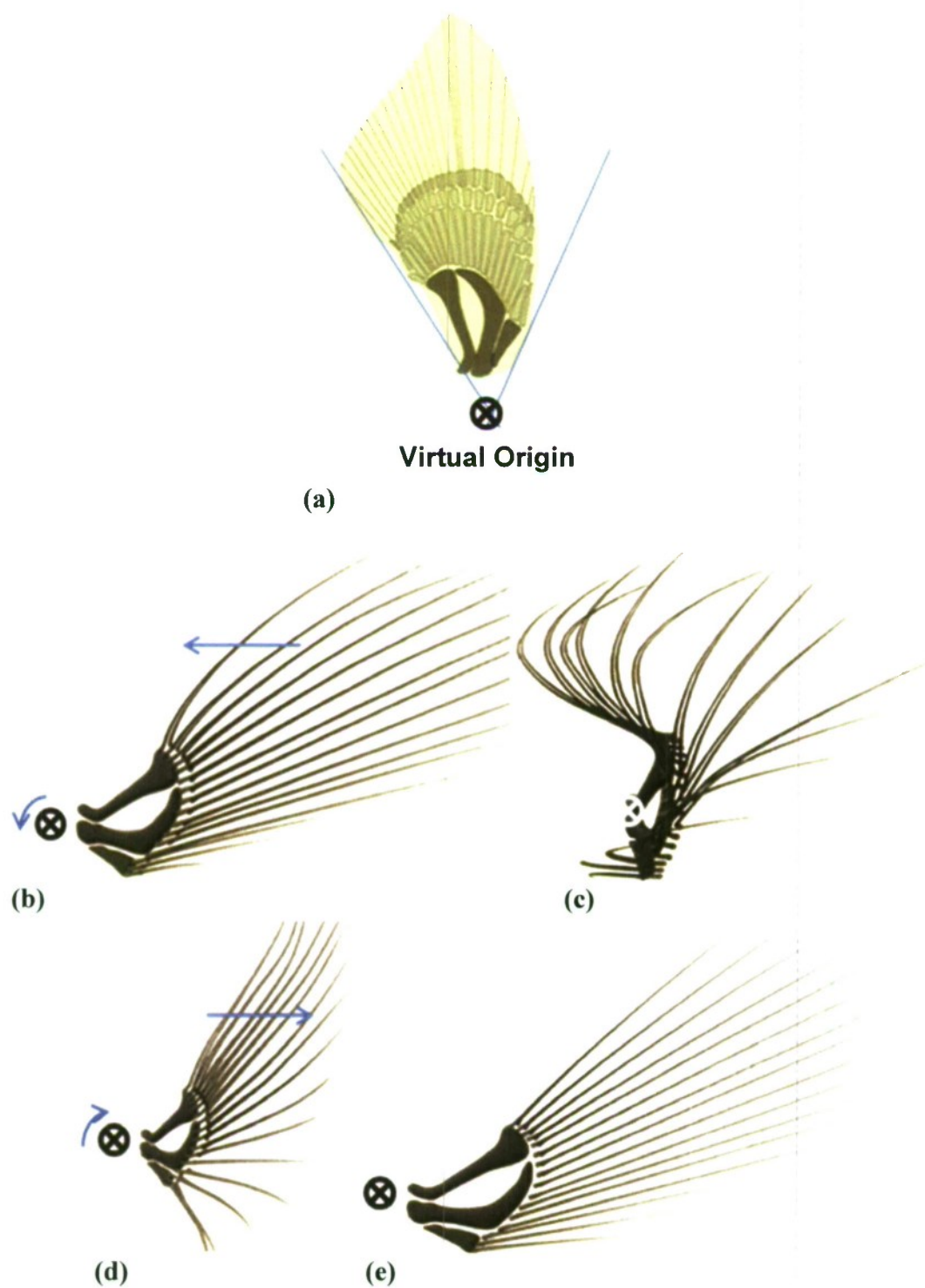


Figure A-21. Sequence Rationalizing the S to L Progression
(Arrows indicate the direction of fin motion. Oscillation of the fin assembly about the virtual origin qualitatively reproduces the motion of the sunfish pectoral fin as in Lauder (2009).)

INITIAL DISTRIBUTION LIST

Addressee	No. of Copies
Office of Naval Research (ONR-32—T. Paluszkievicz; ONR-321—T. Swean, M. Traweck; ONR-331—R. Joslin; ONR-332—T. McMullen; ONR-333—R. Brizzolara; ONR-34—T. Allard; ONR-341—J. Tangney, M. McKenna, I. Vodyanoy)	10
Naval Sea Systems Command (SEA-00—J. C. S. Meng)	1
Defense Technical Information Center	2
Massachusetts Institute of Technology (Attn: Prof. M. Triantafyllou, Prof. F. Hover, Prof. A. Techet, Prof. A. Annaswamy)	4
University of Houston (Attn: Prof. F. Hussain)	1
University of Nevada (Attn: Prof. K. Kim, Prof. S. Singh)	2
University of Cambridge (Attn: Prof. C. Ellington, Prof. A. Dowling)	2
University of Melbourne (Attn: Prof. M. Chong)	1
University of Iowa (Attn: Prof. V. Patel)	1
University of Michigan (Attn: Prof. Y. Young)	1
New York University Medical School (Attn: Prof. R. Llinas)	1
Arizona State University (Attn: Prof. R. Adrian)	1